The Pennsylvania State University

The Graduate School

ELASTIC NETWORK VIBRATION ISOLATORS

A Dissertation in

Mechanical Engineering

by

George Rai

Submitted in Partial Fulfillment

of the Requirements

for the Degree of

Doctor of Philosophy

December 2022

The dissertation of George Rai was reviewed and approved by the following:

Christopher Rahn
Professor of Mechanical Engineering and Associate Dean for Innovation, College of Engineering
Dissertation Co-Advisor
Co-Chair of Committee

Edward Smith
Professor of Aerospace Engineering
Dissertation Co-Advisor
Co-Chair of Committee

Joseph Najem
Assistant Professor of Mechanical Engineering

Stephen Hambric
Professor in the Penn State Graduate Program in Acoustics

Daniel Haworth
Associate Department Head of Graduate Programs
Professor of Mechanical Engineering

Abstract

Passive vibration isolators are widely used in engineering applications where the operating conditions are known, such as helicopter gearbox isolation, engine mounts, or sensitive laboratory equipment isolation. Their passive nature makes them favorable over more complex active-control type vibration isolation techniques. The main challenge, however, is that passive isolators often trade a simplistic design and excellent isolation behavior for a larger footprint and a large mass-penalty. Fluid-based passive isolators trade improved isolation performance and footprint over strictly mechanical designs for a more complex manufacturing process and an increase in temperature sensitivity. Moreover, passive isolators are isolation frequency dependent, and sensitive to system disturbances that change the operational frequency.

This thesis introduces elastic network vibration isolators, defined as a system of flexible elements that are designed and connected in a way to reduce the vibrations across the system from input to output. This class of isolators is based on the principle of antiresonance, where inertial forces cancel stiffness forces, leading to isolation at a tuned frequency. Two stacking methods for flexible elements are explored, namely, parallel and series stacking. It is shown that parallel-stacked beam network isolators overcome some of the basic challenges of passive isolation, namely High-Static-Low-Dynamic-Stiffness (HSLDS) behavior combined with low frequency isolation. Due to their continuous system characteristic, beam network isolators exhibit multiple interesting features, such as, multimode isolation frequencies, and multi-isolation frequency clustering, even at low frequencies.

Using a beam-network design, a modified Dynamic Antiresonant Vibration Isolator (DAVI) with a flexible lever is introduced. An analytical model predicts that a compliant lever design can provide the same isolation frequency as that of a rigid DAVI but with half the auxiliary mass. The analytical model also shows that for the same auxiliary mass, compliant levers can provide lower isolation frequencies compared to DAVIs with rigid levers. The proposed isolator includes monolithic compliant features that are realizable with additive manufacturing, which reduces friction and wearing losses compared to traditional isolators. Two fabricated and tested devices validate the model and demonstrate the improved performance of a flexible design. The validated analytical model is used to design an isolator with elastomeric features to meet industry standard specifications. A proof-of-concept isolator is fabricated, and it is experimentally shown that the rubber-based isolator can provide 93% reduction in stiffness at the tuned isolation

frequency, in-line with theoretical predictions.

Series stacking is explored for beam and plate elements. This thesis introduces nodal beam stack isolators, consisting of symmetric stacks of beams with tip masses connected in series via compliant hinges near nodal points. An analytical model is derived to predict the vibration behavior of a beam stack. It is shown that nodal beam stacks are capable of generating multiple bandgaps, (isolation over a frequency range as opposed to single frequency isolation) even at low frequencies. An isolator with four beams is designed to provide a band gap of 32 Hz with a center frequency at 72 Hz. A Polylactic acid polymer prototype is 3D printed and the frequency response of input force to transmitted force is experimentally measured showing a large 41 Hz band gap with a center frequency also around 72 Hz. The experimentally validated model is used to design a 10 beam isolator with a low frequency band gap from 10 to 86 Hz, and a high frequency band gap from 202 to 543 Hz. An experimental study shows that band gap effectiveness can be affected by rotational modes that are induced by load path misalignments, which reflects on the sensitivity of real life band gaps to small load path disturbances, as opposed to analytical band gaps that are generally deeper.

Moreover, this thesis introduces plate stack isolators, consisting of axisymmetric stepped plates stacked in series and connected using compliant hinges. A Kirchoff-Love Plate model predicts the frequency response, and it is shown that these isolators are also capable of broadband vibration isolation over multiple frequency ranges. Additively manufactured polymer 4-plate and 2-plate isolators, show that multiple bandgaps can be achieved by model based tuning of plate geometries. The experimentally validated model predicts that metal isolators manufactured with Laser Powder-Bed fusion can achieve low frequency bandgaps and other design metrics of commercially available vibration isolators.

The use of compliant hinges allows for a monolithic design of elastic network isolators (both beams and plates), which eliminates friction, leading to deeper stop bands and larger cycle lives. Elastic network isolators have a fairly complex structural design which could not be manufactured with traditional manufacturing methods. This thesis shows that additive manufacturing can be used to realize complex structures with a favorable dynamic performance.

Table of Contents

List of Figures

List of Tables

Acknowledgments

I would like to extend my gratitude to my co-advisors Dr. Christopher Rahn and Dr. Edward Smith. Your outstanding mentorship over the past years has helped me grow as a researcher, and more importantly, as a person. Your approach to problem solving has really been inspiring, and your guidance has always led me to a better place than where I was a step before. I am very grateful to have Dr. Steve Hambric and Dr. Joseph Najem on my dissertation committee; their research suggestions have always been constructive.

I would also like to thank Dr. Conor Marr from Parker LORD for his constant support, and for his insightful input on this work throughout all its stages. I would like to thank Parker LORD for funding this research.

I would also like to thank my labmates (current and previous) for making my day-to-day lab experience much more enjoyable, and easy going: Dr. Tahzib Safwat, Dr. Jun Ma, Dr. Mihir Parekh, Shuhua Shan, Valentin Lanari, Mike Trowbridge, Matthew Lenko, Kiran Bhaskar, Changik Cho, Nitisha Ahuja, Seth Kelley, Gabriel Worman, and Quentin Vaira.

Lastly, I'd like to thank my family for their constant support and encouragement.

Chapter 1

Introduction

Passive vibration isolators are often used to mitigate the effect of undesired vibrations by reducing the transmissibility between the vibrating object and the isolated body. With the increase in human comfort standards in vehicles and other motion-based utility devices, as well as the advance of complex high disturbance systems, and high precision instruments, vibration isolation has consistently been a high interest topic to meet the needs of the industry. In the following sections, different types of isolators are introduced, the state of the art, as well as the advantages and disadvantages of each type of isolator are discussed.

1.1 Linear Passive Vibration Isolators

Isolators are placed between the vibrating source and the isolated object; they are usually part of the load path. They usually protect a system foundation from disturbances caused by harmonic excitations or rotating imbalances. Alternatively, they can be used to protect an object from the disturbances caused by base excitations. Linear isolators are usually composed of a load bearing element and an energy dissipating element as shown in Figure 1.1-a . In many cases a single element, such as a rubber pad, can perform both load bearing and energy dissipating functions [1]. Typical linear isolators attenuate

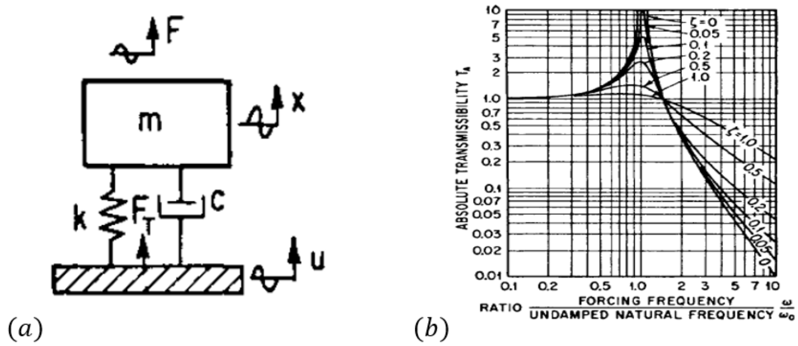

Figure 1.1. Schematic of a linear vibration isolator (a) and its corresponding transmissibility response (b) from [1]

vibrations for frequencies exceeding $\sqrt{2}\omega_n$, where ω_n is the undamped natural frequency, and they perform better as the damping ratio decreases, as shown in Figure 1.1-b. The theory of passive linear vibration isolation is well documented in the literature [17–19].

Another class of linear isolators are Dynamic Antiresonant Vibration Isolators (DAVIs) [20], these isolators consist of an inertially coupled system with a mass-lever combination where the inertial forces cancel spring induced forces, allowing for zero transmissibility between the isolated mass and the vibrating base, at a specific frequency, as shown in Figure 1.2. The isolation frequency is independent of the isolated mass, thus they are very useful in applications where the isolated mass is subject to changes, such as isolation of components, passenger seats, cargo, and deck isolation. They have also been extensively investigated and used for several helicopter applications [21–26]. Based on the DAVI, the Eurocopter company developed the SARIB system to protect the helicopter fuselage from gearbox vibrations. Other applications include propeller vibration isolation systems [27], and floor-machine isolation [28]. Researchers have also investigated different variations of the DAVI system, for example, Liu *et. al* [29] introduced a DAVI with an X-shaped supporting structure as the stiffness element which yielded an improved low frequency broadband isolation. Yilmaz and Kikuchi [30] studied a 2 degree of freedom DAVI that shows a wider stop-band region compared to a traditional DAVI. Kim and

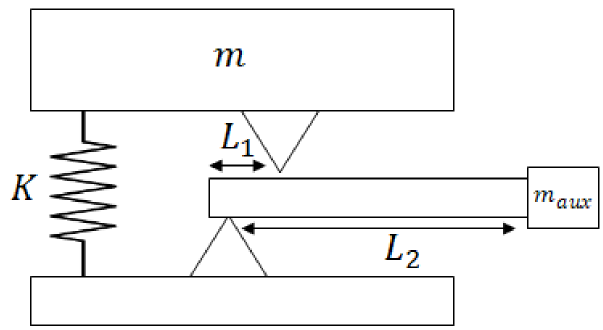

Figure 1.2. Schematic of a dynamic antiresonant vibration isolator.

Figure 1.3. Photograph of a self-tuning DAVI being excited at 25 Hz from [2]

Kang [31] introduced a V- shaped folded lever DAVI. Yan *et. al* [32] proposed a DAVI with eddy current damping that exhibited a wider isolation band. Similarly, a DAVI with eddy current damping and a magnetic spring is shown to have quasi-zero stiffness characteristics in [33]. Ozyar and Yilmaz [2] introduced a self-tuning DAVI, that adapts to variations in operational frequency by mechanically changing the DAVI amplification ratio. A photograph of the self-tuning isolator is shown in Figure 1.3. Rivin [34] shows that the transverse vibrations can be transformed to rotational movements that induce an inertial antiresonance force which leads to isolation.

Another type of inertial coupling that is often used is based on hydraulic flow.

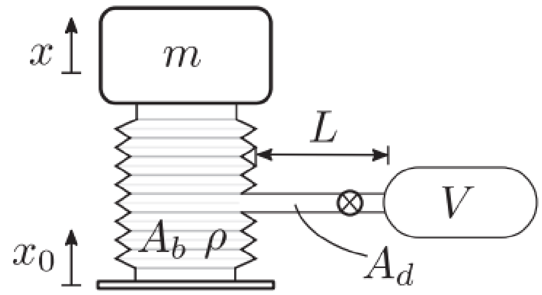

Figure 1.4. Schematic of a Goodwin vibration isolator obtained from [3]

Goodwin [35] introduced hydraulic inertial isolators by using elastic bellows connected to a fluid vessel as shown in Figure 1.4, the inertial flow of the fluid creates a counter force that contributes to vibration isolation. Therefore, the fluid flow in this case would be the analogue of the mass oscillations in the classic DAVI. Hydraulic isolation principles were then extensively used in engine mount designs [36–39]. Scarabourgh *et al.* [40] introduced a new class of fluid-based inertial vibration isolators by coupling fluidic matrix composites to an air pressurized fluid port. Fluidic matrix composite isolators were then studied for several helicopter applications [41, 42].

The use of fluid as opposed to a solid mass in the DAVI has led to a reduced weight and size penalty. The classic DAVI often requires a large amplification ratio when the there is a high static stiffness requirement coupled with low frequency isolation. The amplification ratio in the fluid analogue of the DAVI is dependent on the fluid track geometry in the device. This has led to compact fluidic isolator designs compared to the DAVI such as the Liquid Inertia Vibration Eliminator introduced by Bell Helicopter and shown in Figure 1.6. As vibratory forces are applied on the pylon, the fluid that is pumped through the tuning port is displaced in the inertia track, leading to oscillatory accelerations that induce pressure and inertial forces out of the phase with the input vertical force, thus leading to dynamic force cancellation and isolation. The amplification ratio in this case will be the ratio of the outer cylinder area to tuning port area. High

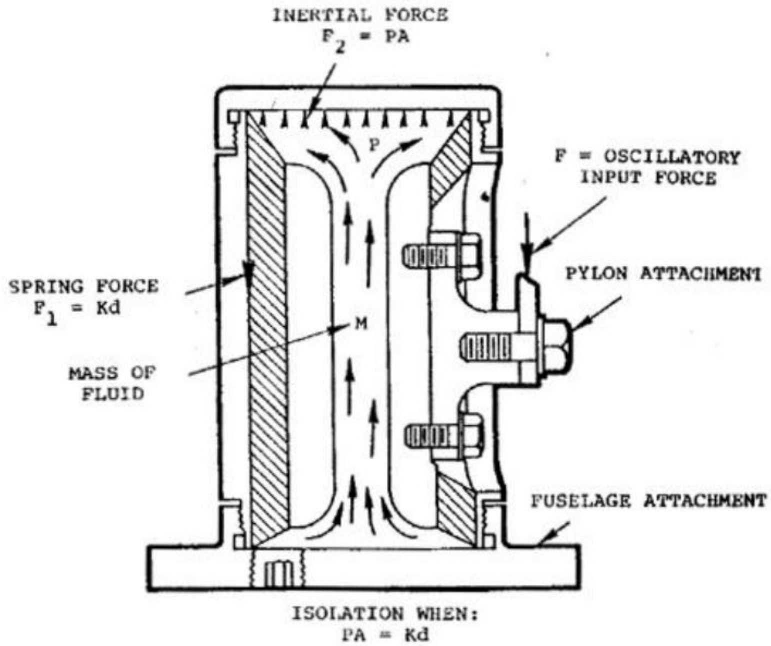

Figure 1.5. Section view of the Liquid Inertia Vibration Eliminator (LIVE) from [4].

density fluids such as mercury are often used to achieve higher inertial forces.

Inertial isolators became more feasible for helicopter applications due to Fluidlastic technology, which combines fluid inertia tracks and bonded elastomeric elements [6]. Similar to the LIVE system, this technology includes two fluid chambers filled with a high-density fluid, connected via a reduced section inertia track, resulting in an amplified inertial force [43]. Fluidlastic pylon isolators introduced by LORD corporation [6, 44] have a compact design, as shown in Figure 1.7. They also exhibit impressive dynamic characteristics compared to their size, thus making them suitable for helicopter applications. Han *et al.* [45] proposed using Fluidlastic isolators for pitch link load reduction in helicopters.

Fluidic isolators have some drawbacks compared to a fully mechanical design. For instance, bubble formation in the inertia track can lead to a change in the fluid bulk modulus, resulting in deviations from the tuned isolator behavior. Therefore, these

Figure 1.6. Fluidlastic Technology used on the rotor hub of CH-47 Chinook helicopter [5]

isolators require a complex manufacturing process to prevent air bubble formation in the fluid track. Leaking problems primarily caused by cavitation can lead to isolator performance deficiencies. Also, proper fluid insulation is often required to prevent the entrapment of small solid particles as the isolator is being used, leading to more design requirements. Furthermore, these fluids are often tuned to operate in a given thermodynamic environments, which means that these isolators are thermally sensitive and their performance will change if operated under different conditions.

1.1.1 Research Objective 1

Nonfluidic antiresonant isolators typically have noncompact, high volume designs, often with a very high weight penalty. On the other hand, Fluidlastic vibration isolators typically trade improved isolation, performance, and footprint over strictly elastomeric or other typical mechanical designs for a more complex manufacturing process and a potential increase in temperature sensitivity. This research aims to find solutions to

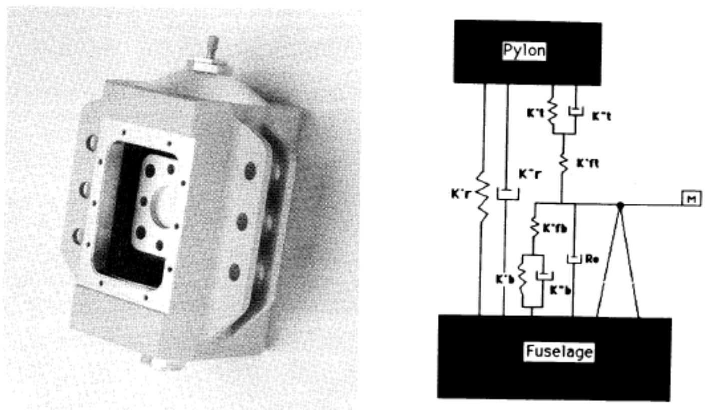

Figure 1.7. Schematic of a Fluidlastic pylon vibration isolator obtained from [6]

design compact, fluid-free isolators, with a dynamic performance that is comparable to that of a fluidic isolator.

1.2 Nonlinear Passive Vibration Isolators

Conventional linear isolators are mainly used when the natural frequency is well away from the operating frequency, that is, to ensure a reduced transmissibility near the operating frequency range. Furthermore, linear isolators often trade load bearing capability with low dynamic stiffness, this effect is much more pronounced on lower isolation frequencies. Typically, low frequency linear isolators are very soft, and are prone to a poor performance when subject to system disturbances [46]. Due to their soft nature, their corresponding resonant frequency is very low, making them highly unstable. Therefore, there is a lot of interest in designing high-static-low-dynamic-stiffness (HSLDS) isolators that can provide low frequency isolation with a high static stiffness. High static stiffness is usually a design requirement for many applications whereby the isolator is placed in a critical connection point in the load path, such as helicopter gearbox-air-frame isolation where the fuselage is hanging on the rotor-hub via the isolator connections (see Figure 1.8).

HSLDS isolators often have nonlinear stiffness, which can be accomplished by com-

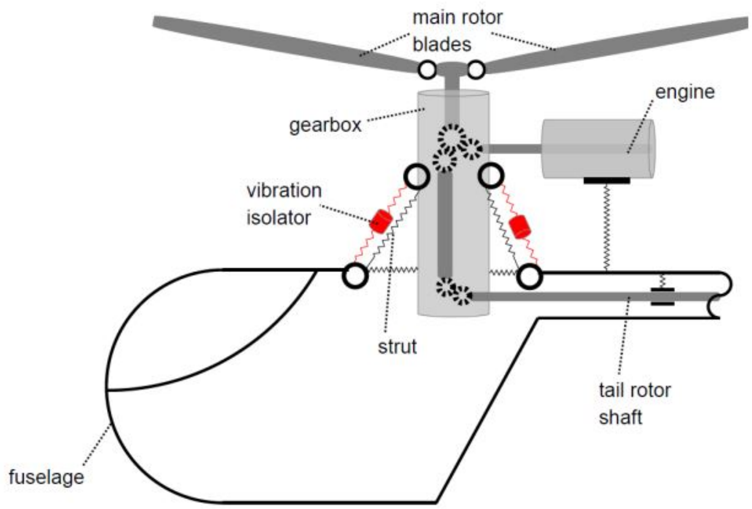

Figure 1.8. Schematic showing the vibration isolator placement on gearbox strut in a helicopter, from [7]

bining positive stiffness and negative stiffness elements. Positive stiffness is when the opposing force increases with an increase of displacement. On the other hand, negative stiffness can be described as a decrease in opposing force with an increase displacement. In essence, negative stiffness is when a force is applied on a structure and the structure pulls away in the same direction. Therefore, by combining a negative stiffness and a positive stiffness element, a quasi-zero stiffness behavior can be obtained, leading to zero force output for a given displacement input. The negative stiffness element is used to provide isolation by decreasing the dynamic stiffness, while the positive stiffness element withstands most of the static load and provides stability [47]. One popular way to achieve HSLDS isolation is by combining a negative stiffness Euler beam with a linear spring, as shown in Buckled beams exhibit negative stiffness behavior as shown in Figure 1.10 (curve 3) where the opposing force is decreasing with applied displacement in the working range. . The overall isolator force-displacement behavior seen in Figure 1.10 is the combined behavior of the beam and the spring. It is seen that there is a zero-slope behavior in the working range, indicating quasi-zero stiffness.

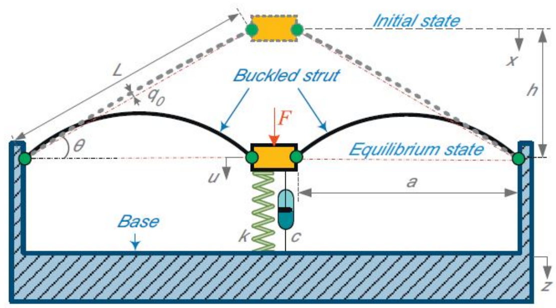

Figure 1.9. Graph showing the force vs displacement behavior of a linear spring (curve 1) and a buckled beam (curve 3) and their combined behavior (3) [8]

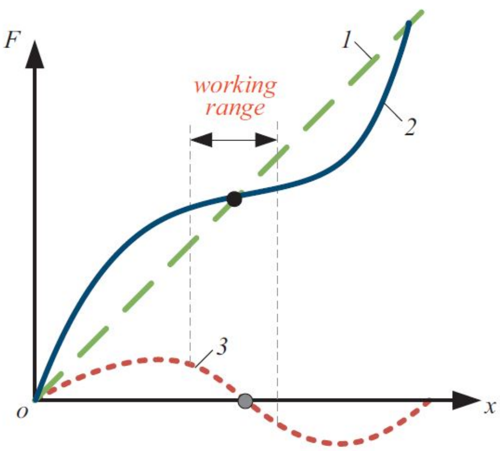

Figure 1.10. Graph showing the force vs displacement behavior of a linear spring (curve 1) and a buckled beam (curve 3) and their combined behavior (3) [8]

Liu *et al.* [48] proposes a negative stiffness isolator that achieves HSLDS behavior by combining a linear spring with a negative stiffness buckled Euler. Oyelade [49] investigated the use of a Euler buckling beam negative stiffness vibration isolator for vehicle comfort and found that the isolation frequency range is much larger than that of a linear isolator. Lu *et al.* [50] proposed a circular ring HSLDS vibration isolator. Shaw *et al.* studied a bistable plate HSLDS isolator. Somnay *et al.* [51] presented the Gospodnetic-Frisch-Fay beam mounted on two knife edge supports, as a nonlinear vibration isolator. Ibrahim *et al.* [46] analyzed the Gospodnetic-Frisch-Fay beam in [51] as mounted on

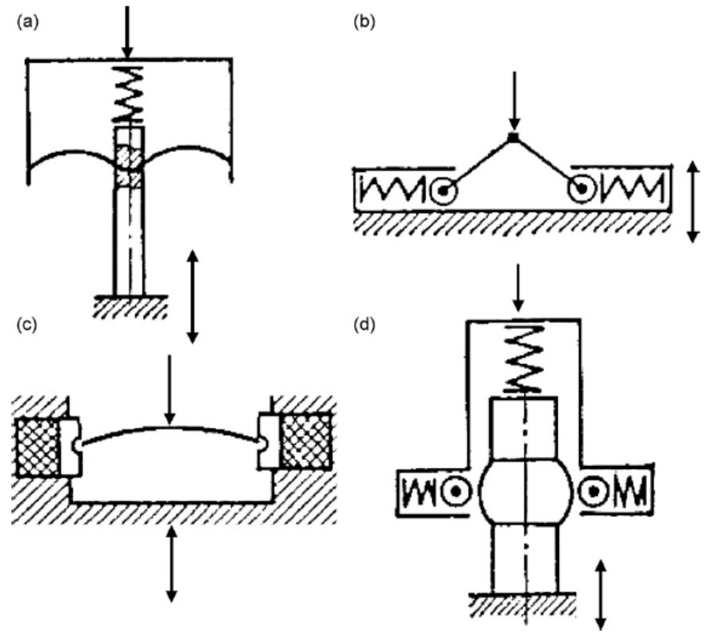

Figure 1.11. Schematic diagrams of different HSLDS mechanisms (a) shows a spring with two buckles beams (b) shows a double link restrained by horizontal springs (c) shows a buckled beam isolator (d) shows a vertical and horizontal spring system [9, 10]

frictional supports, it was found that the transmissibility performance is improved for post resonant excitation frequencies because of the addition of friction. Huang *et al.* [8] found that the sliding beam in [51] exhibits negative stiffness characteristics and suggested a nonlinear vibration isolator consisting of a sliding beam coupled with a linear spring [8]. Nonlinear stiffness can also be obtained by scissor-like or X-shaped structures [52, 53], or by connecting three oblique springs to the same node [47, 54–57]. Different HSLDS mechanisms are shown in Figure 1.11 .

Nonlinear isolators generally operate near a displacement equilibrium point where the dynamic stiffness is very low in its proximity. Moreover, these isolators often behave like a duffing isolator with a curved resonance peak as seen in Figure 1.12. This is usually associated with Jump Phenomenon where the frequency response is sensitive to the frequency sweep direction, this can be seen in Figure 1.12 where the response jumps down from high to low amplitude between range 2 and 3 as the frequency goes from

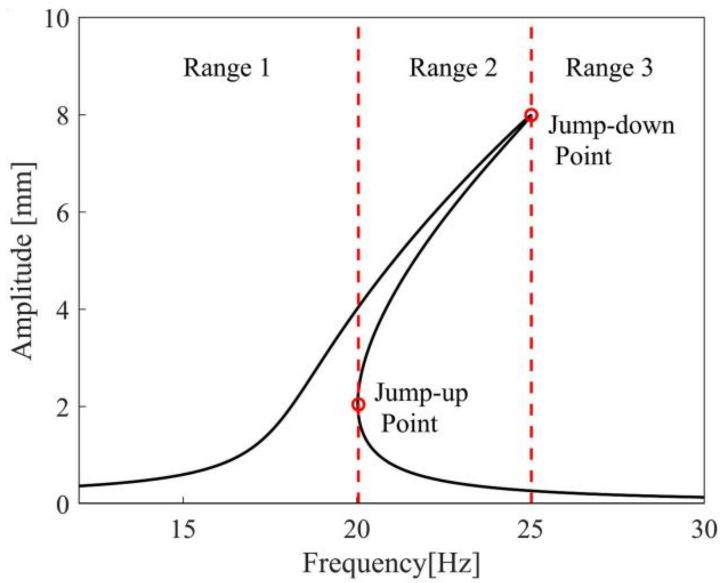

Figure 1.12. Frequency response graph showing jump phenomenon from [11]

left to right. Alternatively, the response jumps up from low to high amplitude at the jump-up point between ranges 1 and 2.

1.2.1 Research Objective 2

The displacement dependence of nonlinear isolators makes them highly sensitive to high displacement loads, where any deviations from the displacement envelope will lead to disruptive and even abrupt isolator behavior. Furthermore, jump phenomenon creates stability issues near the resonance frequency region [47]. This research aims to find solutions to design HSLDS isolators that are capable of low frequency isolation, such that they are not sensitive to displacement variations, or possess nonlinear stability characteristics.

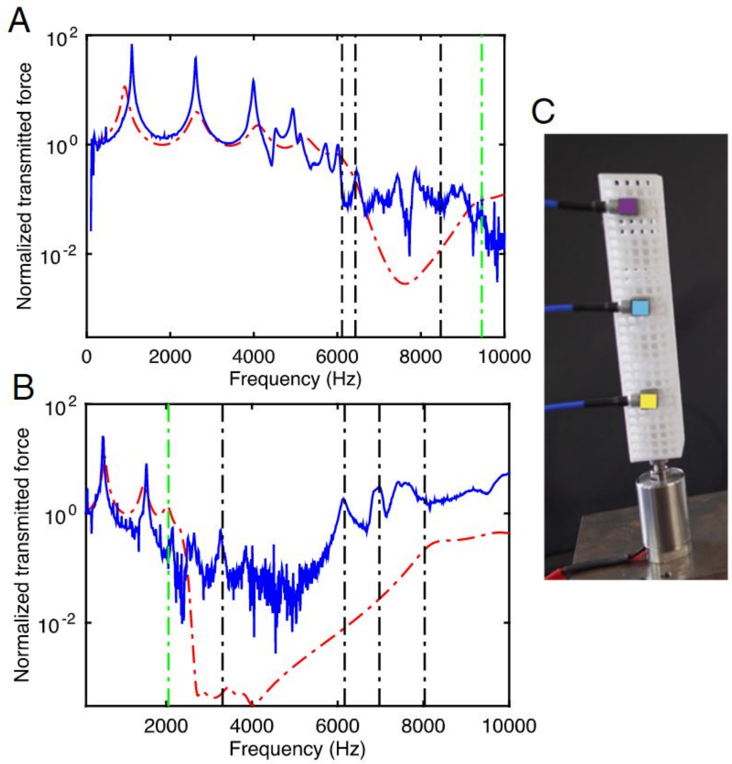

Figure 1.13. (A-B) Show simulated and experimental frequency responses for high and low stiffness metamaterial structures, (C) is an image of the experimental setup [12]

1.3 Band Gap Isolation

Isolators are usually tuned to operate over a limited frequency range, making the isolator performance sensitive to operating frequency variations. Band stop or band gap vibration isolators have a larger stop band frequency range making them less susceptible to disturbance frequency variations. This becomes very critical in applications where unwanted disturbances may occur through shocks and random excitation with a wide frequency spectrum [58], or applications with multiple operational frequencies, such as machines with multiple speeds or gearbox vibration isolators whereby vibrations occur at multiple gear mesh frequencies [59]. Band gap vibration isolation can be accomplished using periodic structures with Bragg scattering or local resonances. Bragg scattering periodic structures have a high impedance mismatch to achieve destructive interference

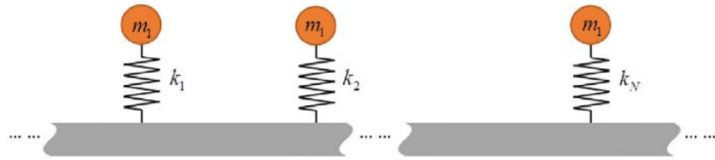

Figure 1.14. Graded local resonators on a beam from [13]

between the transmitted and reflected elastic waves to create a vibration or acoustic band gap [12, 60, 61]. Bragg scattering techniques are suitable for high frequency applications due to the small scale of the periodic structures [62] . An example of a metamaterial with band gap behavior can be seen in Figure 1.14.

The need for low frequency bandgaps has led to the development of locally resonant phononic crystals (PCs) [63]. Locally resonant structures embedded in periodic arrays absorb vibration energy, thus creating a stop band at their local resonant frequencies. Combining Bragg scattering and local resonators can achieve low frequency bandgaps [64–66].

Local resonators can be mounted on a structure subject to vibratory loads. By tuning each resonator to resonate at a different frequency, the vibrations will be absorbed at the tuned resonance frequencies, thus leading to a vibration band gap in the tuned frequency range. Figure 1.14 Nobrega [67] *et al.* introduce a metamaterial rod with periodic local resonator attachments to achieve vibration bandgaps. Wang *et al.* [68] proposed a metamaterial rod with embedded negative-stiffness resonators to generate low frequency bandgaps. Wu *et al.* [69] used high-static-low-dynamic-stiffness X-shaped local resonators. Sun *et al.* [70] introduced a periodic metamaterial structure consisting of several spring mass damper combinations mounted on an isotropic beam. Lu *et al.* [71] proposed a rolling ball local resonator metamaterial that is capable of vibration isolation and energy harvesting. Wu *et al.* [69] showed that X-shaped structures can be used as local resonators on a metamaterial beam for broadband vibration isolation. Hu *et al.* [13] proposed a graded metamaterial beam with spring-mass local resonators tuned

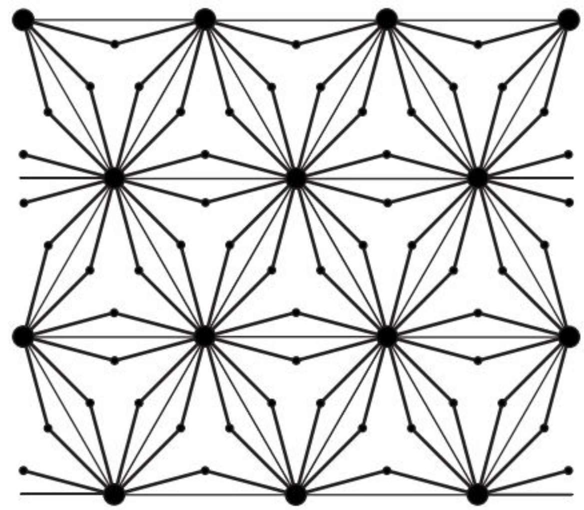

Figure 1.15. Metamaterial local resonator lattice with lever-type inertial amplification [14]

for broadband vibration isolation. El-Borgi *et al.* [72] introduced a periodic metamaterial structure consisting of several cross-connected beam-mass local resonators mounted on an isotropic beam. Similarly, researchers use vibration neutralizers as local resonators on beam structures [73–75].

Low frequency band gap vibration absorbers often use heavy added masses, incurring high weight penalties [76, 77]. Inertial amplification had been used to reduce added mass. Amplification mechanisms can significantly increase the inertial forces, thus leading to a lower mass penalty. Figure 1.15 shows a lever type inertial mechanism embedded in a metamaterial structure. Szefi *et al.* [78] introduced a high frequency periodically layered helicopter isolator with inertial fluid elements in a metal-elastomer layered isolator. Yilmaz *et al.* [14] showed that inertial amplifiers in a lattice truss structure provide a wide band gap at low frequency with a lower weight penalty compared to locally resonant periodic structures. Frandsen *et al.* [79] showed that a rod with periodically attached inertial amplifiers generates the same band gap as a standard local resonator at low frequency but with twenty times less mass. Li [80] utilized periodic metamaterials made from scissor or X-shaped structures with an inertial amplification mechanism.

Zhu *et al.* introduced a plate composed of periodic cantilever-mass microstructures to suppress low frequency flexural waves. Miranda *et al.* [81] introduced a metamaterial elastic plate with periodically attached multiple degree of freedom resonators to suppress flexural waves. Periodic arrays of mass screws *et al.* [82], spring-mass *et al.* [83] have been investigated.

Lever-type dynamic antiresonant vibration isolation (DAVI) systems amplify the inertial forces using a lever and mass to cancel stiffness forces and create an antiresonant frequency [9, 20, 84, 85] . Yilmaz and Kikuchi [30] showed that placing DAVI type isolators in series results in multiple antiresonant frequencies, creating a band gap. Liu *et al.* [76] generated a band gap with an X-shape supporting structure embedded in a 2-DOF lever type system consisting of two DAVIs connected in series. The nonlinear characteristics of the X-shape structure enhances the overall isolation performance in the band gap frequency range. Kim and Kang [31] introduced a biologically inspired V-shaped antiresonant lever type isolator with a relatively narrow band gap as compared to placing several DAVIs in series.

1.3.1 Research Objective 3

Metamaterial-based isolators have been shown to work on bench-top testing, however they are not used for practical isolation applications. This is caused by complex metamaterial structures with little load bearing capacity, or simply because they are too soft (small stiffness). Other bandgap isolators based on periodic placement of antiresonant elements, such as the multilayered DAVI [30], are very difficult to manufacture, and are often made from several parts. Their multi-part nature creates several wearing and friction problems on sliding surfaces. Additionally, typical band gap isolators generate a single band gap frequency. This research aims to find solutions to design practical broad band gap isolators with multi-band gap generation ability, with no friction or wearing concerns.

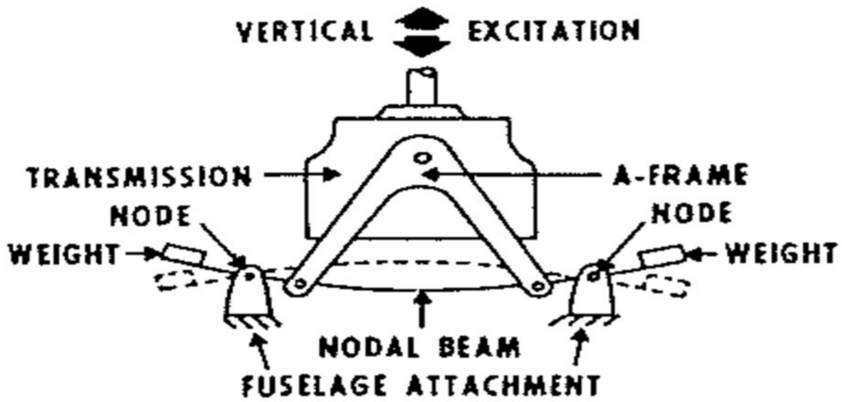

Figure 1.16. Metamaterial local resonator lattice with lever-type inertial amplification [15]

1.4 Background on Beam-based Isolators

Vibration isolators are usually characterized as discrete dynamic systems consisting of elastic spring and damper elements. However, discrete system modeling often fails to capture system nonlinearities and complex elastic modes, or cross axis coupling terms that are highly effective at high frequencies [86]. Thus, there has been a growing interest in designing and analyzing vibration isolators as continuous dynamic systems. Ding et al. studied the force transmissibility of viscoelastic beams [87] and pre-pressed beams [88], both mounted on elastic supports and under transverse loading conditions and found that effective isolation frequencies become much smaller if the elasticity of the beam and/or the elasticity of the boundary supports are considered. Snowdon [89] showed how force transmissibility across a bream is highly affected by its mass loading conditions. Lim *et al.* [90] proposed a cantilever beam vibration absorber for vibration reduction in an optical disk drive using finite element analysis and lumped parameter models.

Beams analyzed as continuous dynamic have also been analyzed in the context of antiresonance vibration isolation. Beams have an inherent inertial and elastic profile, and therefore, inherent antiresonant characteristics, making them the continuous system analogue of the discrete system DAVI. To achieve low frequency isolation additional masses can be attached so the beam acts as a low frequency vibration isolator [91]. A well-known beam isolator application is the Bell NodaMatic isolator which utilizes the nodalization concept to isolate the helicopter from gearbox vibrations [92, 93]. Nodalization involves mounting the beam on two symmetric nodal points such that there is zero force/displacement transmissibility at the antiresonance frequency [94–96]. Figure 1.16. This concept has also been applied on helical springs [97].

1.5 Research Contributions

The research contributions for each chapter (2-6) are summarized:

- Chapter 2: The isolation behavior in continuous beams is investigated using an analytical closed form transfer function approach. It was analytically and experimentally proven that the addition of a tip mass greatly reduces the shear isolation frequency of a cantilever beam. Thereafter the concept of stacking beams in parallel is explored. Results show that High Static Low Dynamic Stiffness (HSLDS) can be obtained, even at low frequencies. Furthermore, multiple isolation frequencies are achieved with the same isolator, yielding a new isolator feature. HSLDS behavior is obtained without the drawback of nonlinear behavior (displacement dependency, instability, jump phenomenon). Therefore, this chapter addresses objectives 1 and 2.

- Chapter 3: A flexible-lever DAVI is introduced based on the concept of parallel stacking using beam networks. A dynamic model to predict the force transmissibility is developed and experimentally verified. The flexible lever DAVI achieves a lower isolation frequency as compared to a classic DAVI with the same mass-penalty. The isolator is fluid-free, compact, and monolithic which eliminates friction wearing and leads to a potential longer shelf-life. This chapter addresses objective 1.

- Chapter 4: A new parallel stacked beam network with elastomeric features is introduced and designed to meet industry specifications. A proof-of-concept isolator is fabricated and used to validate the analytical model. The proposed low frequency isolator is compact, fluid free, and exhibits high static stiffness low dynamic stiffness behavior, thus addressing objectives 1 and 2.

- Chapter 5: Series beam stacking is explored, and a monolithic, compliant beam-network vibration isolator is introduced. An n-n beam analytical model is introduced to predict the force transmissibility. The analytical model is experimentally validated and used to design isolators with several broad band gaps. The monolithic nature of this isolator reduces friction and wearing problems. Furthermore, this isolator can be additively manufactured and can generate multiple band gaps, thus addressing objective 3.

- Chapter 6: Series stacked plate networks are introduced. Several mass-loaded plates connected via flexure hinges compose a plate-stack. An n-n plate analytical model is developed to predict the dynamic response of the stack. The model is experimentally verified to a high degree of accuracy. The plate-stack isolator is shown to be capable of generating multiple broad band gaps. The monolithic design is additively manufactured (AM), which shows the advantages of using AM technology to realize parts with complex structures with favorable dynamic characteristics, which would be otherwise difficult to manufacture with traditional manufacturing. The plate design makes these isolators much stiffer in tilting direction and off-axis modes. This chapter addresses objective 3.

Chapter 2

Parallel-Stacked Beam Network

2.1 Parallel Stacking

Parallel-stacked beam network isolators are defined as beams grouped together and rooted to the same support, subject to the same input, and tuned to provide an overall isolation at a single frequency, or multiple isolation frequencies. There are two main advantages for using beam networks rather than a single beam vibration isolator:

1. Superposition: The total transmitted force is the equivalent of the total shear force reaction of all the beams. This is useful to scale the overall stiffness, or the transmissibility reduction ratio, while keeping the same isolation characteristics of the system. For example, a single beam might be a good fit to provide isolation at a certain frequency, however it might not be stiff enough. Therefore, adding another beam-mass combination will double the stiffness while maintaining the same natural and isolation frequency, and force reduction ratio.

2. Clustered Isolation: Since beams are continuous systems, they can exhibit multiple isolation frequencies, allowing for flexible tuning for isolation at multiple frequency ranges across multiple beams.

The proposed beam network isolator is composed of two sub-components, each with

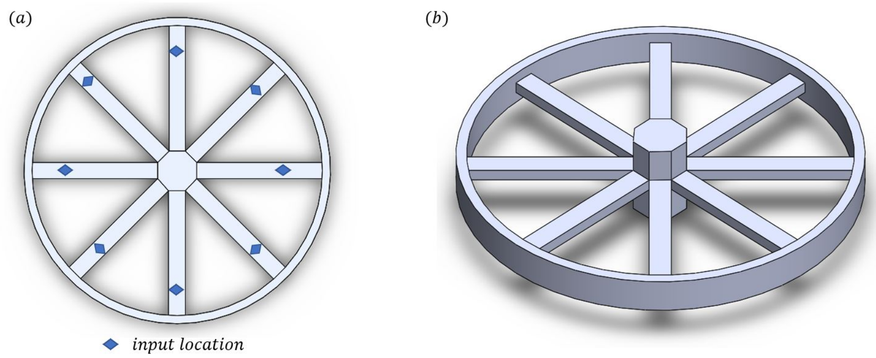

Figure 2.1. Diagram of a Beam network isolator with all the beams connected to the same and rooted to the same support and subject to the same input (a) is a top view (b) is an isometric view.

specific features. The sub-components are analyzed in the section below in the context of point-displacement excitation as well as point-force excitation.

2.1.1 Beams Connected to the same mass

An efficient method to increase the isolator stiffness while maintaining the same natural and isolation frequency of the system is to connect multiple beams to a single mass as shown in Figure 2.1. This will allow for a synchronous motion of the middle mass. The middle mass connection will enforce a zero-slope connection to the beams, thus allowing for a high overall stiffness as compared to a configuration of beams each attached to an independent tip mass. If all the beams were identical, the overall frequency response of the sub-component will be proportional to that of a single beam-mass. Each beam connected to the same mass can be modeled as a sliding beam with a fixed root, and a zero-slope sliding condition on the other end. Figure 2.2 shows a beam of length L and with an input displacement at a distance L_1 from the root. To model an input displacement, the beam will be split into two parts, each part with a governing Euler Bernoulli differential equation, the two equations are coupled with the continuity and the input displacement boundary conditions. Figure 2.2 shows a uniform cross sectional

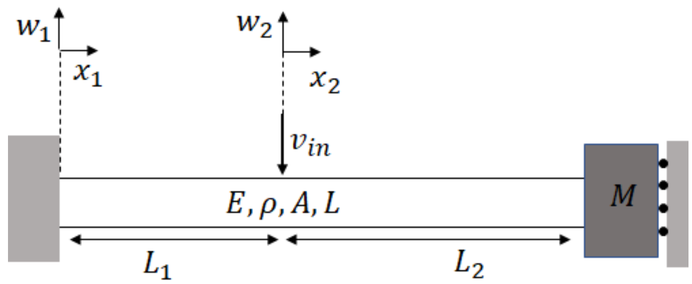

Figure 2.2. Diagram of a Beam with a sliding mass under a displacement input v_{in}.

sliding beam divided into two parts, with lengths L_1 and L_2, such that w_1 and w_2 are defined as the transverse beam displacements, for each part. The Euler Bernoulli beam equation is written as:

$$EI\frac{\partial^4 w_i}{\partial x_i^4} + \rho A\frac{\partial^2 w_i}{\partial t^2} = 0 \tag{2.1}$$

With i denoting the specific part of the beam, in this case $i = 1, 2$. E^* is the complex Young's modulus,

$$E^* = E(1 + j_{im} tan\delta), \tag{2.2}$$

where tan $delta$ is the loss tangent such that,

$$tan(\delta) = \frac{E''}{E}. \tag{2.3}$$

E is the Young's modulus (storage modulus) and E'' is the loss modulus, $j_{im} = \sqrt{-1}$. The complex Poisson's ratio v^* is assumed to be equal to the real Poisson's ratio v, based on [98].

The following non-dimensional variables are introduced, $\bar{x}_i = x/L_i$, $\bar{w}_i = w_i/L_i$ and $\bar{t}_i = ct/L_i^2$ where $c = \sqrt{\frac{E^*I}{\rho A}}$. The non-dimensional form of equation (2.1) becomes,

$$\frac{\partial^4 \bar{w}_i}{\partial \bar{x}_i^4} + \frac{\partial^2 \bar{w}_i}{\partial \bar{t}_i^2} = 0, \tag{2.4}$$

Taking the Laplace transform of (2.4) in the $\bar{t}_i$ domain yields

$$\frac{\partial^4 \bar{W}_i}{\partial \bar{x}_i^4} + s_i^2 \bar{W}_i = 0, \tag{2.5}$$

$W_1(x,s)$ and $W_2(x,s)$ are defined as the Laplace transforms of $w_1(x,t)$ and $w_2(x,t)$, respectively. The displacement transfer function can then be introduced as,

$$G_i(x_i, s_i) = \frac{W_i(x_i, s_i)}{V_{in}(s_i)} \tag{2.6}$$

where $V_{in}(s_i)$ is the Laplace transform of the input displacement $v_{in}(t)$ at $x_i = L_i$ and $x_{i+1} = 0$. The non-dimensional input displacement is then introduced as $\bar{v}_{in} = v_{in}/L_i$, and in the Laplace domain as,

$$\bar{V}_{in}(x,s) = \frac{V_{in}(x,s)}{L_i} \tag{2.7}$$

The non-dimensional transfer displacement transfer function is then introduced as

$$\bar{G}_i(\bar{x}_i, s_i) = \frac{\bar{W}_i(\bar{x}_i, \bar{s}_i)}{\bar{V}_{in}(\bar{s}_i)} \tag{2.8}$$

with $\bar{W}_i = W_i/L_i$. Replacing eq. (2.8) in (2.4), and taking $s_i = j\bar{\omega}_i$ where $\bar{\omega}$ is the non-dimensional excitation frequency, the transfer function ODE can be written as,

$$\frac{\partial^4 \bar{G}_i(\bar{x}_i, \bar{\omega}_i)}{\partial \bar{x}_i{}^4} + \beta_i^4 \bar{G}_i(\bar{x}_i, \bar{\omega}_i) = 0 \tag{2.9}$$

such that $\beta_i^4 = \bar{\omega}_i^2 = \omega^2 L_i^4/c^2$. The non-dimensional boundary conditions are then written as,

$$
\begin{aligned}
&\bar{G}_1(0,\bar{\omega}_1) = 0, \left[\frac{\partial \bar{G}_1(0,\bar{\omega}_1)}{\partial \bar{x}}\right]_{\bar{x}=0} = 0,\\
&\bar{G}_1(1,\bar{\omega}_1) = 1, \bar{G}_2(0,\bar{\omega}_2) = \frac{L_1}{L_2}\bar{G}_1(1,\bar{\omega}_1)\\
&\left[\frac{\partial \bar{G}_1(\bar{x}_1, j\bar{\omega}_1)(\bar{x},\bar{\omega}_1)}{\partial \bar{x}_1}\right]_{\bar{x}_1=0} = \left[\frac{\partial \bar{G}_2(\bar{x}_2, j\bar{\omega}_2)(\bar{x}_2,\bar{\omega}_2)}{\partial \bar{x}_2}\right]_{\bar{x}_2=0},\\
&\left[\frac{\partial^2 \bar{G}_1(\bar{x}_1, j\bar{\omega}_1)(\bar{x},\bar{\omega}_1)}{\partial \bar{x}_1^2}\right]_{\bar{x}_1=0} = \frac{L_1}{L_2}\left[\frac{\partial^2 \bar{G}_2(\bar{x}_2, j\bar{\omega}_2)(\bar{x}_2,\bar{\omega}_2)}{\partial^2 \bar{x}_2}\right]_{\bar{x}_2=0},\\
&\left[\frac{\partial \bar{G}_2(\bar{x}_2,\bar{\omega}_2)}{\partial \bar{x}_2}\right]_{\bar{x}_2=1} = 0,\\
&\left[\frac{\partial^3 \bar{G}_2(\bar{x}_2,\bar{\omega_2})}{\partial \bar{x}_2^3} + \beta_2^4 \bar{M}\bar{G}_2(\bar{x}_2,\bar{\omega}_2)\right]_{\bar{x}_2=1} = 0
\end{aligned}
\tag{2.10}
$$

where in this case, $\bar{M} = M/\rho A L_2$. The solution of equation (2.9) is,

$$
\begin{aligned}
\bar{G}_i(x, j\omega) = \bar{G}_i(0, j\omega)&\left[\frac{\cosh\beta\bar{x} + \cos\beta\bar{x}}{2\beta^2}\right]\\
&+ \bar{G}_i'(0, j\omega)\left[\frac{\sinh\beta\bar{x} + \sin\beta\bar{x}}{2\beta^3}\right]\\
&+ \bar{G}_i''(0, j\omega)\left[\frac{\cosh\beta\bar{x} - \cos\beta\bar{x}}{2\beta^2}\right]\\
&+ \bar{G}_i'''(0, j\omega)\left[\frac{\sinh\beta\bar{x} - \sin\beta\bar{x}}{2\beta^3}\right].
\end{aligned}
\tag{2.11}
$$

The unknown coefficients in equation (2.11) can be found by replacing equation (2.11) in the boundary conditions (2.10). The non-dimensional dynamic stiffness at the root, defined as K_{dyn} can be calculated as,

$$
\bar{K_{dyn}} =\mid \bar{G}_1'''(0,\bar{\omega}_1) \mid \tag{2.12}
$$

The non-dimensional static stiffness is found by taking the limit of the non-dimensional

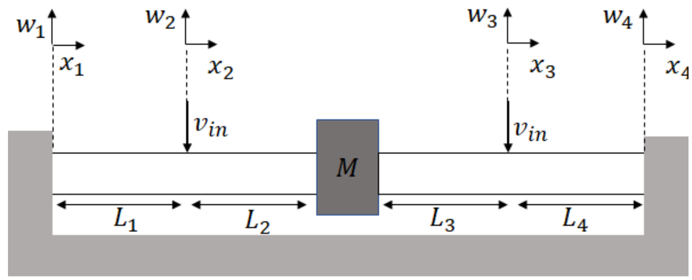

Figure 2.3. Diagram of Beam with middle concentrated mass fixed at both ends under a displacement input v_{in} at two locations.

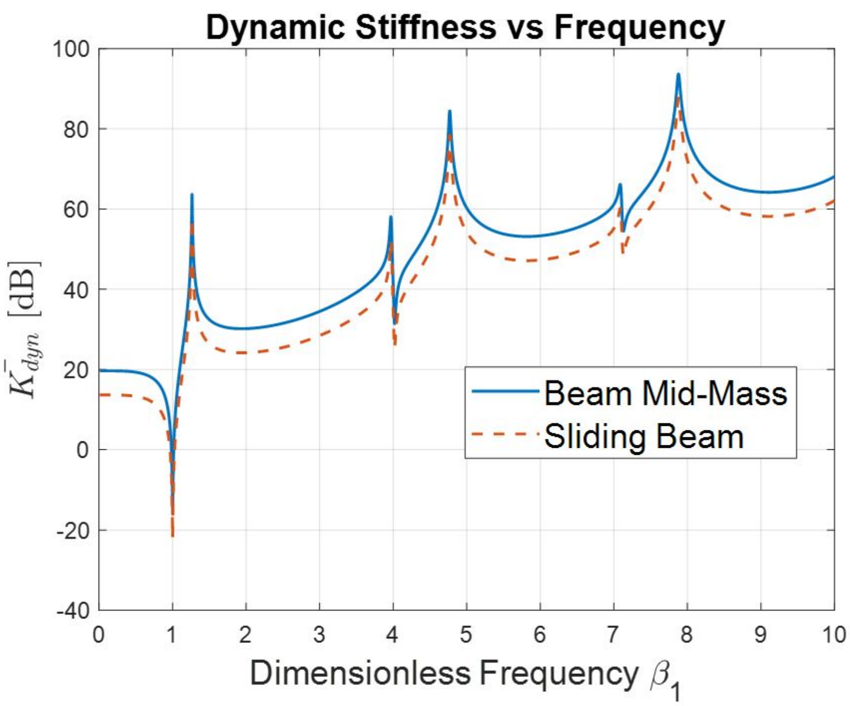

Figure 2.4. Dimensionless dynamic stiffness vs dimensionless frequency for a beam with a middle concentrated mass compared with a beam with a sliding mass with half its length and half its mid mass placed at the tip end.

dynamic stiffness at $\bar{\omega} = 0$

$$\bar{K_{static}} = [\lim_{\omega_1 \to 0} \bar{G}_1'''(0, \bar{\omega})] \tag{2.13}$$

The sliding beam is a unit element of the beam network isolator, this analytical model can be used to predict the dynamics of the entire beam network since this dynamic model is scalable. To prove scalability, the case of a beam with a concentrated middle mass subject to a zero-slope condition at its mid span is taken into consideration and compared to a sliding beam with half its length and half its mid mass placed at its tip end. Figure (2.3) shows a uniform cross-sectional beam with a concentrated middle mass, and subject to a displacement V_{in} at a distance L_1 and L_4 from the two fixed ends, respectively. The beam is divided into 4 parts for this analysis. Following the same non-dimensional scheme shown above, the non-dimensional displacement transfer function is the same as in equation (5.8) for i=1,2,3 and 4. The non-dimensional boundary and continuity conditions are shown below,

$$
\begin{aligned}
&\bar{G}_1(0,\bar{\omega}_1) = 0, \left[\frac{\partial \bar{G}_1(0,\bar{\omega}_1)}{\partial \bar{x}}\right]_{\bar{x}=0} = 0, \\
&\bar{G}_1(1,\bar{\omega}_1) = 1, \bar{G}_2(0,\bar{\omega}_2) = \frac{L_1}{L_2}\bar{G}_1(1,\bar{\omega}_1) \\
&\left[\frac{\partial \bar{G}_1(\bar{x}_1,\bar{\omega}_1)(\bar{x},\bar{\omega}_1)}{\partial \bar{x}_1}\right]_{\bar{x}_1=0} = \left[\frac{\partial \bar{G}_2(\bar{x}_2,\bar{\omega}_2)(\bar{x}_2,\bar{\omega}_2)}{\partial \bar{x}_2}\right]_{\bar{x}_2=0} \\
&\left[\frac{\partial^2 \bar{G}_1(\bar{x}_1,\bar{\omega}_1)(\bar{x},\bar{\omega}_1)}{\partial \bar{x}_1^2}\right]_{\bar{x}_1=0} = \frac{L_1}{L_2}\left[\frac{\partial^2 \bar{G}_2(\bar{x}_2,\bar{\omega}_2)(\bar{x}_2,\bar{\omega}_2)}{\partial^2 \bar{x}_2}\right]_{\bar{x}_2=0} \\
&\left[\frac{\partial \bar{G}_2(\bar{x}_2,\bar{\omega}_2)}{\partial \bar{x}_2}\right]_{\bar{x}_2=1} = 0 \\
&\left[\frac{\partial^3 \bar{G}_2(\bar{x}_2,\bar{\omega_2})}{\partial \bar{x}_2^3}\frac{L_3^2}{L_2^2}\right]_{\bar{x}_2=1} = \left[\frac{\partial^3 \bar{G}_3(\bar{x}_3,\bar{\omega_3})}{\partial \bar{x}_3^3} - \beta_3^4 \bar{M}_{mid}\bar{G}_3(\bar{x}_3,\bar{\omega}_3)\right]_{\bar{x}_3=0} \\
&\bar{G}_2(0,\bar{\omega}_2) = \bar{G}_3(0,\bar{\omega}_3)\frac{L_3}{L_2}, \left[\frac{\partial \bar{G}_3(0,\bar{\omega}_3)}{\partial \bar{x}_3}\right]_{\bar{x}_3=0} = 0 \\
&\bar{G}_3(1,\bar{\omega}_3) = \frac{L_4}{L_3}, \bar{G}_4(0,\bar{\omega}_4) = 1 \\
&\left[\frac{\partial \bar{G}_3(\bar{x}_3,\bar{\omega}_3)(\bar{x},\bar{\omega}_3)}{\partial \bar{x}_3}\right]_{\bar{x}_3=0} = \left[\frac{\partial \bar{G}_4(\bar{x}_4,\bar{\omega}_4)(\bar{x}_4,\bar{\omega}_4)}{\partial \bar{x}_4}\right]_{\bar{x}_4=0} \\
&\left[\frac{\partial^2 \bar{G}_3(\bar{x}_3,\bar{\omega}_3)(\bar{x},\bar{\omega}_3)}{\partial \bar{x}_3^2}\right]_{\bar{x}_3=0} = \frac{L_3}{L_4}\left[\frac{\partial^2 \bar{G}_4(\bar{x}_4,\bar{\omega}_4)(\bar{x}_4,\bar{\omega}_4)}{\partial^2 \bar{x}_4}\right]_{\bar{x}_4=0} \\
&\left[\frac{\partial \bar{G}_4(\bar{x}_4,\bar{\omega}_4)}{\partial \bar{x}_4}\right]_{\bar{x}_4=1} = 0, \bar{G}_4(1,\bar{\omega}_4) = 1
\end{aligned} \tag{2.14}
$$

where $\bar{M} = M/\rho A L_2$, the displacement transfer functions in the form of equation (2.11) can then be solved using (2.14). The total dynamic and static stiffness are then written as,

$$\bar{K_{dyntot}} =| \bar{G}_1'''(0, \bar{\omega}_1) + \bar{G}_4'''(1, \bar{\omega}_4) | \tag{2.15}$$

$$\bar{K_{statictot}} = [\lim_{\omega_1 \to 0} \bar{G}_1'''(0, \bar{\omega}_1)] + [\lim_{\omega_4 \to 0} \bar{G}_4'''(1, \bar{\omega}_4)] \tag{2.16}$$

Figure 2.4 shows the frequency response of the dynamic stiffness for the Mid mass Beam configuration in Figure 2.3 and the sliding beam mass configuration in Figure 2.2. The loss modulus is considered to be $\tan\delta = 0.01$. The mid-mass beam is twice the length of the sliding beam, and the middle mass is twice the tip mass such that $L_1 = L_4$, $L_2 = L_3$ and $M_{mid} = 2M$. The two beams are assumed to have the same uniform cross section and made from the same material. The results show that the frequency responses are proportional. The natural and isolation frequency are the same, the dynamic stiffness of the mid-mass beam is twice that of the sliding beam. Therefore, the frequency response of the sliding beam can be scaled to predict the frequency response of all the beams connected to a single mass. The stiffness of the isolator can be increased by simply adding another beam and scaling the mass proportionally to keep the same natural and isolation frequencies.

2.1.2 Beams Connected to an Independent Masses

Combining cantilever beams each with an independent tip mass brings forth several features to the beam network isolation such as isolation frequency clustering, and dynamic stiffness scaling (See Figure 2.5). These features can be achieved by tuning the mass of each beam, changing the input location on the beam, or changing the beam geometry. The dynamic stiffness of a cantilever beam with a tip mass subject to a point displacement input, as shown in Figure 2.6, can be calculated using the same method as the one for a sliding beam, the only difference is that the end boundary condition changes since the

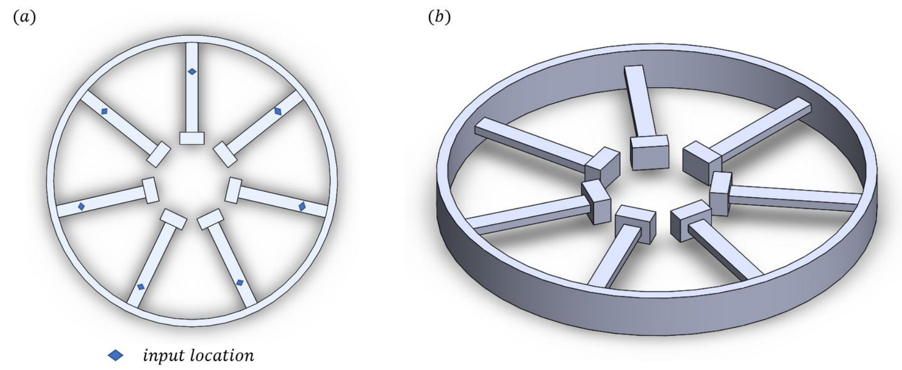

Figure 2.5. Diagram of a Beam network isolator with all the beams connected to independent masses and rooted to the same support and subject to the same input (a) is a top view (b) is an isometric view.

zero slope condition is no longer enforced and the mass is free to rotate at an angle, thus the effect of the rotational inertia of the mass is also accounted for. The non-dimensional boundary conditions are then:

$$
\begin{aligned}
&\bar{G}_1(0, j\bar{\omega}_1) = 0, \left[\frac{\partial \bar{G}_1(0, \bar{\omega}_1)}{\partial \bar{x}}\right]_{\bar{x}=0} = 0, \\
&\bar{G}_1(1, j\bar{\omega}_1) = 1, \bar{G}_2(0, j\bar{\omega}_2) = \frac{L_1}{L_2}\bar{G}_1(1, j\bar{\omega}_1), \\
&\left[\frac{\partial \bar{G}_1(\bar{x}_1, j\bar{\omega}_1)(\bar{x}, \bar{\omega}_1)}{\partial \bar{x}_1}\right]_{\bar{x}_1=0} = \left[\frac{\partial \bar{G}_2(\bar{x}_2, j\bar{\omega}_2)(\bar{x}_2, \bar{\omega}_2)}{\partial \bar{x}_2}\right]_{\bar{x}_2=0}, \\
&\left[\frac{\partial^2 \bar{G}_1(\bar{x}_1, j\bar{\omega}_1)(\bar{x}, \bar{\omega}_1)}{\partial \bar{x}_1^2}\right]_{\bar{x}_1=0} = \frac{L_1}{L_2}\left[\frac{\partial^2 \bar{G}_2(\bar{x}_2, j\bar{\omega}_2)(\bar{x}_2, \bar{\omega}_2)}{\partial^2 \bar{x}_2}\right]_{\bar{x}_2=0}, \\
&\left[\frac{\partial^2 \bar{G}_2(\bar{x}_2, j\bar{\omega}_2)}{\partial \bar{x}_2^2} - \beta_2^2 \bar{J}\frac{\partial \bar{G}_2(\bar{x}_2, j\bar{\omega}_2)}{\partial \bar{x}_2}\right]_{\bar{x}_2=1} = 0, \\
&\left[\frac{\partial^3 \bar{G}_2(\bar{x}_2, \bar{\omega_2})}{\partial \bar{x}_2^3} + \beta_2^4 \bar{M}\bar{G}_2(\bar{x}_2, \bar{\omega}_2)\right]_{\bar{x}_2=1} = 0,
\end{aligned}
\tag{2.17}
$$

Consider the case of two cantilever beams each with an independent tip mass connected to the same support, as shown in Figure 2.7. The dynamic and static stiffness are calculated using equations (2.12) (2.13) (2.15) and (2.16). Figure 2.8 shows the dynamic stiffness variation of a beam network consisting of two uniform cantilever beams of the

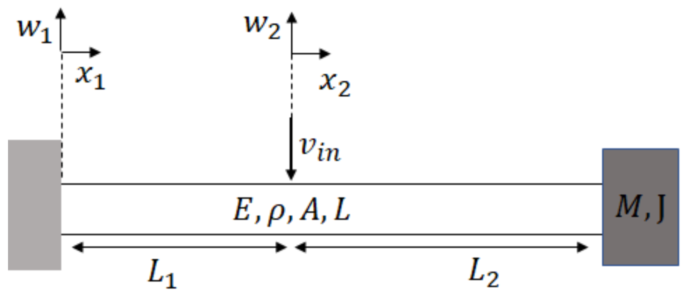

Figure 2.6. Cantilever beam with free tip mass under a displacement input v_{in}

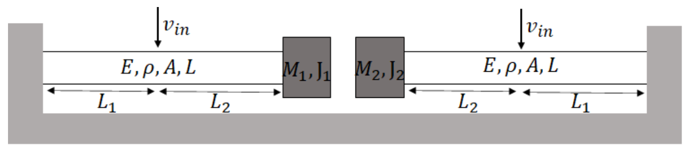

Figure 2.7. Two cantilever beams with free tip mass under a displacement input v_{in} connected to the same support

same length, cross sectional area, and beam material, and input position L_1. The loss modulus considered here is $\tan delta = 0.02$. The isolation frequency for beam 1 with $\bar{M} = 1$ is greater than that of beam 2 with $\bar{M} = 10$, this is expected since the heavier the mass the more anti-resonance force is produced. Both beams have a a single isolation frequency near their first mode in the vicinity of $\beta_1 < 1$, however, the total system consisting of both beams has 2 isolation frequencies near the $\beta_1 < 1$ vicinity. This shows that having multiple beams with independent masses can allow for a close cluster of isolation frequencies. The tip mass, input location and beam parameters can be tuned to cluster isolation frequencies on a certain frequency range. Furthermore, the dynamic stiffness reduction ratio can be scaled by tuning the mass and number of beams in the isolator. The building element of a beam network isolator is a beam; this section mainly deals with methods to tune the isolation performance of the beam. Figure 2.12 shows the isolation frequency variation as a function of both $\bar{M}$ and $r = L_1/L$. The surface plot shows that the isolation frequency of the beam tends to decrease as the tip mass increases. The frequency decreases more sharply with a change in the amplification ratio

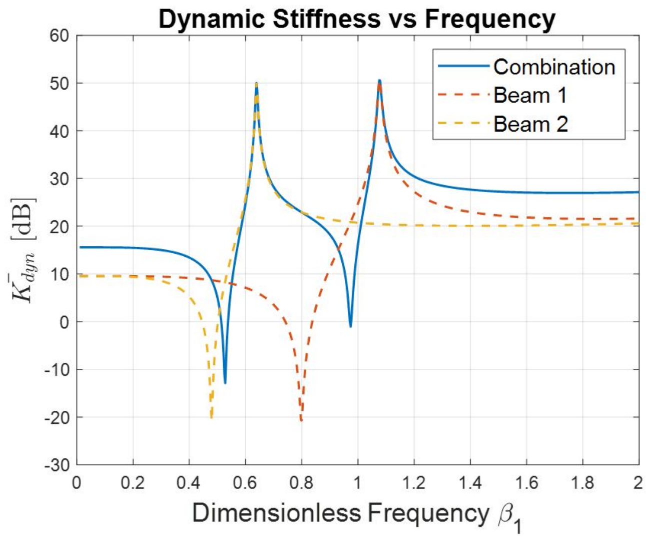

Figure 2.8. Dimensionless dynamic stiffness vs dimensionless frequency for beam 1 and beam 2 and their sum which is equivalent to the total dynamic stiffness, with $\bar{M} = 1$ and $\bar{M} = 10$, for beam 1 and 2 respectively, both with $\bar{J} = 0$ for the case of a point mass.

(which is equivalent to L_1/L).

2.2 Experimental Proof of Concept

The addition of a tip mass to a cantilever beam is expected to greatly reduce the shear force reaction isolation frequency at the root of a cantilever beam. An experimental proof of concept was constructed with an aluminum uniform beam cantilevered at one end, and a tip mass on its other end. The beam was excited by a 'LING LMT-100' shaker at a distance a from the cantilever root. The input force and the shear reaction force are both measured by two load cells, 'PCB-208C01' and 'PCB-208C02', respectively. The two load cell voltage signals are then processed through a 'PCB 482C-series' signal conditioner before they are collected through an NI-DAQ at a sampling frequency of 2000Hz. The shaker is excited with a chirp signal with an input voltage of 0.1 volts, and a frequency sweep between 0 to 60 Hz for a sweep length of 60 seconds. The material and geometric properties of the beam and mass are shown in tables 2.1 and 2.2.

Table 2.1. Material, geometric and damping properties of beam

Property	Value
E	73 Gpa
ρ	2688 Kg/m^3
L	0.175 m
A	6.972×10^{-4} m^2
I	4.555×10^{-11} m^4

Table 2.2. Tip mass and rotational inertia

Property	Value
M	0.07 Kg
J	2.0181×10^{-5}Kg m^2

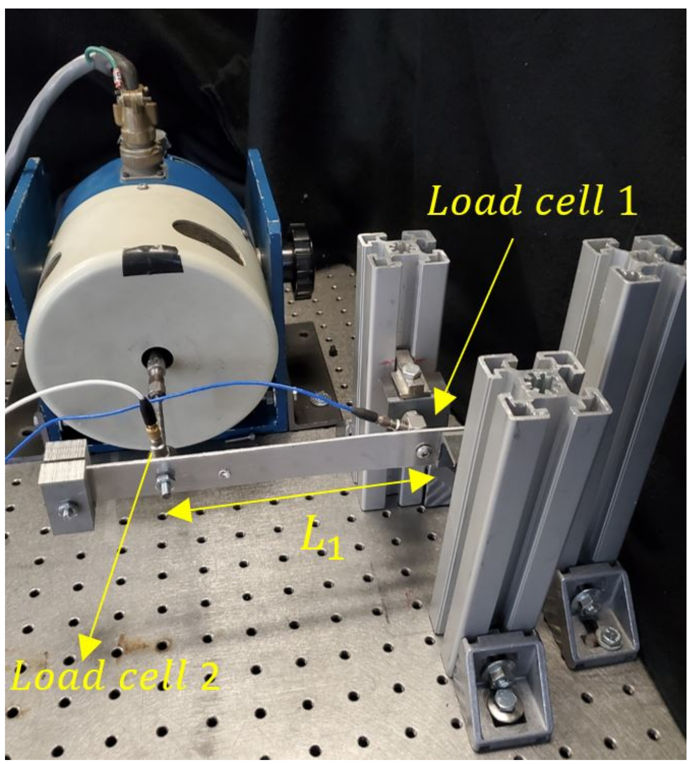

Figure 2.9. Experimental setup showing the beam mass, load cells and shaker stinger.

The time domain voltage signals collected by the DAQ were then transferred to the frequency domain using a FAST FOURIER TRANSFORM (FFT) algorithm. The experiment was done at two distances from the cantilever root, one at $a = 11cm$ and another at $a = 14cm$. The experimental setup is shown in Figure 2.9 . To compare with the analytical method presented in the first section of this paper, the analytical model is altered to incorporate a force input rather than a displacement input. The Euler Bernoulli equation becomes,

$$\frac{\partial^4 \bar{w}}{\partial \bar{x}^4} + \frac{\partial^2 \bar{w}}{\partial \bar{t}^2} = \bar{f_{in}} \delta(\bar{x} - \bar{a}), \tag{2.18}$$

where $\bar{f_{in}} = f_{in} L^3/EI$ and $\bar{a} = a/L$. Letting $\bar{W}(\bar{x}, s)$ be the Laplace transform of $\bar{w}(x, t)$, and $\bar{F}_{in}(s)$ be the Laplace transform of the forcing function $f_{in}(t)$. Therefore the transfer function is defined as,

$$\bar{G}(\bar{x}, \bar{s}) = \frac{\bar{W}(\bar{x}, \bar{s})}{\bar{F}_{in}(\bar{s})}, \tag{2.19}$$

Taking the Laplace transform of equation (2.18) and replacing by (2.19) and $\bar{s} = j\bar{\omega}$,

$$\frac{\partial^4 \bar{G}}{\partial \bar{x}^4} + \beta^4 \bar{G} = \delta(\bar{x} - \bar{a}), \tag{2.20}$$

where $\bar{\omega}$ is the nondimensional frequency such that $\bar{\omega} = \omega L^2/c$ and $\beta^4 = \bar{\omega}^2$. The solution of equation (2.20) is,

$$\begin{aligned} \bar{G}(x, j\omega) = -&\left[\frac{\sinh \beta(\bar{x} - \bar{a}) - \sin \beta(\bar{x} - \bar{a})}{2\beta^3}\right] \\ &+ \bar{G}(0, j\omega)\left[\frac{\cosh \beta\bar{x} + \cos \beta\bar{x}}{2\beta^2}\right] \\ &+ \bar{G}'(0, j\omega)\left[\frac{\sinh \beta\bar{x} + \sin \beta\bar{x}}{2\beta^3}\right] \\ &+ \bar{G}''(0, j\omega)\left[\frac{\cosh \beta\bar{x} - \cos \beta\bar{x}}{2\beta^2}\right] \end{aligned}$$

$$+ \bar{G}'''(0, j\omega)\left[\frac{\sinh\beta\bar{x} - \sin\beta\bar{x}}{2\beta^3}\right]. \tag{2.21}$$

The non-dimensional boundary conditions are written as,

$$\begin{aligned}
\bar{G}(0,\bar{\omega}) = 0, \left[\frac{\partial\bar{G}(0,\bar{\omega})}{\partial\bar{x}}\right]_{\bar{x}=0} &= 0, \\
\left[\frac{\partial^2\bar{G}(\bar{x},\bar{\omega})}{\partial\bar{x}^2} - \beta^2\bar{J}\frac{\partial\bar{G}(\bar{x},\bar{\omega})}{\partial\bar{x}}\right]_{\bar{x}=1} &= 0, \\
\left[\frac{\partial^3\bar{G}(\bar{x},\bar{\omega})}{\partial\bar{x}^3} + \beta^4\bar{M}\bar{G}(\bar{x},\bar{\omega})\right]_{\bar{x}=1} &= 0,
\end{aligned} \tag{2.22}$$

with $\bar{M} = M/\rho A$ and $\bar{J} = J/\rho AL^2$.The solution $G(\bar{x},\bar{\omega})$ can be obtained by substituting (2.21) in the non-dimensional boundary conditions (2.22). The nondimensional force reaction transfer function at the root is written as:

$$\frac{\bar{F}(\bar{\omega})}{\bar{F}_{in}} = \bar{G}'''(0,\bar{\omega}) \tag{2.23}$$

The following dimensional transformations are used, for shear force F_{out},

$$F_{out} = \frac{EI}{L^2}\bar{G}'''(0,\bar{\omega}), \tag{2.24}$$

and the excitation frequency ω,

$$\omega = \beta^2\sqrt{\frac{EI}{\rho AL^2}} \tag{2.25}$$

The experimental results in Figures 2.10 and 2.11 show that the analytical model accurately predicts the frequency response of the cantilever beam. The analytical loss modulus is adjusted to $\tan\delta = 0.2$ for the analytical model. There seems to be a 15% and a 2% offset in the natural and isolation frequencies at $L_1 = 14cm$. At $L_1 = 11cm$ the offset is 10% for both frequencies. This is probably because the stinger rigidly attaches

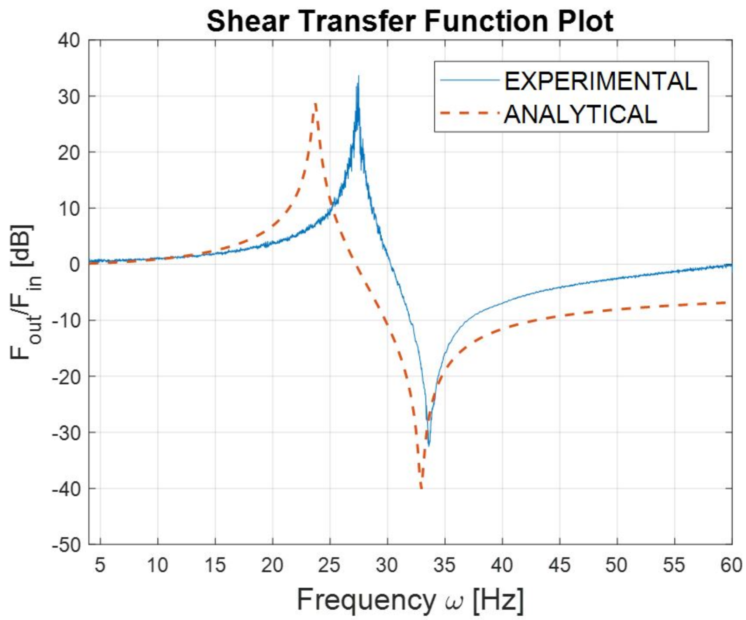

Figure 2.10. Transfer function amplitude versus frequency ω for shear force at $x = 0$ and with an input force at $L_1 = 11$ cm.

to the beam at the connection point (at L_1) and analytical model does not account for the added rotational stiffness. The added stiffness generally results in a right shift in the frequency response. The results show that there is a drop of force transmissibility at 45 Hz at $a = 14$ cm, and 32.7 Hz at $a = 11$ cm. The isolation frequency is reduced by 92% and 78% after the addition of a tip mass with $\bar{M} = 2.3$ for $L_1/L = 0.8$ and $L_1/L = 0.63$ cm, respectively. Therefore, the isolation frequency decreases as the distance between the input and the root decreases. This is mainly because the mass will have more mobility to oscillate, thus creating a larger anti-resonance force. The dynamic stiffness at the isolation frequencies reduces to zero due to the absence of damping. These results show that the beam analytical model can accurately predict the response of a single beam. This proof of concept shows that the beam with tip mass is a suitable High-Static-Stiffness-Low-Dynamic-Stiffness isolator. Experiments with multiple parallel stacked beams will be explored in the chapters 3 and 4.

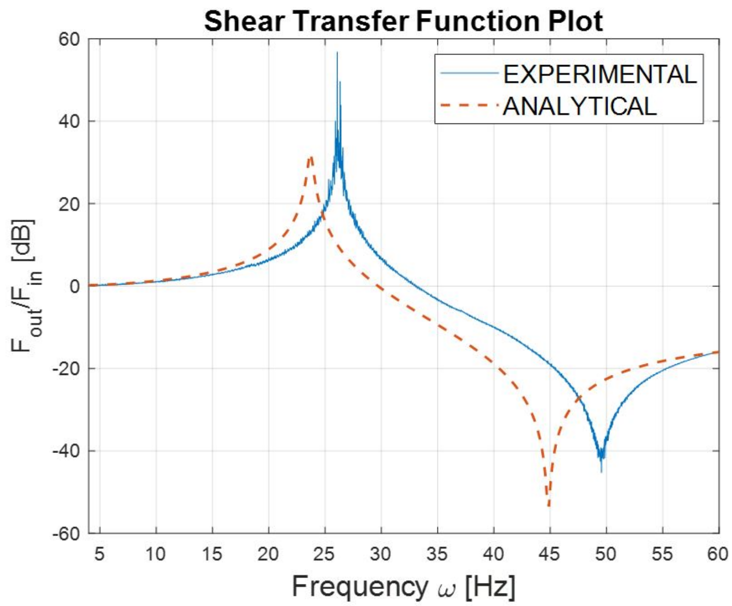

Figure 2.11. Transfer function amplitude versus frequency ω for shear force at x=0 and with an input force at $L_1 = 14$ cm.

2.3 Discussion on Parallel Stacking

Using beams connected to a single mass is a good way to achieve a high stiffness isolator. The synchronous movement of the mass and the beams allows for a smooth dynamically coupled response. Using only a group of beams connected to the same mass, clustering frequencies can be achieved by tuning the beam and mass parameters to achieve a multi-mode isolation in the required frequency range. However, this is often difficult to achieve given certain size and weight constraints for multi-frequency isolation applications. A high stiffness isolator with a close cluster of force isolation frequencies can be achieved using hybrid beam isolators, consisting of the two sub-components introduced above, or using only beams connected to independent masses, and tuning the masses, beams, or excitation positions, accordingly.

Generally, the stiffer the beam, the less oscillating force it can produce, and a larger tip mass is needed to achieve a target isolation frequency as compared to a beam with

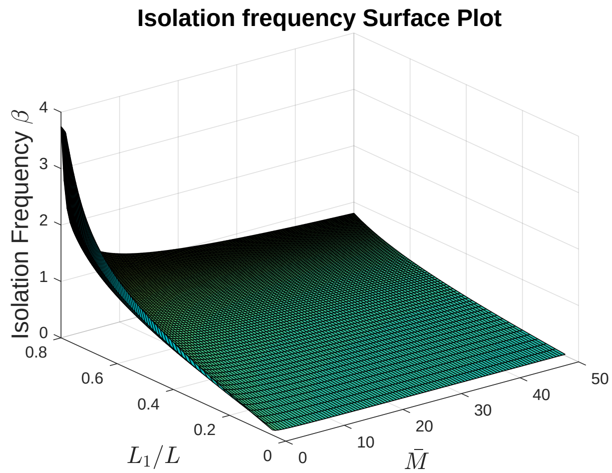

Figure 2.12. Surface plot of the variation of isolation frequency β as a function of $\bar{M}$ and L_1/L for the case of cantilever beam with a tip mass.

less stiffness. Soft beams are not suitable for high stiffness isolator applications, mainly because beams need to have large oscillations to induce large antiresonant forces, therefore stiffer beams induce a large mass penalty to compensate for smaller displacements. Thus, for a single beam there is always a trade-off between high stiffness and high isolation characteristics. Furthermore, a high stiffness and high deflection characteristic is difficult to achieve for a single beam, even if the isolation goals could be achieved. This is mainly due to the high stresses caused by the large deflection. However, this design problem can be solved by using beam network isolators, rather than a single beam. Beams with little to no tip mass can be used to contribute most of the stiffness. This comes in handy since the target high stiffness can be achieved by using multiple fewer stiff beams in parallel, acting as springs in parallel. This will come at a low weight penalty since these beams are not coupled with a tip mass. Flexible beams could be used to create all the anti-resonance needed and can be tuned to provide the needed dynamic stiffness reduction ratio. For the case of a beam network the problem of large weight penalty can be mitigated for applications where the dynamic stiffness at the operating frequency is not necessarily very low, in this case the total mass will be dependent on the ratio of dynamic stiffness reduction. This is done by using beams not connected to the same mass where the overall sum of dynamic stiffness for each beam can optimized to reach the dynamic stiffness goal. Figure 2.12 shows the isolation frequency variation as a function of both $\bar{M}$ and $r = L_1/L$. The surface plot shows that the isolation frequency of the beam tends to decrease as the tip mass increases. The frequency decreases more sharply with a change in the amplification ratio L_1/L. This means that for even a small tip mass the anti-resonance forces can be much larger for smaller amplification ratios. Thus, decreasing the amplification ratio on the beam level is another method that can be used to mitigate the problem of large weight penalties. However, the level of mitigation is highly dependent on the input deflection limit as well as the deflection of the beam. As the amplification ratio is increased, the stresses in the beam will increase due to an increase in bending moments.

Chapter 3

Dynamic Antiresonant Vibration Isolators with Flexible Levers

This chapter builds on the concept of parallel stacking and introduces a DAVI with a flexible lever and elastic boundary conditions. The proposed isolator is modeled as a mass loaded beam with elastic boundary conditions on both ends, and an elastic mid span connection, as shown in Figure 3.1. The proposed model is expected to capture the complex dynamics of the lever, which will result in more accurate DAVI dynamic modelling, as well as a larger design space because the beam and springs parameters affect the dynamic response. Moreover, the added flexibility and inertial profile of the lever will lead to higher antiresonance forces as compared to rigid lever classical DAVIs. A transfer function model is introduced to predict the dynamic stiffness and the force transmissibility of flexible DAVIs. An experiment is conducted with a 3D printed flexible DAVI to validate the analytical model and validate performance. The monolithic features in the proposed isolator are realizable through additive manufacturing, thus eliminating friction losses at critical connection points.

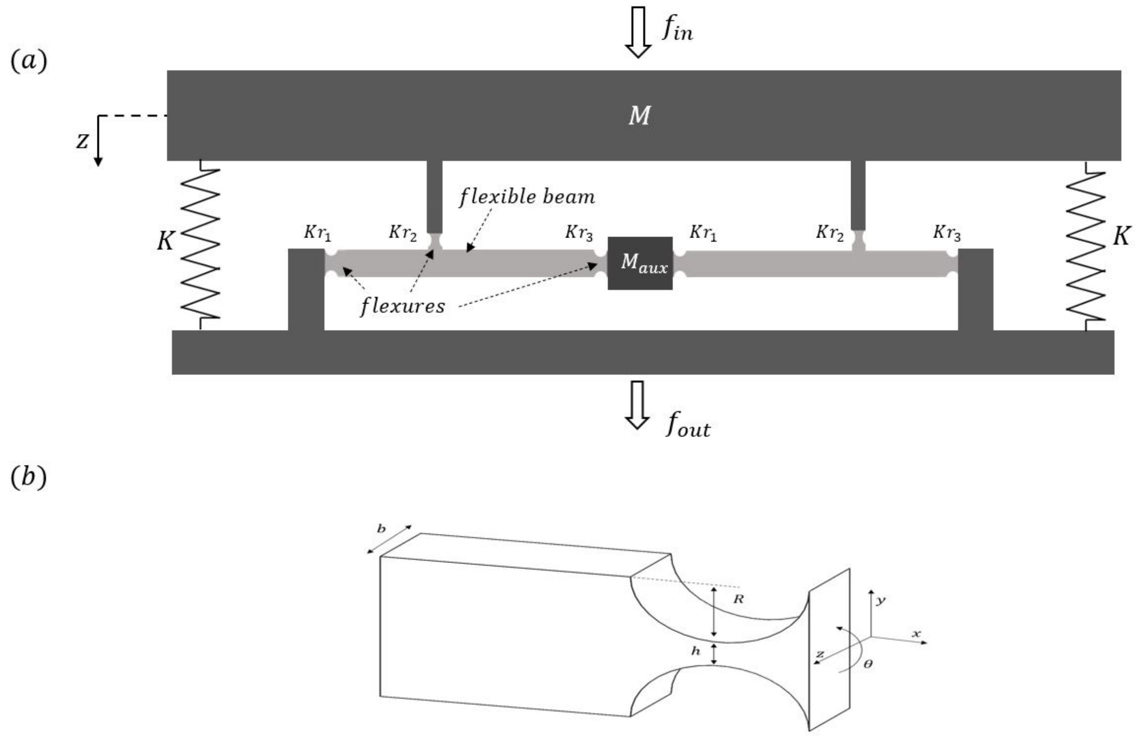

Figure 3.1. (a) Schematic showing the proposed generic DAVI with a flexible beam and elastic boundary conditions. (b) Drawing showing a circular flexure hinge

3.1 Analytical Model

Figure 3.1 shows the proposed flexible DAVI model. The vibrating structure is subject to a force input f_{in}. A linear spring with stiffness K acts as a direct stiffness element between the vibrating object and the fixed support.

Symmetry is assumed and only the half-model is analyzed as shown in Figure 3.2. The lever is elastic with a Young's modulus E, density ρ, cross-sectional Area A, and moment of inertia I. The mass is connected to the beam via a rotational spring, that models a flexure. The beam is supported by a rotational spring with a stiffness Kr_1, The beam is connected to the input structure via a rotational spring Kr_2 and to the auxiliary mass via a rotational spring Kr_3. The beam of length L is connected to the vibratory structure at a distance L_1. The transverse displacement of the beam is w_i where the

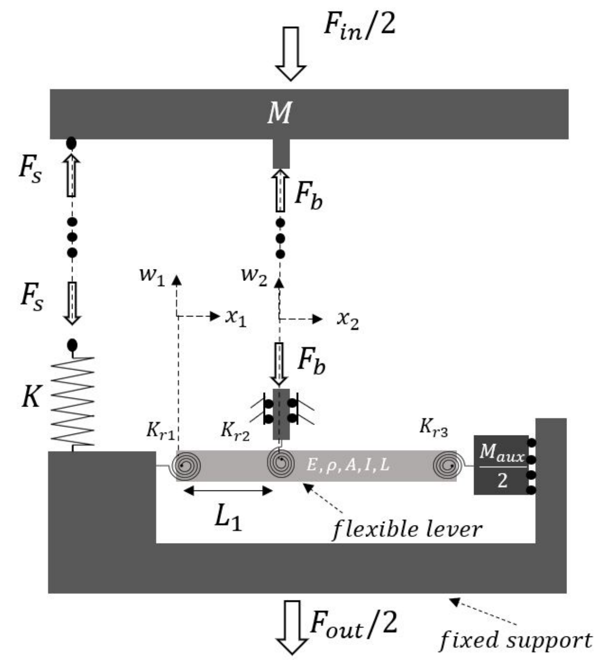

Figure 3.2. Schematic showing the proposed flexible beam lever with elastic boundary conditions.

subscript i denotes the first and second part of the beam. The force transferred from the beam to the ground is f_g. The Euler Bernoulli equation is:

$$E^* I \frac{\partial^4 w_i}{\partial x_i^4} + \rho A \frac{\partial^2 w_i}{\partial t^2}, = 0 \tag{3.1}$$

where $w_i(x,t)$ is the transverse displacement, the subscript i denotes the part of the beam such that $i = 1$ for the part of the beam between Kr_1 and Kr_2, and $i = 2$ between Kr_2 and Kr_3. E^* is the complex Young's modulus,

$$E_i^* = E(1 + j_{im} tan\delta), \tag{3.2}$$

where $\tan delta$ is the loss tangent such that,

$$tan(\delta) = \frac{E''}{E}. \tag{3.3}$$

E is the Young's modulus (storage modulus) and E'' is the loss modulus, $j_{im} = \sqrt{-1}$. The complex Poisson's ratio v^* is assumed to be equal to the real Poisson's ratio v, based on [98]. The Laplace transform of equation (3.1) becomes,

$$E^* I \frac{\partial^4 W_i}{\partial x^4} + \rho A s^2 W_i = 0, \tag{3.4}$$

where $W(x, s)$ is the Laplace transform of $w(x, t)$, $F_b(s)$ and $F_g(s)$ are the Laplace transforms of the forcing function f_b and reaction force f_g. The transfer function,

$$G_i(x, s) = \frac{W_i(x, s)}{F_b(s)} \tag{3.5}$$

Thus, dividing equation (3.4) by $F_b(s)$, and using equation (3.5), the ordinary differential (ODE) equation for the transfer function $G(x, s)$ is obtained. Substituting the Laplace variable s with $s = j\omega$ with $j = \sqrt{-1}$ and ω is the excitation frequency, the frequency domain ODE is obtained:

$$\frac{\partial^4 G_i(x_i, \omega)}{\partial x^4} - \beta^4 G_i(x_i, \omega) = 0 \tag{3.6}$$

where,

$$\beta^4 = \frac{\rho A \omega^2}{E^* I}. \tag{3.7}$$

The solution to equation (3.6),

$$G_i(x,\omega) = G_i(0,\omega)\left[\frac{\cosh\beta x + \cos\beta x}{2\beta^2}\right] + G_i'(0,\omega)\left[\frac{\sinh\beta x + \sin\beta x}{2\beta^3}\right] + G_i''(0,\omega)\left[\frac{\cosh\beta x - \cos\beta x}{2\beta^2}\right] + G_i'''(0,\omega)\left[\frac{\sinh\beta x - \sin\beta x}{2\beta^3}\right]. \tag{3.8}$$

The coefficients $G_i(0,\omega)$, $G_i'(0,\omega)$, $G_i''(0,\omega)$, $G_i'''(0,\omega)$ can be found by replacing equation (3.8) in the boundary conditions (BCs). The boundary conditions at x_1=0 are as follows,

$$\begin{aligned} \left[E^*I\frac{\partial^3 G_1(x_1,\omega)}{\partial x_1^3} + K_b G_1(x_1,\omega)\right]_{x_1=0} &= 0, \\ \left[Kr_1\frac{\partial G_1(x_1,j\omega)}{\partial x} - E^*I\frac{\partial^2 G_1(x_1,j\omega)}{\partial x_1^2} -\right]_{x_1=0} &= 0. \end{aligned} \tag{3.9}$$

The boundary conditions at $x_2 = L_2$,

$$\begin{aligned} \left[Kr_2\frac{\partial G_2(x_2,j\omega)}{\partial x_2} + E^*I\frac{\partial^2 G_2(x_2,\omega)}{\partial x_2^2} -\right]_{x_2=L_2} &= 0, \\ \left[E^*I\frac{\partial^3 G_2(x_2,\omega)}{\partial x_2^3} + M\omega^2 G_2(x_2,\omega)\right]_{x_2=L_2} &= 0. \end{aligned} \tag{3.10}$$

The continuity conditions at $x_1 = L_1$ (and $x_2 = 0$) are as follows,

$$\begin{aligned} &[G_1(x_1,\omega]_{x_1=L_1} = [G_2(x_2,\omega]_{x_2=0}\,, \\ &\left[\frac{\partial G_1(x_1,\omega)}{\partial x_1}\right]_{x_1=L_1} = \left[\frac{\partial G_2(x_2,\omega)}{\partial x_2}\right]_{x_2=0}, \\ &\left[\frac{\partial^2 G_1(x_1,\omega)}{\partial x_1^2} + Kr_2\frac{\partial G_1(x_1,\omega)}{\partial x_1}\right]_{x_1=L_1} = \left[\frac{\partial^2 G_2(x_2,\omega)}{\partial x_2^2}\right]_{x_2=0}, \\ &\left[E^*I\frac{\partial^3 G_1(x_1,\omega)}{\partial x_1^3} + 1\right]_{x_1=L_1} = \left[E^*I\frac{\partial^3 G_2(x_2,\omega)}{\partial x_2^3}\right]_{x_2=0}. \end{aligned} \tag{3.11}$$

The force transmissibility transfer function

$$T_{flex}(\omega) = \frac{-KG_2(0,\omega) + E^* I G_1'''(0,\omega)}{-KG_2(0,\omega) + 1 + \omega^2 M_t G_2(0,\omega)}, \tag{3.12}$$

where M_t is the mass of the top vibrating input structure.

3.2 Design and Experimental Setup

Figure 3.3 shows an example monolithic flexible DAVI design with beams forming the stiffness and lever elements. This device shown was designed for low amplitude vibrations. The distance between the mass and the input structure and support is suitable for low beam-mass displacements.

The stiffness beams are short with 1.5 cm lengths and 20×1 mm rectangular cross sections. Their stiffness can be approximated by the stiffness equation of a cantilever beam with a sliding tip end subject to a point force, such that $K = 12E_sI_s/L_s^3$, where the stiffness beam Young's modulus $E_s = 3$ Gpa, and the moment of inertia $I_s = 0.005$ Nm^2. The lever is connected to the device via compliant hinges shown in Figure 3.1. The flexures are compliant in the rotational direction with a stiffness,

(a)

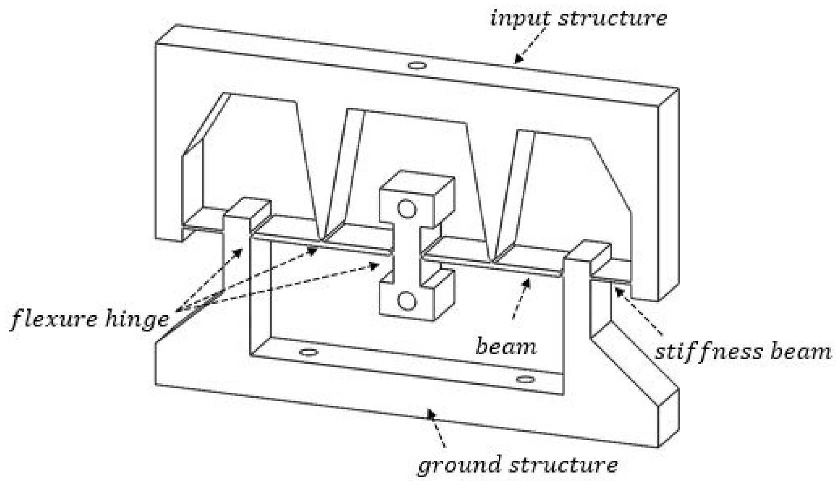

(b)

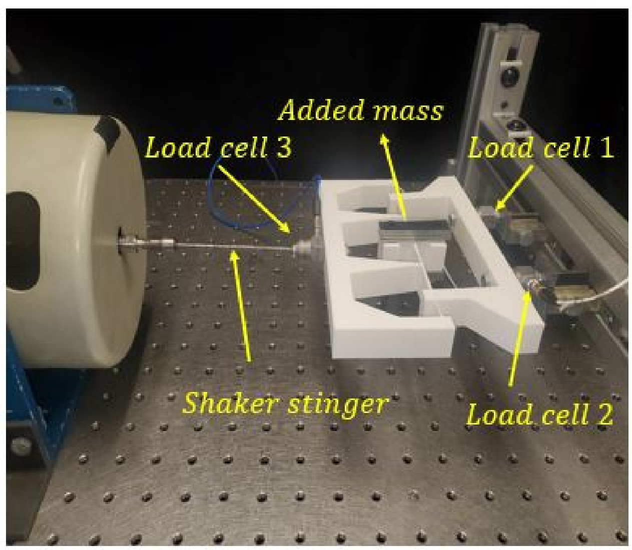

Figure 3.3. (a) Drawing showing a dimetric view of the proposed Flexible DAVI (flex-beam) (b) Photograph showing the experimental setup

$$Kr_i = \frac{Ebh^3(2R+h)(4R+h)^3}{24R}\Bigg[h(4R+h)(6R^2+4Rh+h^2) + 6R(2R+h)^2\sqrt{h(4R+h)}\arctan\left(\sqrt{1+\frac{4R}{h}}\right)\Bigg]^{-1} \quad (3.13)$$

and infinite translational stiffness [99]. Figure 3.3-(a) shows the fabricated flexible-beam DAVI (Flex-beam) composed of an input structure connected to the stiffness beams and

Table 3.1. Area and Flexural Rigity of the Flex-Beam and the Stiff-Beam DAVIs

DAVI type	Cross-sectional Area A	Flexural Rigidity EI
Flex-beam	4×10^{-5}m^2	0.04 Nm^2
Stiff-beam	1.4×10^{-4}m^2	1.715 Nm^2

the lever-beams, which are, in terms, connected to the ground structure. The tips of the lever beams are connected to an I-shaped oscillating mass. The mass includes holes to attach external mass elements. This allows for dynamic response tunability by changing the external mass. For comparison, another flexible DAVI (Stiff-beam DAVI) with a much stiffer lever-beam, is shown in Figure 3.4-(a). The Young's modulus is assumed to be $E = 3$ Gpa [100], the density is measured to be 1100 Kg/m^3. The flexure hinges for both devices have $R = 0.7$ mm, $h = 0.6$ mm with a depth $b = 2$ cm, corresponding to a rotational stiffness $Kr_i = 1.58$ N rd/m for $i = 1, 2, 3$. Both beams have a total length of 5 cm with $L_1 = L_2 = 2.5$ cm. Both beams have a rectangular cross section with a depth of 2 cm, and a height of 2 mm for the flex beam, and 7 mm for the stiff beam. The cross-sectional area and flexural rigidities for both beams is shown in Table 3.1. The isolators were tuned to achieve an isolation frequency of 67 Hz. The mass used on the flex-beam DAVI is 0.0335 Kg, the mass used on the stiff-beam DAVI is 0.067 Kg (twice as large).

The two isolators are printed with an Ender 3 V2 3D printer at 100% infill density of Polyactic Acid (PLA) and at a raster angle of 45°, a layer thickness of 0.2 mm, a print speed of 50 mm/sec, a 200 ° C nozzle extrusion temperature and 50 ° C build plate temperature.

The experimental setup for vibration testing is shown in Figures 3.3-(b) and 3.4-(b). The isolators are connected to a shaker stinger via a PCB201-C load cell that measures the input force. The mount structure is connected to a support structure via two PCB208-C load cells that measure the output force. The voltage signals of the load cell

(a)

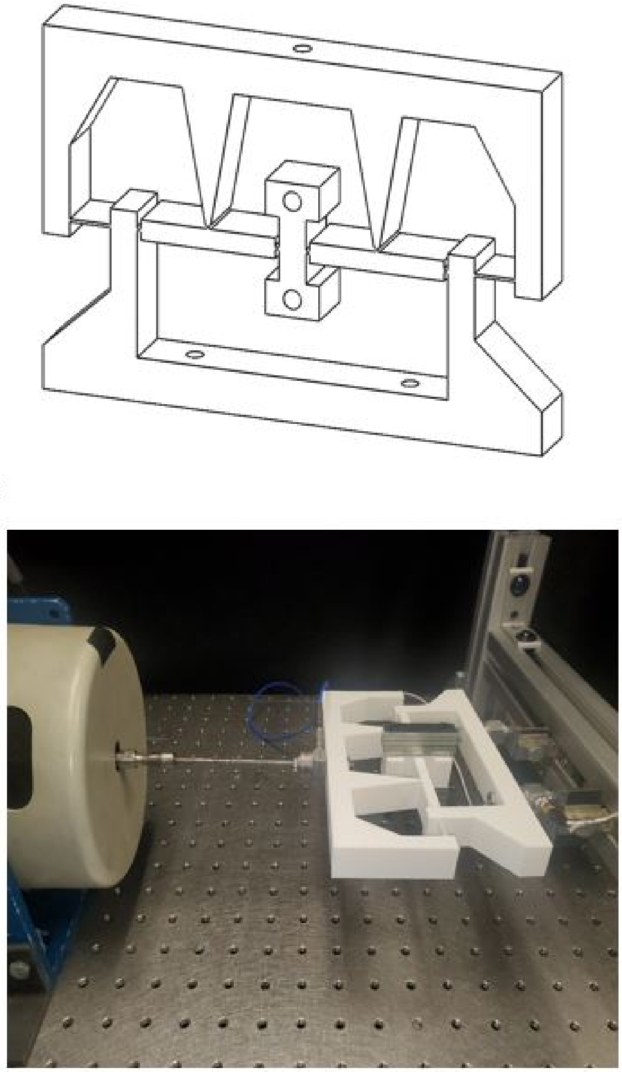

(b)

Figure 3.4 has two panels: (a) the drawing and (b) the photograph.

Figure 3.4. (a) Drawing showing a dimetric view of the proposed Flexible DAVI (stiff-beam) (b) Photograph showing the experimental setup

are transmitted to a PCB482C-series signal conditioner. The voltage signals are then collected by an NI data acquisition device. Note that there is no static preload condition in both experiments.

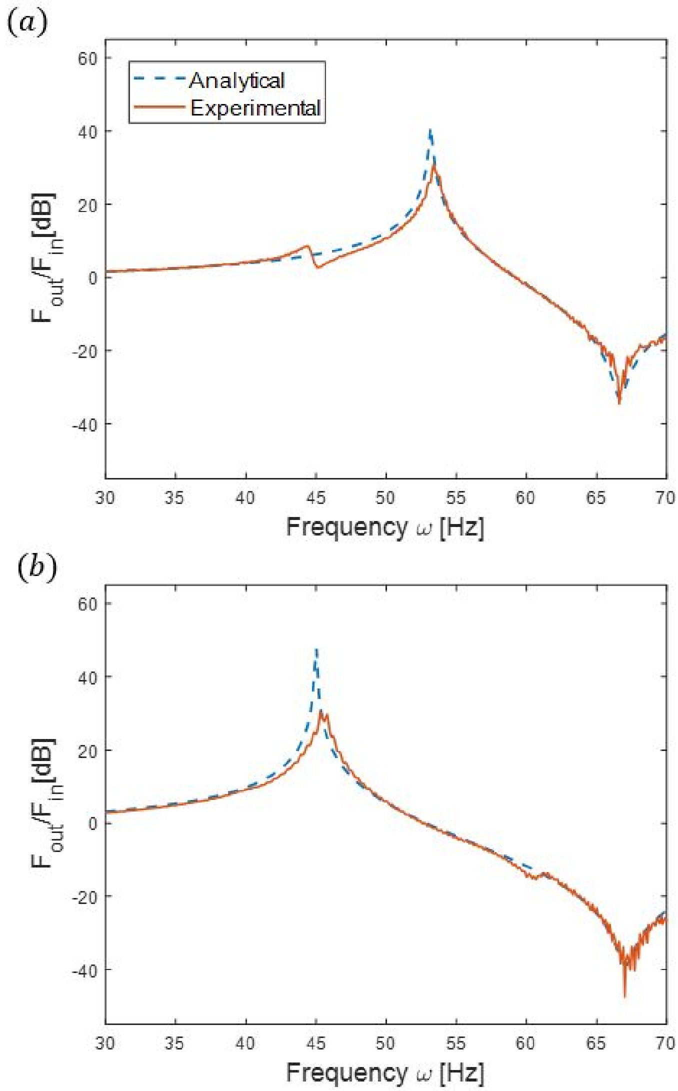

Figure 3.5. Analytical (dashed) vs experimental (solid) force transmissibility frequency response for a (a) flex-beam DAVI and a (b) stiff-beam DAVI.

3.3 Results and Discussion

Figures 3.5- (a) and (b) show the force transmissibility of the analytical model and the experiment for the flex beam and the stiff beam, respectively. The loss modulus is adjusted to $\tan\delta = 0.02$ for the analytical models. Both devices show an isolation frequency at 67 Hz, as predicted by the model and a resonance at a lower frequency. The overall shapes of the frequency response curves match well between theory and experiment. For the flex-beam DAVI there is a 0.24 Hz left shift for natural frequency (0.45 % deviation) between the analytical prediction and the experiment. For the stiff-beam DAVI there is a 0.41 Hz left shift for natural frequency (1.34 %). Overall, the experiment is in agreement with the analytical model. The discrepancy between the model and the experiment is partially caused by 3D printing errors. Small thickness variations in the flexure hinges can alter the frequency response, especially when the errors cause stiffness asymmetries between the right- and left-hand side beams. Moreover, the input, output and support structures are not perfectly rigid, which causes some deviations from the experiment.

Figure 3.5 shows that the flexible beam DAVI achieves the same isolation frequency as that of the stiff-beam but with half the required mass. The flexibility of the lever helps achieve better isolation performance than a stiff beam that does not bend easily. The flexible beam allows for higher mass oscillations, which amplifies the antiresonance forces, leading to lower isolation frequencies. Although the stiff-beam is heavier with almost 3.5 times more mass than the flex-beam, the additional beam inertia does not contribute to antiresonance as much as the amplified oscillations of the attached mass. The stiff design does have a wide gap between the resonance and isolation frequencies, providing a wide frequency isolation region.

3.4 Comparison to Rigid Classic DAVI

The force transmissibility for rigid-lever DAVI, with friction-less hinge connections and a fixed ground support, is,

$$T_{rigid}(\omega) = \frac{K - \omega^2 \left[M_{aux} \frac{L}{L_1} (\frac{L}{L_1} - 1) \right]}{K - \omega^2 \left[M + M_{aux} (\frac{L}{L_1})^2 \right]}. \tag{3.14}$$

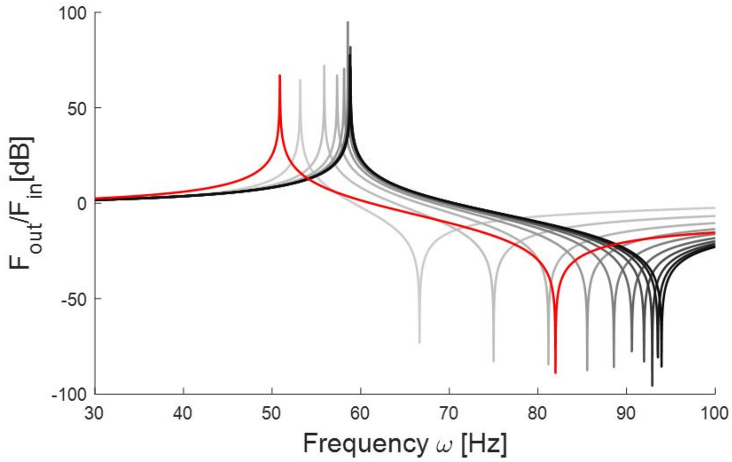

Figure 3.6. Force transmissibility response of a rigid lever Classic DAVI (red) and flexible-lever DAVI with flexural rigidities varying from $EI = 0.04$ Nm^2 (light gray) to $EI = 1.715$ Nm^2 (black) with the darker colors resembling a higher EI.

For comparison with a flexible lever DAVI, $L = 0.05$ m and $L_1 = 0.025$ m. The masses used are $M_{aux} = 0.0335$ Kg and $M = 0.04$ Kg. The external stiffness element spring stiffness is $K = 17778$ N/m. For the flexible beam comparison in Figure 3.6, the flexural rigidity of the beam is varied from $EI = 0.04$ to 1.715 Nm^2. There is no damping assumed in this case and the loss modulus is $\tan\delta = 0$. The comparison in Figure 3.6 shows that flexible DAVIs with a smaller flexural rigidity are capable of achieving lower isolation frequency compared to a rigid DAVI with the same auxiliary mass, up until $EI = 0.15$ Nm^2, after which the isolation frequencies of the flexible DAVI exceed that of the rigid DAVI. Note that the flexible DAVIs with very high flexural rigidities do not converge to the rigid DAVI response due to the added stiffness of the flexure hinges, and the beam's inertial properties, as opposed to a the classic DAVI, where the lever is assumed to be rigid and mass-less. Therefore, for more flexible levers, the oscillations of the mass amplify the inertial forces and achieve lower isolation frequencies with less mass penalties compared to rigid levers.

Chapter 4

Elastomeric Beam Network Isolator

4.1 Elastomer Beam Network Isolator Design

The beam network isolators presented above are limited by the compliance limits of the of the beams themselves, or the flexure hinges. The maximum displacement or force input is largely controlled by the beam/flexure fatigue stress limits; thus, a rubber-based isolator is proposed. Rubber is known to a have a relatively high shear strain modulus compared to other materials, thus, rubber can undergo large shear strain deformation before it permanently deforms. Therefore, torsional rubber hinges shown in Figure 4.1 are proposed to be used as an elastic connection to a beam with a tip mass. The inner and outer diameters of the rubber hinge are denoted by d_i and d_o, the width of the hinge is denoted by w_h. The torsional hinge design is similar to a bushing. The torsional strain, and stiffness, can be calculated using the following equations from [101, 102]:

$$\gamma_{tor} = \frac{2\theta}{d_i^2}\left(\frac{1}{d_i^2} - \frac{1}{d_o^2}\right)^{-1} \tag{4.1}$$

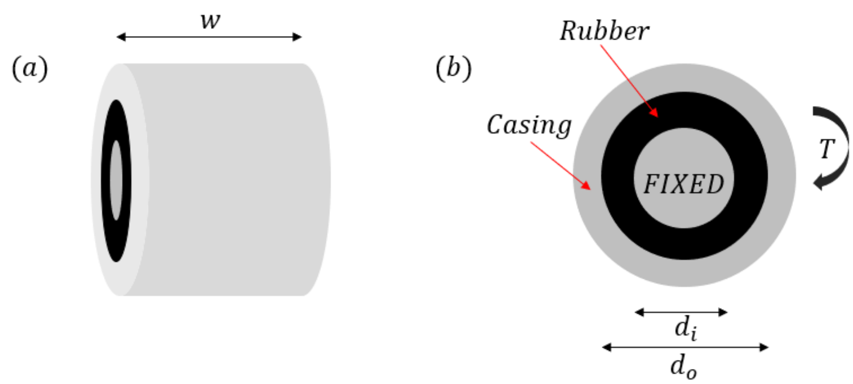

Figure 4.1. Schematic of a torsional hinge with (a) and (b) showing the lateral and cross-sectional view of the proposed hinge

$$K_r = \pi G_{mod} w_h \left(\frac{1}{d_i^2} - \frac{1}{d_o^2} \right)^{-1} \tag{4.2}$$

where θ is the relative angular displacement of the rubber between the outer circumference and the fixed inner circumference, G_{mod} is the shear modulus of the enclosed rubber material. The following maximum radial strain equation for a rubber bushing is used [103],

$$\epsilon_{rad} = \frac{2F_{rad}}{\pi w_h d_i (G_{mod} + E_a)} \tag{4.3}$$

where F_{rad} is the axisymmetric radial force on of the rubber bushing. E_a is the effective Young's Modulus,

$$E_a = \frac{4G_{mod}}{1 - \frac{S}{\sqrt{3}} \tanh \frac{\sqrt{3}}{S}} \tag{4.4}$$

and S is the shape factor for a circular hinge, defined as the ratio of loaded area, to force free bonded area, and calculated as,

$$S = \frac{2w_h(b^3 - a^3)}{3(b^2 - a^2)^2} \tag{4.5}$$

Table 4.1. Rubber hinge isolator specifications

Specification	Value
Static Stiffness	$7 \times 10^6 N/m$
Max Static Displacement	$3.81 \times 10^{-3} m$
Isolation frequency	$25 Hz$
Isolation ratio at 25 Hz	$0\% - 30\%$
Isolation ratio at 23 Hz	$0\% - 35\%$
Isolation ratio at 27 Hz	$0\% - 40\%$
Dynamic Displacement	$2.54 \times 10^{-7} m$

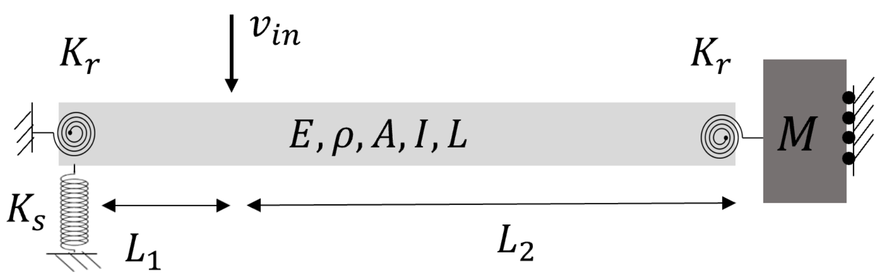

Figure 4.2. Schematic of a sliding beam with a tip mass and torsional hinges on both extremities

where, $a = d_i/2$, and $b = d_o/2$. The radial stiffness denoted by K_s is calculated with the following equation [103],

$$K_s = \frac{4\pi}{\frac{S^2+2.45}{S^2+1.45} \log \frac{b}{a} - \frac{b^2-a^2}{b^2+a^2}} \tag{4.6}$$

The radial equation used above and presented in [103] is more suitable for direct analytical calculations than other established methods to calculate the radial stiffness such as the ones in [101, 104], which rely on experimental data for rubber compression moduli.

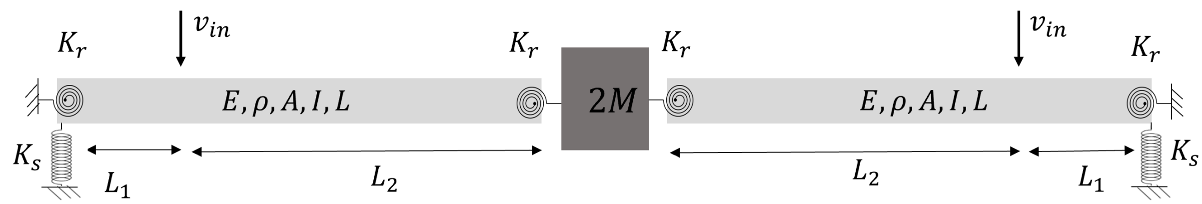

Figure 4.3. Schematic of a sliding beam with a tip mass and torsional hinges on both extremities

4.2 Unit Beam Model

Given the high feasibility of rubber in real life applications, the rubber isolator is designed to meet realistic isolator specifications shown in Table 4.1. Note that the isolation ratio is simply the ratio of the dynamic stiffness to the static stiffness, at a given frequency. The HSLDS requirement makes parallel stacking a reasonable design choice. Thus, the unit beam model used is that of a sliding beam connected to rotational springs on both ends, a linear spring on the root end, and subject to a displacement input v_{in} as shown in Figure 4.2.

The parallel two beam system with double the stiffness is shown in Figure 4.3. The rubber hinge is assumed to be compliant in the rotational and radial directions, represented by a rotational spring K_r and a linear translational spring K_s. The displacement transfer function is defined here as,

$$G_i(x_i, s) = \frac{W_i(x_i, s)}{V_{in}(x_i, s)} \tag{4.7}$$

where $W_i(x, s)$ is the transverse displacement of the beam and V_{in} is the input displacement, both in the Laplace domain. The beam model presented in chapter 2 and 3 is used to calculate the overall dynamic response of the beam. The boundary conditions at x_1=0 are as follows,

$$
\begin{aligned}
&\left[E^*I\frac{\partial^3 G_1(x_1,\omega)}{\partial x_1^3}\right]_{x_1=0} = 0 \\
&\left[Kr_1\frac{\partial G_1(x_1,j\omega)}{\partial x} - E^*I\frac{\partial^2 G_1(x_1,j\omega)}{\partial x_1^2} - \right]_{x_1=0} = 0
\end{aligned}
\tag{4.8}
$$

The boundary conditions at $x_2 = L_2$,

$$
\begin{aligned}
&\left[Kr_3\frac{\partial G_2(x_2,j\omega)}{\partial x_2} + E^*I\frac{\partial^2 G_2(x_2,\omega)}{\partial x_2^2} - \right]_{x_2=L_2} = 0 \\
&\left[E^*I\frac{\partial^3 G_2(x_2,\omega)}{\partial x_2^3} + M\omega^2 G_2(x_2,\omega)\right]_{x_2=L_2} = 0
\end{aligned}
\tag{4.9}
$$

The continuity conditions at $x_1 = L_1$ (also $x_2 = 0$) are as follows,

$$
\begin{aligned}
&[G_1(x_1,\omega]_{x_1=L_1} = [G_2(x_2,\omega]_{x_2=0} \\
&[G_1(x_1,\omega]_{x_1=L_1} = 1 \\
&\left[\frac{\partial G_1(x_1,\omega)}{\partial x_1}\right]_{x_1=L_1} = \left[\frac{\partial G_2(x_2,\omega)}{\partial x_2}\right]_{x_2=0} \\
&\left[\frac{\partial^2 G_1(x_1,\omega)}{\partial x_1^2} + Kr_2\frac{\partial G_1(x_1,\omega)}{\partial x_1}\right]_{x_1=L_1} = \left[\frac{\partial^2 G_2(x_2,\omega)}{\partial x_2^2}\right]_{x_2=0}
\end{aligned}
\tag{4.10}
$$

The dynamic stiffness of the sliding beam can be calculated by replacing the dimensional form of the transfer function ODE, equation (3.8), in the boundary and continuity conditions (4.8, 4.9, 4.10). The total dynamic stiffness is calculated by summing the dynamic stiffness of each beam such that,

$$
K_{dyntot} = \sum_{i=1}^{n} E^*IG'''_{1,i}(0, 25Hz) \tag{4.11}
$$

where n is the total number of beams and the index i denotes the corresponding beam.

4.2.1 Static and Dynamic Decoupling

Given the large static stiffness as well the large static displacement, it was found that it is very difficult to obtain a design with a reasonable weight and geometric dimensions within an acceptable strain and stress envelope. The isolator is subject to a static input and a displacement input, therefore the torsional strain in the rubber hinges are directly related to the displacement inputs and the beam geometry. The closer the input is to the rubber, the larger the torsional angle due to displacement. Therefore, to decrease the strain in the rubber, the displacement input should be placed well away from the hinge, however this would come at a cost of lower antiresonant forces, which can be mitigated by an increase in mass. Chapter 2, section 2.3, shows the trade-off between amplification ratio and mass, which, in this is case, is reflected as a trade-off between torsional strain, and tip mass.

Therefore, the static and dynamic displacement are decoupled in the proposed design. This is done by using an independent stiffness element, such that, during the static loading phase, only the stiffness elements are loaded. Once the static displacement is reached, the beams are then engaged, thereafter any dynamic displacement will be applied on both the stiffness elements and the beams. This is done by adding a distance offset between the input structure and the beams, while keeping the input in constant contact with the stiffness elements. The stiffness elements are chosen to be rubber pads subject to shear loading. The stiffness of the rubber pads is calculated as,

$$K_{pad} = \frac{G_{mod} A_c}{t} \tag{4.12}$$

Where A_c and t are the displaced area and the thickness of the rubber pad, respectively. The stiffness of the rubber pad is assumed to be constant, statically, and dynamically.

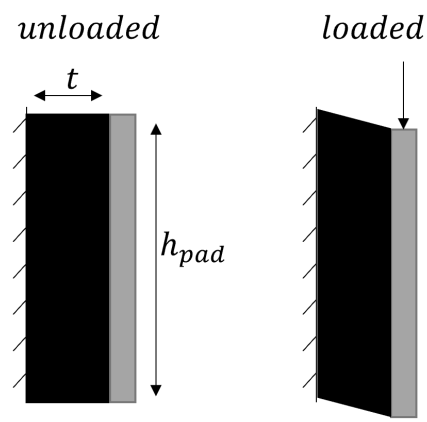

Figure 4.4. Schematic of an unloaded and loaded rubber shear pad

Table 4.2. Parameter generator ranges

Parameter	Range
d_i	$0.03 - 0.003$ m
d_o	$0.03 - d_i$ m
w	$0.05 - 0.01$ m
L_1	$0.07 - 0.01$ m
L_2	$0.07 - 0.01$ m
M	$1.5 - 0.05$ Kg

Therefore, the overall dynamic stiffness can be written as,

$$K_{dyntot} = \sum_{i=1}^{n} G_{1,i}(0, 25Hz) + K_{pad} \tag{4.13}$$

4.2.2 Design Methodology

In addition to the isolator specifications, the design should also meet a set of constraints. The constraints can be classified as geometric, stress-strain, and dynamic constraints. The weight of the isolator should be as small as possible, the lighter and smaller the isolator, the more feasible it is to be used in engineering applications. Also, the maximum number

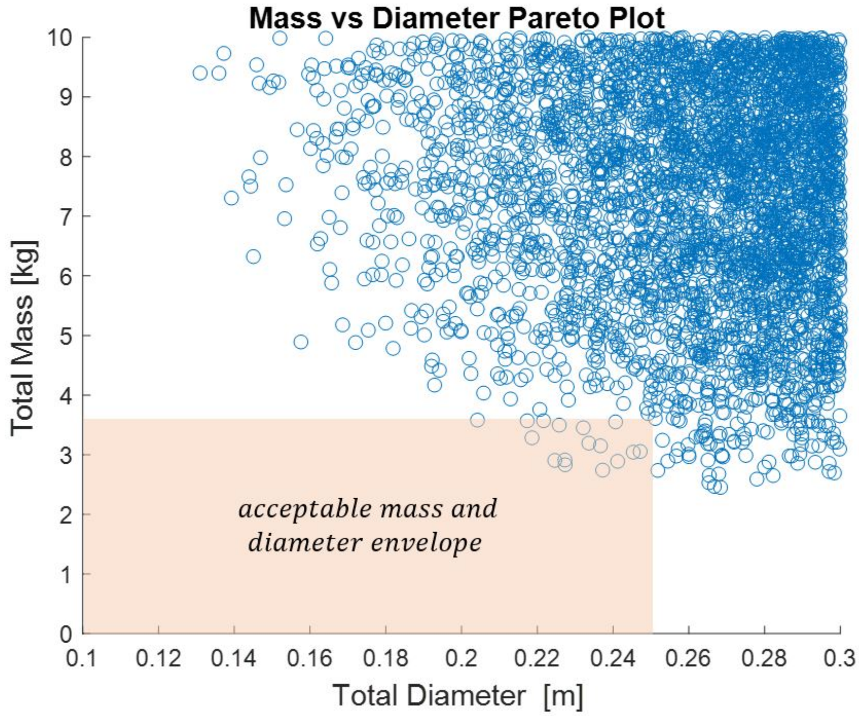

Figure 4.5. Pareto plot for different isolator designs subject to all design constraints but with a maximum radial strain of 5% and a maximum torsional strain of 20%, with the area in orange indicating an acceptable size and mass envelope such that maximum diameter is 25 cm and the maximum mass is 3.5 Kg.

of beams should be as small as possible, not to exceed 8 beams. Isolators with a very large number of beams are very difficult to manufacture with conventional manufacturing techniques. The number of beams is calculated such that there is a 70% reduction in force, the rubber pads are designed to provide a static stiffness equivalent to 7×10^6 N/m, assuming all the beams are identical, the number of beams needed, n, is calculated as follows,

$$n = \frac{4.9 \times 10^6}{|G_1(0, 25Hz)|.} \tag{4.14}$$

The stress limits are chosen such that the maximum dynamic stress in the beams does not exceed half the endurance limit (safety factor of 2). In this case, spring steel is chosen as the beam material, and the max stress limit is 300 Mpa. The dynamic stress denoted by σ_{dyn} is calculated using Euler-Bernoulli beam theory. The strain limit is chosen to be

20% for torsional strain, and 5% for radial strain. The dynamic constraint corresponds to the maximum isolation frequency. The maximum isolation frequency per beam is 25 Hz, this can be explained by equation (4.14), the beams should create a force large enough to cancel their own stiffness, as well as the stiffness of the rubber pad at 25 Hz. After the isolation frequency, the shear force at the root switches phase, opposite to the direction of the input force. Therefore, for the beams to collectively cancel the total input force, their individual isolation frequencies should be less than 25 Hz. To narrow down the design space, the following design methodology is used:

1. Choose the hinge and beam-mass parameters d_o-d_i-w_h-L_1-L_2-M-A-I
2. Calculate the hinge stiffnesses K_r-K_s
3. Calculate the torsional strain and check $\gamma_{tor} < 0.20$
4. Calculate the dynamic stiffness response for the beam K_{dyn}
5. Calculate the radial strain using the maximum dynamic radial displacement from the frequency response and check $\epsilon_{rad} < 0.05$
6. Check the isolation and natural frequency limits such that $\omega_{isolation} < 25$ Hz and $\omega_n > 35$ Hz
7. Calculate the total number of beams and total mass and check $n < 8$
8. Check for dynamic stresses not to exceed the endurance limit such that $\sigma_{dyn} < 300 Mpa$

The optimal design would be the one with the least mass and diameter within a reasonable stress and strain amplitude. To find that optimal design, large amounts of parameter combinations were generated and used in the first step in the design methodology. The parameter combinations that meet the constraints are saved and the total mass and

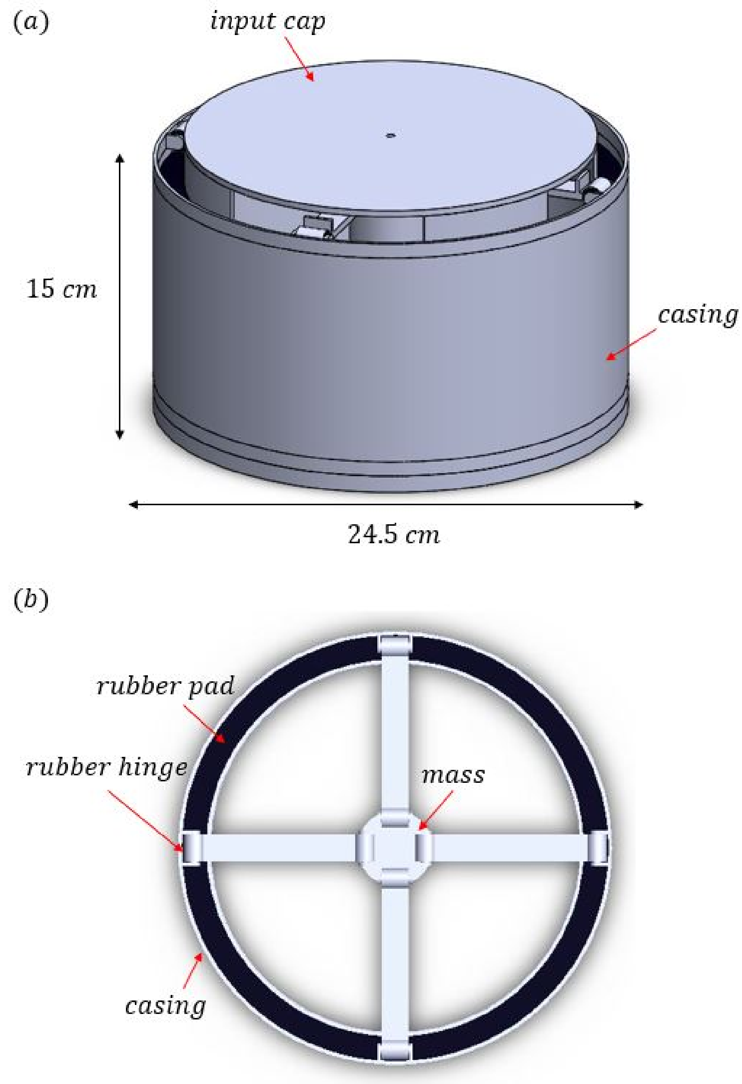

Figure 4.6. Drawing showing the proposed rubber hinge isolator with (a) showing a 3D isometric view and (b) showing a cross section view without the top input cap

diameter for each parameter set is plotted in Figure 4.5. The parameters were generated in specific ranges as shown in Table 4.2. The beam cross-sectional area is chosen to be rectangular with a base of 0.01 m and a height of 0.005m. The rubber shear modulus is chosen to range from $G_{mod} = 3 \times 10^5$ to $G_{mod} = 1 \times 10^6$ Pa, the beam Young's modulus is $E = 200$ Gpa with a density of $\rho = 7800\ Kg/m^2$. Note that the total mass is the summation of the beam tip masses, the masses of the beams, and an additional 2 Kg

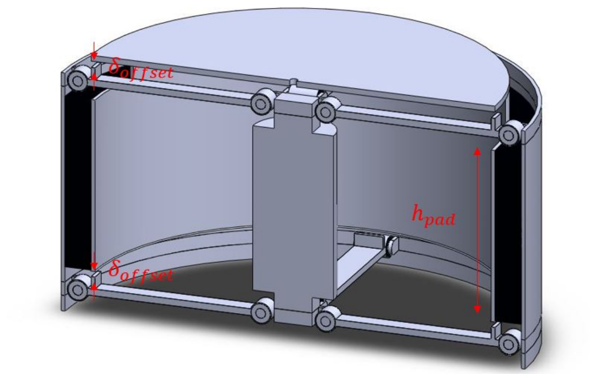

Figure 4.7. Drawing showing a lateral cross-sectional view proposed rubber hinge isolator

Table 4.3. Isolator and Beam Parameters

Parameter	Value
d_i	0.005 m
d_o	0.01 m
w	0.015 m
L_1	0.008 m
L_2	0.092 m
M	0.13 Kg

(estimated value) to amount for the mass of the hinges, rubber pads, input cap and casing. The additional mass is dependent on the detailed design of the isolator, which include the casing thickness, rubber pad dimensions, and input cap design.

4.2.3 Proposed Design

The chosen design parameters are close to that of the Pareto front knee in Figure 4.5. Figure 4.6-(a) shows a 3D dimetric view of the isolator. The outer diameter and height of the isolator are 24.5 cm and 15 cm, respectively. The input cap is excited, thus loading the rubber pads (statically and dynamically) and beams (dynamically). Figure 4.6-(b) shows a top view of the isolator without the input cap, the rubber pad is cylindrical

Table 4.4. Isolator geometric and weight properties

Parameter	Value
n beams	8
Total Mass	3.1 Kg
Total Diameter	0.245 m
Total Height	0.15 m

and shown to be in direct contact with the outer casing. Figure 4.7 shows a dimetric cross-sectional view of the isolator. The rubber hinges connect the beams to the outer casing on one side of the beam, and to the mass on the other side. The mass is cylindrical and connected to the hinges on the top and bottom. There is an offset distance δ_{offset} between the hinges and the input structure, the top beams engage the input cap, while the bottom beams connect to the cylindrical extension of the input cap that is connected to the rubber pad. To make sure there is constant engagement of the beams, the static offset is chosen to be equivalent to the difference of the static and maximum dynamic displacement,

$$\delta_{offset} = \delta_{static} - \delta_{dynamic} \tag{4.15}$$

The design parameters used for this design are shown in Table 4.3. Note that the total mass includes the mass of the beams, the casing, the input cap and its extension, as well as the rubber. The cylindrical rubber pad is chosen to be made a rubber pad with $G_{pad} = 17 \times 10^5$ Pa, and have an inner diameter of 0.209 cm, a thickness $t = 1.4$ cm, and a height $h_{pad} = 8.78$ cm. The max shear strain in the rubber pad is 29% at max displacement (static+dynamic). The rubber hinge is chosen to have a shear modulus $G_{mod} = 10^6$ Pa. The beam cross sectional area is chosen to be rectangular with a base of 0.015 m and a height of 0.0035 m. The geometric and weight properties are summarized

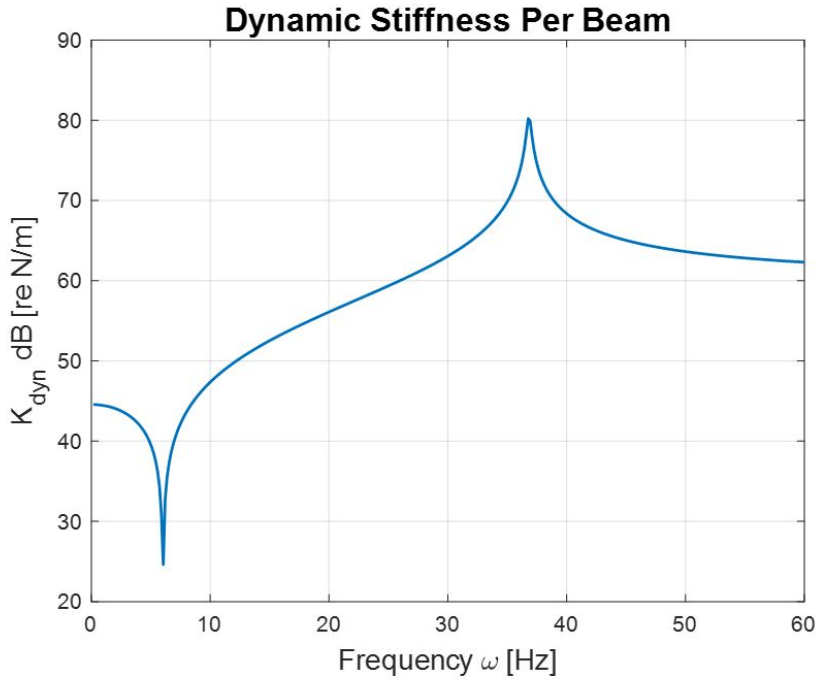

Figure 4.8. Dynamic stiffness frequency response for each beam

in Table 4.4. The beam and isolator dynamic stiffness frequency response is shown in Figures 4.8 and 4.9, respectively. The loss modulus is assumed to be $\tan\delta = 0.05$. The beam isolator frequency is much lower than the operating frequency at 25 Hz. The oscillation of the mass is fully cancelling the stiffness of rubber hinge at 6 Hz, after which the reaction force at the root, acting on the outer casing is in the opposite direction of the input force. The beam is tuned to provide 1.38% isolation ratio (no damping assumption) at 25 Hz, as shown in Figure 4.9. The isolator specifications are summarized in Table 4.5.

4.3 Proof of Concept

As a proof of concept, a rubber-based beam network is designed and built. In this case, the design is chosen to be connected to be similar to that of the flexible DAVI in chapter-3 but with an added linear spring on the root end, as shown in the unit beam

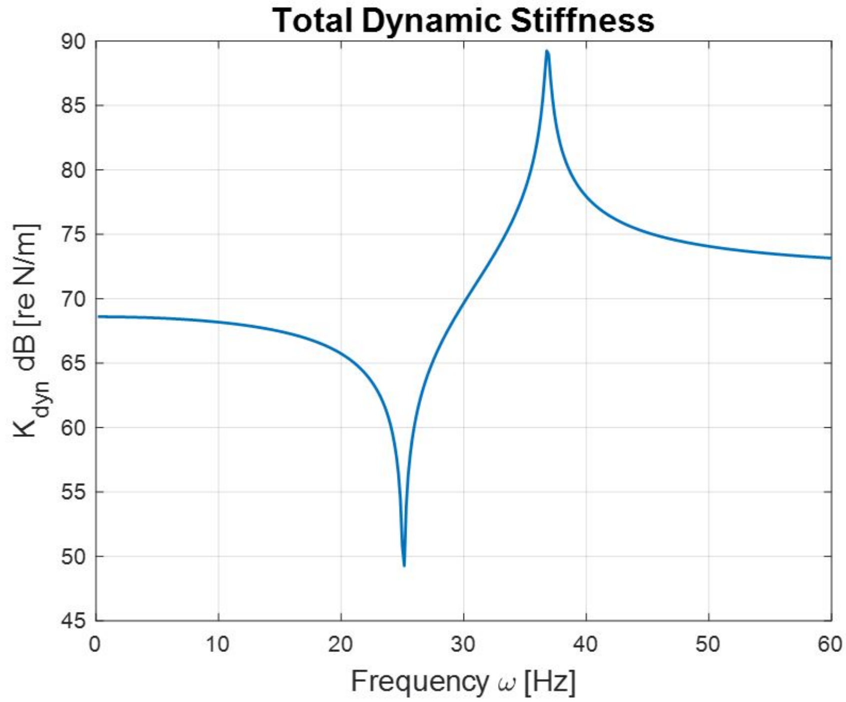

Figure 4.9. Total dynamic stiffness frequency response for the isolator

Table 4.5. Isolator specifications

Specification	Requirement	Provided
Static Stiffness	$7 \times 10^6 N/m$	$7 \times 10^6 N/m$
Isolation ratio at 25 Hz	$0\% - 30\%$	1.38%
Isolation ratio at 23 Hz	$0\% - 35\%$	25.76%
Isolation ratio at 27 Hz	$0\% - 40\%$	35.14%

model in Figure 4.10. For validation both force and displacement input conditions are conditions. Let $H(x, \omega)$ be a generic input function that can either be a force input with $H(\omega) = F_b(\omega)$, or a displacement input with $H(s) = V(s)$. Let the transfer function $G(x, s)$ be defined as,

$$G_i(x, s) = \frac{W_i(x, s)}{H(s)} \tag{4.16}$$

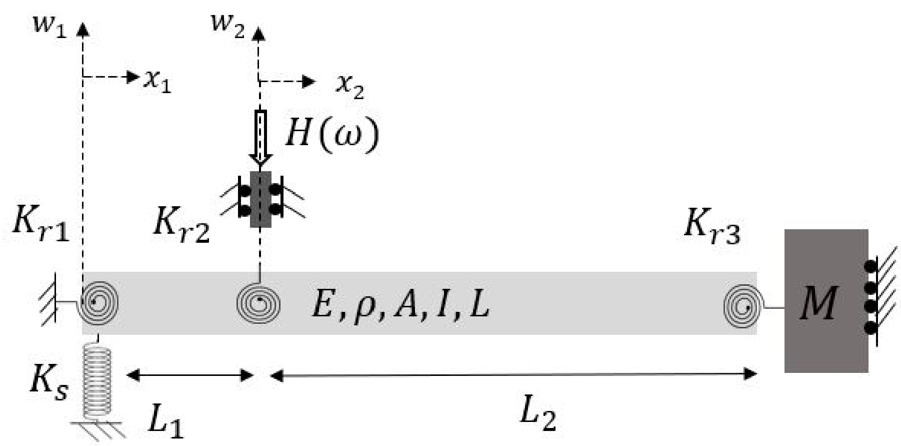

Figure 4.10. Unit beam model for proof of concept isolator.

The corresponding boundary conditions at $x_1 = 0$ are,

$$\begin{aligned}
&\left[E^* I \frac{\partial^3 G_1(x_1, \omega)}{\partial x_1^3} + K_s G_1(x_1, \omega)\right]_{x_1=0} = 0 \\
&\left[K r_1 \frac{\partial G_1(x_1, j\omega)}{\partial x} - E^* I \frac{\partial^2 G_1(x_1, j\omega)}{\partial x_1^2} - \right]_{x_1=0} = 0
\end{aligned} \tag{4.17}$$

The boundary conditions at $x_2 = L_2$,

$$\begin{aligned}
&\left[K r_3 \frac{\partial G_2(x_2, j\omega)}{\partial x_2} + E^* I \frac{\partial^2 G_2(x_2, \omega)}{\partial x_2^2} - \right]_{x_2=L_2} = 0 \\
&\left[E^* I \frac{\partial^3 G_2(x_2, \omega)}{\partial x_2^3} + M\omega^2 G_2(x_2, \omega)\right]_{x_2=L_2} = 0
\end{aligned} \tag{4.18}$$

The continuity conditions at $x_1 = L_1$ (also $x_2 = 0$) are as follows,

$$\begin{aligned}
&[G_1(x_1, \omega]_{x_1=L_1} = [G_2(x_2, \omega]_{x_2=0} \\
&\left[\frac{\partial G_1(x_1, \omega)}{\partial x_1}\right]_{x_1=L_1} = \left[\frac{\partial G_2(x_2, \omega)}{\partial x_2}\right]_{x_2=0} \\
&\left[\frac{\partial^2 G_1(x_1, \omega)}{\partial x_1^2} + K r_2 \frac{\partial G_1(x_1, \omega)}{\partial x_1}\right]_{x_1=L_1} = \left[\frac{\partial^2 G_2(x_2, \omega)}{\partial x_2^2}\right]_{x_2=0}
\end{aligned} \tag{4.19}$$

The input is part of the continuity conditions. For a displacement input,

$$[G_1(x_1,\omega) =]_{x_1=0} = 1 \tag{4.20}$$

For a force input,

$$\left[E^* I \frac{\partial^3 G_1(x_1,\omega)}{\partial x_1^3} + 1\right]_{x_1=L_1} = \left[E^* I \frac{\partial^3 G_2(x_2,\omega)}{\partial x_2^3}\right]_{x_2=0} \tag{4.21}$$

The solution for $G_i(x,s)$ can be calculated by plugging the boundary and continuity conditions in equation (3.8). The overall dynamic stiffness transfer function $K_{dyn}(\omega) = F_{out}/V_{in}$ can be calculated using the displacement input equation,

$$K_{dyn} = K + E^* I G_1'''(0,\omega) \tag{4.22}$$

Where K is the stiffness of the external spring elements. The force transmissibility transfer function $T(\omega) = F_{out}/F_{in}$ is calculated using the force input equation such that,

$$T(\omega) = \frac{-KG_2(0,\omega) + E^* I G_1'''(0,\omega)}{-KG_2(0,\omega) + 1 + \omega^2 M_t G_2(0,\omega)} \tag{4.23}$$

where M_t is the mass of the input structure.

4.3.1 Isolator Design and Experiment

A rod-end (Parker LORD R150P series [105]) is used as a rotational hinge by fixing the inner diameter to a fixed shaft. And a high deflection mount (Parker LORD MHDM series [105]) is used as a stiffness element (replacing the rubber pads in the above design). The isolator shown in Figure 4.11 is composed of an input-beam structure (white color) and a mount structure (black color) that are both additively manufactured with Polylactic acid (PLA) plastic. The input-beam structure is a single compliant structure that is

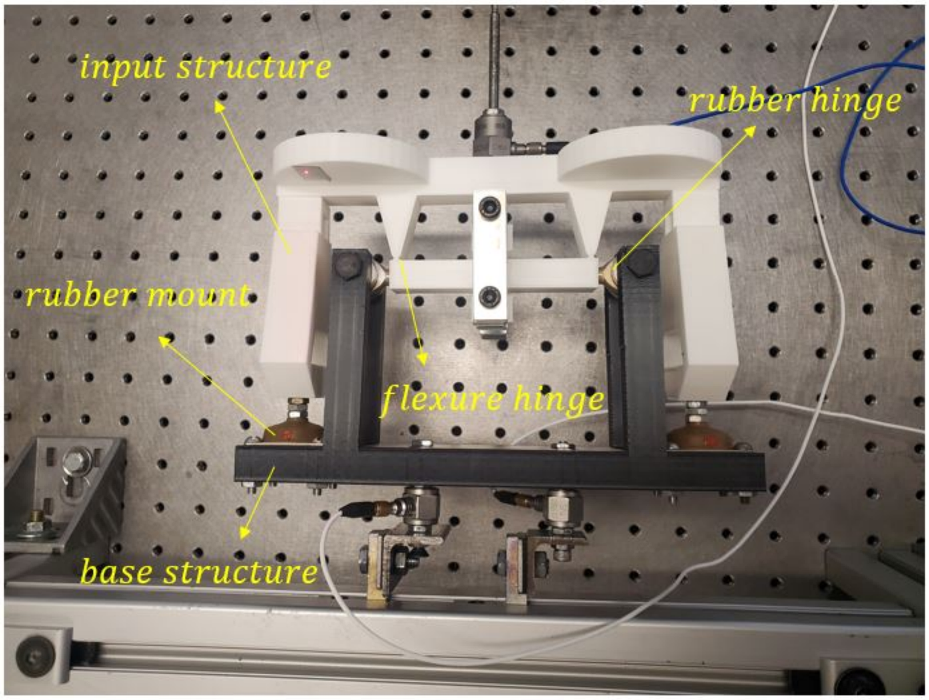

Figure 4.11. Labeled photograph showing the proposed isolator.

composed of a stiff structure on which the input force is applied, two tapered beams attach to the flexible beam via compliant flexure hinges that act as rotational springs. The beams attach to the mass via a compliant flexure hinge that also acts as a rotational spring. Rubber hinges are attached to the beams and connect to the mount structure via a rigid shaft connection, thus acting as rotational springs. The input structure is connected to the rubber mounts which are in turn, attached to the mount structure, acting as linear springs. The auxiliary mass is connected to the plastic mass structure. The radial stiffness of the hinge is assumed to be $K_s = 1.5 \times 10^5$ (from [105]). The rotational hinge stiffness is calculated using equation (4.2), with $G_{mod} = 3.3 \times 10^6$ Pa, $a = 0.0032$ m, $b = 0.0095$ m, $w_h = 0.009$ m (values extracted from [105]). The flexure stiffnesses on the input side and the mass side are identical, and their stiffnesses are estimated using equation (3.13). All stiffness values are summarized in Table 4.6. The beam is chosen to have a rectangular cross section, its geometric and material properties are in Table 4.7. The rubber mounts have a stiffness $K = 60,000$ N/m, with combined

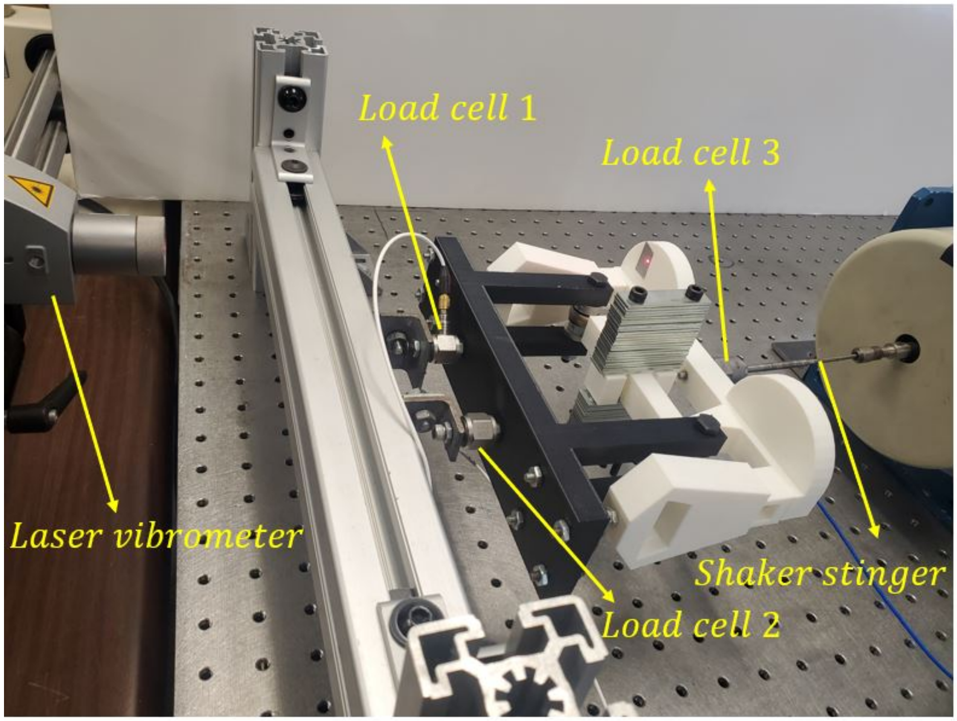

Figure 4.12. Labeled photograph showing the Experimental Setup.

Table 4.6. Isolator Rotational Stiffnesses

Hinge type	Rotational Stiffness
Rubber Hinge Kr_1	3.43 Nm/rd
Flexure Hinge 1 Kr_2	10 Nm/rd
Flexure Hinge 2 Kr_3	10 Nm/rd

stiffness of $120,000$ N/m. The mass of the input structure is measured to be 0.3 Kg. The per-beam tip is $M = 0.135$ Kg.

Figure 4.12 shows the experimental setup that includes the isolator mounted on a support structure one side, and connected to a shaker stinger on the other side. PCB-201C load cells are used to measure the force, load cell 1 connects the shaker stringer to the input structure and measures the total input force. Load cells 2 and 3 connect the mount structure to the support structure and measure the total output force. Additionally, a laser vibrometer is used to measure the displacement of the input structure. Note that there is no static preload condition in both experiments.

Table 4.7. Beam geometric and material properties

Property	Value
E	3 Gpa
L	5 cm
L_1	1.8 cm
A	2.6×10^{-4} m^2
I	3.66×10^{-6} m^4

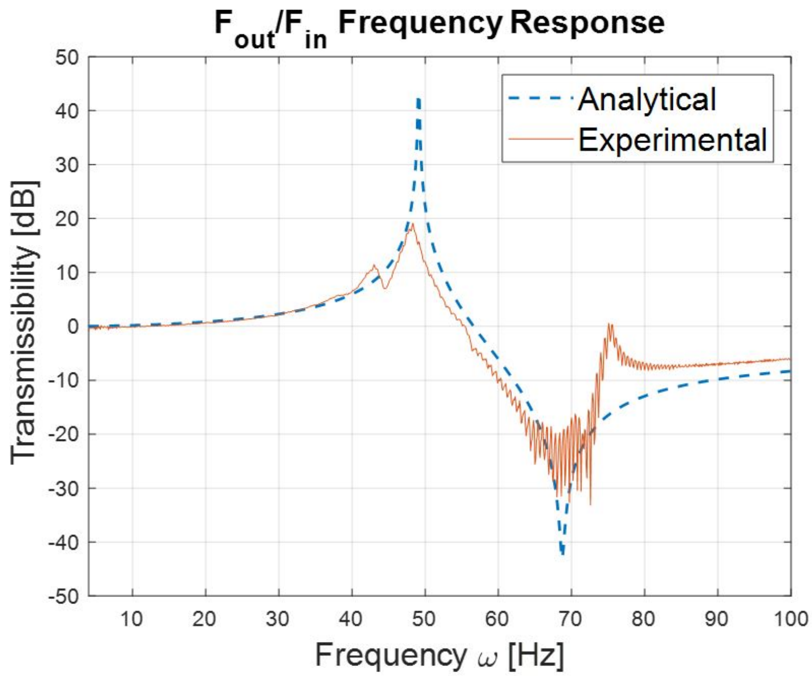

Figure 4.13. Graph showing the analytical vs experimental force frequency response.

4.3.2 Results and Discussion

The experimental and analytical force transmissibility response is shown in Figure 4.13. The loss modulus is assumed to be $\tan \delta = 0.2$. Overall, there is good agreement between the experiment and predicted results. The predicted isolation frequency (frequency with extremely low transmissibility) is almost identical to that of the experiment, although experimentally there is broader low-transmissibility range near the isolation frequency. Experimentally, there is a 90% force reduction, analytically the reduction is about 97%.

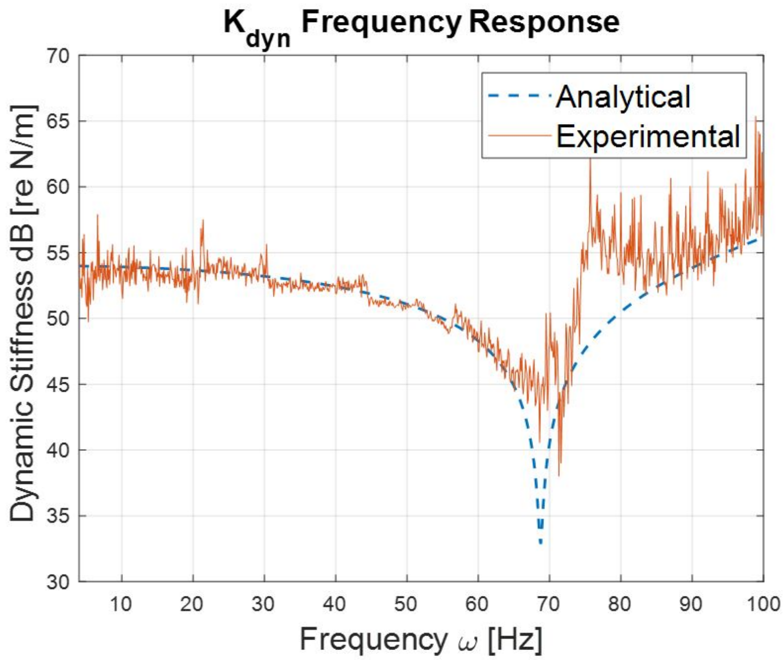

Figure 4.14. Graph showing the analytical vs experimental dynamic stiffness frequency response

The discrepancy is mainly caused by the load cell noise floor when subject to low force. The predicted natural frequency in this case is off by approximately 0.8 Hz. This is probably caused by printing tolerance errors in the thin flexure parts. Any variation in flexure thickness will change the stiffness of the rotational hinges, thus leading to changes in the frequency response.

Figure 4.14 shows the predicted dynamic stiffness response and the experiment. The loss modulus is also assumed to be $\tan\delta = 0.2$. It is shown that the predicted isolation frequency is almost identical to that of the experiment. Experimentally, there is a 93% reduction in stiffness at the isolation frequency, while the predicted reduction is 99% based on the analytical model. Note that theoretically there should be a 100% reduction in the absence of damping, the theoretical graph will approach 100% reduction as the frequency step limit decreases. The discrepancy is probably caused by damping that is unaccounted for in the model. Moreover, the isolation frequencies in both Figures 4.13 and 4.14 are identical in both the analytical prediction and the experiment. There is a small peak at 75.5 Hz that is consistent in both force and dynamic stiffness experiments, and it is not predicted by the model. This is probably caused by the dynamics of the rubber hinges and mounts, which have a high degree of damping and will act as independent isolators with their own resonances when loaded with mass. Moreover, some degree of error is caused by variation of elastomer stiffness of the mounts and rotational members. This causes a small degree of asymmetric loading which is not captured by the model.

Chapter 5

Series-Stacked Beam Network

5.1 Nodal Beam Stack Vibration Isolator

This chapter introduces monolithic compliant beam-network vibration isolators that are capable of generating several broad band gaps. The proposed nodal beam stack isolators can be fabricated using additive manufacturing by using features from compliant mechanisms such as flexure hinges. The complex structure of the proposed network is very difficult to manufacture with traditional subtractive manufacturing methods due to the small thicknesses and monolithic nature of the proposed network, thus the advantages of having such complex structures can only be realized with additive manufacturing.

Figure 5.1 shows a mass loaded nodal beam. The uniform beam parameters are the Young's modulus E, the density ρ, the air and strain damping c_a and c_s, cross sectional Area A, area moment of inertia I, and length L and end mass parameters (mass M and rotational inertia J) are chosen so the beam vibrates in a mode with nodal points at the ground connection. Thus, when the excitation frequencies coincide with the notch frequency, the ground reaction forces are very small. The oscillations of the masses will create a counter force that almost cancels the input force. The beam is symmetric and loaded at mid span. Figure 5.2 shows a schematic diagram of the proposed nodal beam stack vibration isolator consisting of n nodal beams stacked in series. The input force is

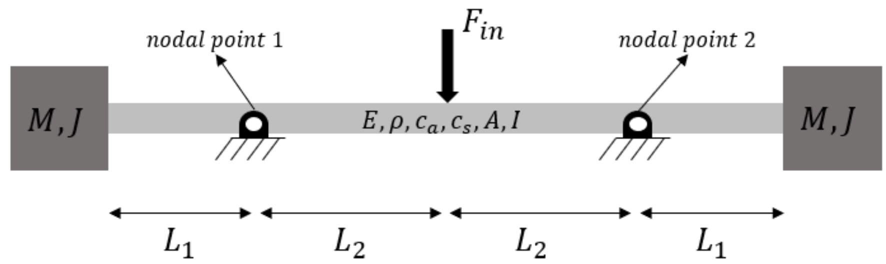

Figure 5.1. Schematic diagram of a mass-loaded nodal beam with mid-span force input

applied to the center of the top beam. The nodal points of this beam are connected by a rigid, y-shaped structure to the second beam. This pattern repeats through the stack. The nodal points of the last two beams however are directly connected without a Y. The output connects to the mid span of the nth beam. The beams are tuned for isolation at slightly different frequencies. These isolation frequencies are close enough to maintain force reduction and distributed to maximize the bandwidth. Nodal beam stack vibration isolators can be fabricated using additive manufacturing. The beams and end masses are all made from the same material. The rotational hinges at the nodal points are realized by circular flexure hinges.

5.2 Analytical Model

The nodal beam stack model shown in Figure 5.2 consists of n-beams. Each beam has two identical masses M_i with rotational inertia J_i at each end, with the subscript i indicating the beam level starting with $i = 1$ for the top beam and ending with $i = n$ for the bottom beam. Each beam has a length Lb_i, a cross sectional area A_i and an area moment of inertia I_i. The entire structure is assumed to be uniform and isotropic with a young's modulus E and a density ρ. The flexure hinges are represented as rotational springs with a stiffness Kr_i which can be calculated using the flexure geometry shown in Figure 5.3 where R is the notch radius, b is the notch depth, and h is the notch thickness.

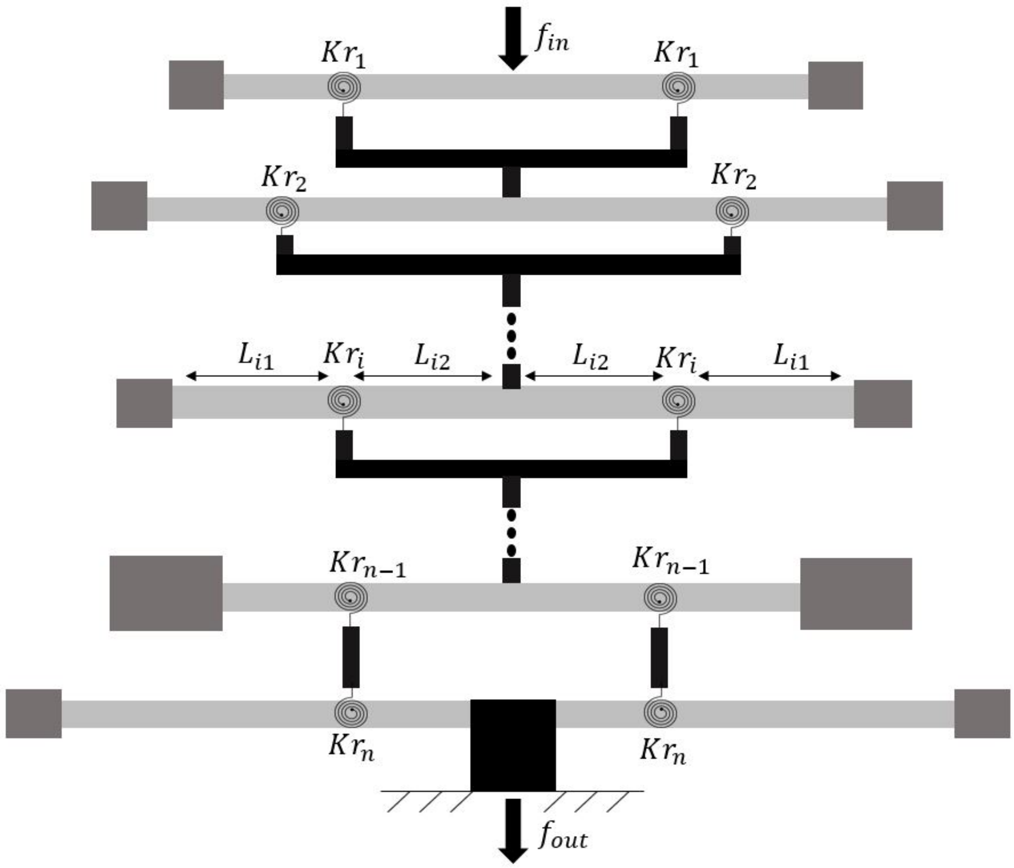

Figure 5.2. Schematic diagram of a nodal beam stack isolator.

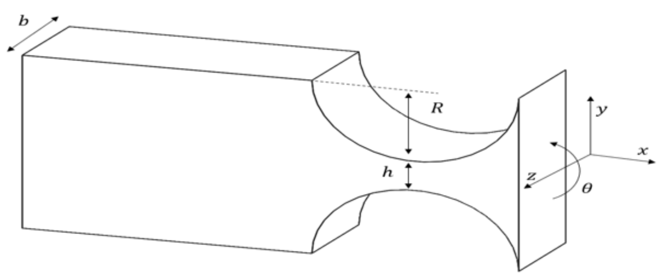

Figure 5.3. Schematic diagram of a circular notch flexure hinge

The stiffness of the rotational spring [99],

$$Kr_i = \frac{Ebh^3(2R+h)(4R+h)^3}{24R}\Bigg[h(4R+h)(6R^2+4Rh+h^2)$$

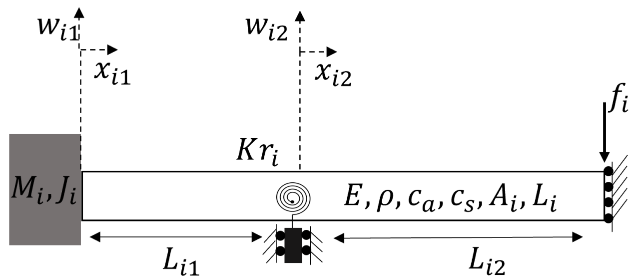

Figure 5.4. Schematic diagram of left half model.

$$+ 6R(2R+h)^2\sqrt{h(4R+h)}\,\mathrm{arctan}\left(\sqrt{1+\frac{4R}{h}}\right)\Bigg]^{-1} \quad (5.1)$$

Due to symmetry, we analyze only the left half of the structure with a vertically sliding boundary conditions for all the beams at the right end, the input force to this model is f_{in} and the output force is f_{out}. Figure 5.4 shows a diagram of the left half beam model divided into two parts each with length L_{ij} and a total length L_i, where the subscript $j = 1, 2$ for left and right parts of the beam, respectively. The transverse displacements w_{i1} and w_{i2} and horizontal coordinates x_{i1} and x_{i2} also correspond to the left and right parts. The input force at the sliding end is denoted by f_i such that the input force on the stack at the top beam is f_{in}, and $v_1 = f_{in}$. Transverse vibrations of a Euler Bernoulli beam are governed by,

$$EI_i\frac{\partial^4 w_{ij}}{\partial x_{ij}^4} + \rho A_i\frac{\partial^2 w_{ij}}{\partial t^2} + c_a\frac{\partial w_{ij}}{\partial t} + c_s\frac{\partial^5 w_{ij}}{\partial x_{ij}^4 \partial t} = 0, \quad (5.2)$$

where c_a is the air damping coefficient and c_s is the Kelvin-Voigt damping coefficient. Damping can also be accounted by using is the complex modulus E^* such that,

$$E_i^* = E^{'} + j_{im}E^{''}, \quad (5.3)$$

E is the Young's modulus (storage modulus) and E'' is the loss modulus, $j_{im} = \sqrt{-1}$. The complex Poisson's ratio v^* is assumed to be equal to the real Poisson's ratio v, based on [98]. The loss tangent is defined as

$$tan(\delta) = \frac{E''}{E} \tag{5.4}$$

Note that the linear damping model used in this case is suitable for small vibration amplitudes that do not exceed 15% of the beam length [106]. Even though the linear elasticity assumption might still be valid for large amplitudes, many studies have shown that large amplitude damping is nonlinear and more involved nonlinear models are needed [107, 108]. The following dimensionless variables are introduced, $\bar{x}_{ij} = x_{ij}/L_{ij}$, $\bar{w}_{ij} = w_{ij}/L_{ij}$ and $\bar{t}_{ij} = c_i t/L_{ij}^2$ where $c_i = \sqrt{\frac{EI_i}{\rho A_i}}$. After substituting the dimensionless variables, the dimensionless form of equation (5.2) becomes,

$$\frac{\partial^4 \bar{w}_{ij}}{\partial \bar{x}_{ij}^4} + \frac{\partial^2 \bar{w}_{ij}}{\partial \bar{t}_{ij}^2} + \bar{c}_{aij} \frac{\partial \bar{w}_{ij}}{\partial \bar{t}} + \bar{c}_{sij} \frac{\partial^5 \bar{w}_{ij}}{\partial \bar{x}_{ij}^4 \partial \bar{t}} = 0, \tag{5.5}$$

where $\bar{c}_{aij} = \frac{L_{ij}^2 c_i c_a}{EI_i}$ and $\bar{c}_{sij} = \frac{c_i c_s}{EL_{ij}^2}$. Taking the Laplace transform of (5.5) yields,

$$(1 + s_{ij}\bar{c}_{sij}) \frac{\partial^4 \bar{W}_{ij}}{\partial \bar{x}_{ij}^4} + (s_{ij}^2 + s_{ij}\bar{c}_{aij})\bar{W}_{ij} = 0, \tag{5.6}$$

where s_{ij} is the Laplace variable and $\bar{W}_{ij}(\bar{x}_{ij}, s_{ij})$ is the Laplace transform of $\bar{w}_{ij}(\bar{x}_{ij}, \bar{t})$. The displacement transfer function is defined as,

$$G_{ij}(x_{ij}, s_{ij}) = \frac{W_{ij}(x_{ij}, s_{ij})}{F_{in}(s_{ij})}, \tag{5.7}$$

where $F_{in}(s_i)$ is the Laplace transform of the input force $f_{in}(t)$ at $x_i = L_i$ such that $v_1 = f_{in}$. The dimensionless force input is then introduced as $\bar{f}_{in} = EI f_{in}/L_{12}^2$, and in the Laplace domain as $\bar{F}_{in}(\bar{x}, s_{12})$. The dimensionless force transfer function is defined as

$$\bar{G}_{ij}(\bar{x}_{ij}, s_{ij}) = \frac{\bar{W}_i(\bar{x}_{i,ij})}{\bar{F}_{in}(s_{12})} \tag{5.8}$$

Replacing eq. (5.8) in (5.5), and taking $s_{ij} = j_{im}\bar{\omega}_{ij}$ where $\bar{\omega}$ is the dimensionless excitation frequency such that $\bar{\omega}_{ij} = \frac{\omega L_{ij}^2}{c_i}$ and $j_{im} = \sqrt{-1}$, the transfer function ODE can be written as,

$$\frac{\partial^4 \bar{G}_{ij}(\bar{x}_{ij}, \bar{\omega_{ij}})}{\partial \bar{x_{ij}}^4} + \beta_{ij}^4 \bar{G}_{ij}(\bar{x}_{ij}, \bar{\omega_{ij}}) = 0 \tag{5.9}$$

such that,

$$\beta_{ij}^4 = \frac{\bar{\omega}_{ij}^2 - j_{im}\omega\bar{c}_{aij}}{1 + j_{im}\bar{c}_{sij}} \tag{5.10}$$

The solution of equation (5.9) is written as,

$$\begin{aligned} \bar{G}_{ij}(x_{ij}, \beta_{ij}) = \bar{G}_{ij}(0, \beta_{ij}) &\left[\frac{\cosh \beta_{ij}\bar{x}_{ij} + \cos \beta_{ij}\bar{x}_{ij}}{2\beta_{ij}^2}\right] \\ + \bar{G}'_{ij}(0, \beta_{ij}) &\left[\frac{\sinh \beta_{ij}\bar{x}_{ij} + \sin \beta_{ij}\bar{x}_{ij}}{2\beta_{ij}^3}\right] \\ + \bar{G}''_{ij}(0, \beta_{ij}) &\left[\frac{\cosh \beta_{ij}\bar{x}_{ij} - \cos \beta_{ij}\bar{x}_{ij}}{2\beta^2}\right] \\ + \bar{G}'''_{ij}(0, \beta_{ij}) &\left[\frac{\sinh \beta_{ij}\bar{x}_{ij} - \sin \beta_{ij}\bar{x}_{ij}}{2\beta^3}\right] \end{aligned} \tag{5.11}$$

The dimensionless ratio vectors are introduced,

$$r_i = \frac{Lp_{i1}}{L_i} \text{ for } i = 1, ..., n \tag{5.12}$$

$$Lbr_i = \frac{Lb_i}{Lb_{i+1}} \text{ for } i = 1, ..., n-1 \tag{5.13}$$

$$Ir_i = \frac{I_i}{I_{i+1}} \text{ for } i = 1, ..., n-1 \tag{5.14}$$

$$Ar_i = \frac{A_i}{A_{i+1}} \text{ for } i = 1, ..., n-1 \tag{5.15}$$

The dimensionless mass, rotational inertia and rotational stiffness are introduced as, $\bar{M}_i = \frac{M}{\rho A i L_{i1}}$, $\bar{J}_i = \frac{J_i}{\rho A i L_{i1}^3}$ and $\bar{K r}_i = \frac{K r_i L_{i1}}{E I_i}$, respectively. Each beam is periodically connected to the beams above it and below it in the stack. This applies to all the beams except for the first beam ($i = 1$) and the last two beams ($i = n-1$ and $i = n$). This is mainly because of the input force boundary condition in the first beam, and the fixed displacement condition in the last beam. The dimensionless boundary conditions can be classified into three groups, free end conditions, continuity conditions, and sliding end conditions. The free boundary conditions,

$$\begin{aligned} &\left[\frac{\partial^2 \bar{G}_{i1}(\bar{x}_{i1}, \beta_{i1})}{\partial \bar{x}_{i1}^2} + \beta_{i1}^2 \bar{J} \frac{\partial \bar{G}_{i1}(\bar{x}_{i1}, \beta_{i1})}{\partial \bar{x}_{i1}}\right]_{\bar{x}_{i1}=0} = 0, \text{ for } i = 1, ..., n-1, \\ &\left[\frac{\partial^3 \bar{G}_{i1}(\bar{x}_{i1}, \beta_{i1})}{\partial \bar{x}_{i1}^3} - \beta_{i1}^4 \bar{M} \bar{G}_{i1}(\bar{x}_{i1}, \beta_{i1})\right]_{\bar{x}_{i1}=0} = 0, \text{ for } i = 1, ..., n-1. \end{aligned} \tag{5.16}$$

The first two continuity conditions for *i=1,...,n* are,

$$\begin{aligned} &\left[\frac{\partial \bar{G}_{i1}(\bar{x}_{i1}, \beta_{i1})(\bar{x}_{i1}, \beta_{i1})}{\partial \bar{x}_{i1}}\right]_{\bar{x}_{i1}=0} = \left[\frac{\partial \bar{G}_{i2}(\bar{x}_{i2}, \beta_{i2})}{\partial \bar{x}_{i2}}\right]_{\bar{x}_{i2}=0}, \\ &\left[\frac{\partial^2 \bar{G}_{i1}(\bar{x}_{i1}, \beta_{i1})}{\partial \bar{x}_{i1}^2} - \bar{K r}_i \frac{\partial \bar{G}_{i1}(\bar{x}_{i1}, \beta_{i1})}{\partial \bar{x}_{i1}}\right]_{\bar{x}_{i1}=1} = \frac{r_i}{1-r_i} \left[\frac{\partial^2 \bar{G}_{i2}(\bar{x}_{i2}, \beta_{i2})}{\partial \bar{x}_{i2}^2}\right]_{\bar{x}_{i2}=0}, \\ &\frac{r_i}{1-r_i} \left[\bar{G}_{i1}(\bar{x}_{i1}, \beta_{i1})\right]_{x_{i1}=0} = \left[\bar{G}_{i2}(\bar{x}_{i2}, \beta_{i2})\right]_{x_{i2}=0}. \end{aligned} \tag{5.17}$$

The fourth continuity condition continuity condition for *i=n-1* is as follows,

$$\frac{1-r_{n-1}}{1-r_n} \left[\bar{G}_{(n-1)2}(\bar{x}_{(n-1)2}, \beta_{(n-1)2})\right]_{x_{(n-1)2}=0} = \left[\bar{G}_{(n)2}(\bar{x}_{(n)2}, \beta_{n2})\right]_{x_{n2}=0} \tag{5.18}$$

and for *i=n*,

$$\left[\frac{\partial^3 \bar{G}_{n1}(\bar{x}_{n1},\beta_{n1})}{\partial \bar{x}_{n1}^3}\right]_{x_{n1}=1} - \left(\frac{r_n}{1-r_n}^2\right)\left[\frac{\partial^3 \bar{G}_{n2}(\bar{x}_{n2},\beta_{n2})}{\partial \bar{x}_{n2}^3}\right]_{x_{n2}=0} =$$
$$Ir_n\left(\frac{r_n}{Lbr_{n-1}r_{n-1}}\right)^2\left[\frac{\partial^3 \bar{G}_{(n-)1}(\bar{x}_{(n-1)1},\beta_{(n-1)1})}{\partial \bar{x}_{(n-1)1}^3}\right]_{x_{(n-1)1}=1} -$$
$$Ir_n\left(\frac{r_n}{Lbr_n(1-r_{n-1})}\right)^2\left[\frac{\partial^3 \bar{G}_{(n-1)2}(\bar{x}_{(n-1)2},\beta_{(n-1)2})}{\partial \bar{x}_{(n-1)2}^3}\right]_{x_{(n-1)2}=0}. \quad (5.19)$$

There are two sliding end boundary conditions for each beam, the zero-slope condition applies to all beams in the stack,

$$\left[\frac{\partial^2 \bar{G}_{i2}(\bar{x}_{i2},\beta_{i2})}{\partial \bar{x}_{i2}^2}\right]_{\bar{x}_{i2}=1} = 0, \text{ for } i=1,...,n \quad (5.20)$$

The other sliding end condition is force or displacement related, the first beam is subject to the force input, all other beams except for the bottom beam have a shear force transfer condition, and the last beam has a zero-displacement condition due to the cantilever root. Therefore, for *i=1*,

$$\left[\frac{\partial^3 \bar{G}_{12}(\bar{x}_{12},\beta_{12})}{\partial \bar{x}_{12}^2}\right]_{\bar{x}_{12}=1} = 1 \quad (5.21)$$

and for *i=2,..,n-1*,

$$\left[\frac{\partial^3 \bar{G}_{i2}(\bar{x}_{i2},\beta_{i2})}{\partial \bar{x}_{i2}^2}\right]_{\bar{x}_{i2}=1} =$$
$$Ir_{i-1}\left(\frac{1-r_i}{Lbr_{i-1}r_{i-1}}\right)^2\left[\frac{\partial^3 \bar{G}_{(i-1)1}(\bar{x}_{(n-1)1},\beta_{(n-1)1})}{\partial \bar{x}_{(n-1)1}^3}\right]_{x_{(n-1)1}=1} -$$
$$Ir_{i-1}\left(\frac{1-r_i}{Lbr_{i-1}(1-r_{i-1})}\right)^2\left[\frac{\partial^3 \bar{G}_{(i-1)2}(\bar{x}_{(i-1)2},\beta_{(i-1)2})}{\partial \bar{x}_{(i-1)2}^3}\right]_{x_{(n-1)2}=1} \quad (5.22)$$

For *i=n*,

$$\left[\bar{G}_{n2}(\bar{x}_{n2},\beta_{n2})\right]_{\bar{x}_{n2}=1} = 0 \quad (5.23)$$

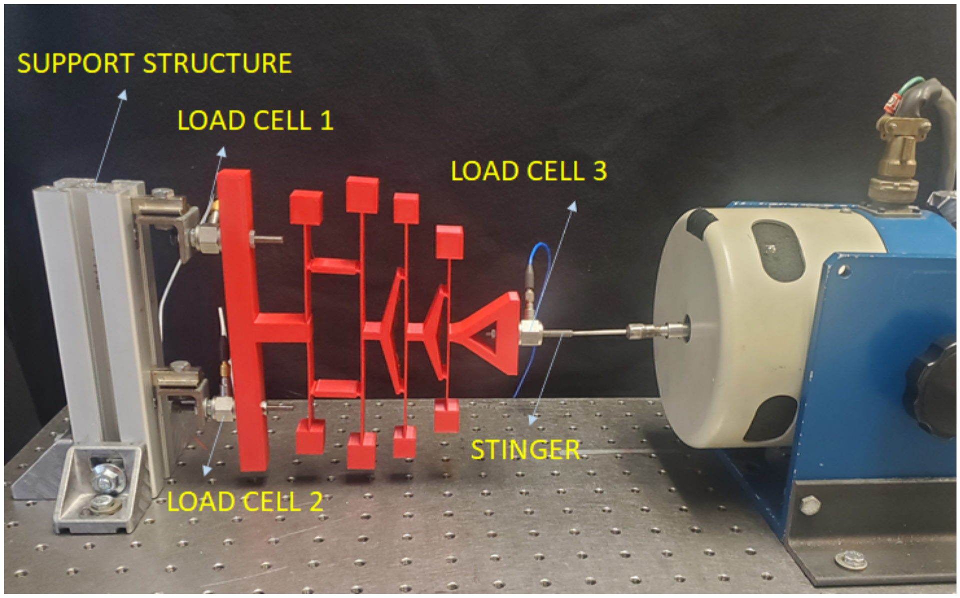

Figure 5.5. Photograph showing the experimental setup

The solutions for $\bar{G}_{ij}(0, \beta_{ij})$, $\bar{G}'_{ij}(0, \beta_{ij})$, $\bar{G}''_{ij}(0, \beta_{ij})$ and $\bar{G}'''_{ij}(0, \beta_{ij})$ in equation (5.11) can be solved by replacing (5.11) in the aforementioned boundary conditions (5.16 - 6.27). The equations are all linear and can solved by matrix inversion. Each beam is associated with 8 boundary conditions, so an $8n \times 8n$ and the matrix is populated and inverted numerically. The output force is twice the shear force at cantilever root connection. The output force is therefore,

$$\bar{F}_{out} = 2 \left[\frac{\partial^3 \bar{G}_{n2}(\bar{x}_{n2}, \beta_{n2})}{\partial \bar{x}_{n2}^3} \right]_{x_{n2}=1} . \tag{5.24}$$

5.3 Four Beam Isolator

The four beam isolator shown in Figure 5.5 was designed and experimentally tested for vibration isolation. The experiment was performed with no static preload. The geometric parameters are shown in Table 5.1. The flexure hinge radius is $R = 0.00145$ m, with a notch $h = 0.0011$ m and a depth of $b = 0.02$ m, with an overall rotational stiffness

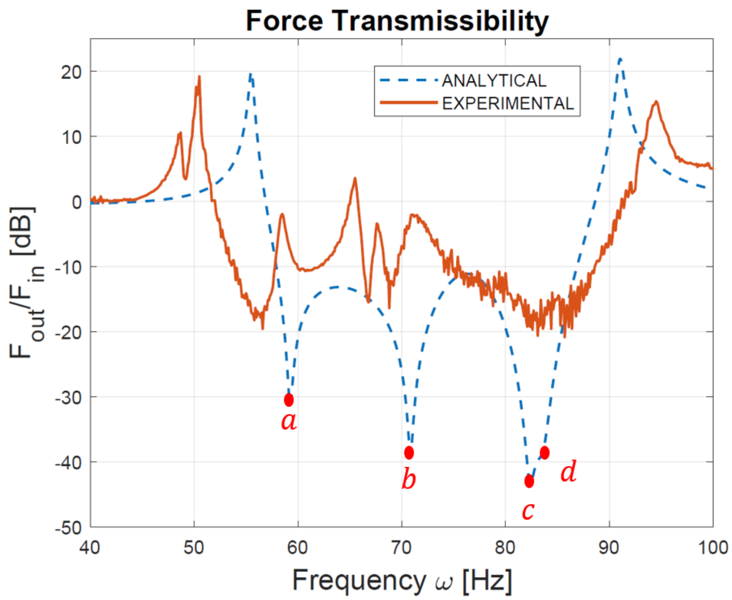

Figure 5.6. Frequency response of the analytical model (dotted) and the experiment(solid) with the red dots labeled a-b-c-d indicating the four analytical isolation frequencies

Table 5.1. Geometric and tip mass properties of four beam isolator

Beam index	L_{i1}	L_{i2}	$Height$	M	J
1	0.023 m	0.0245 m	$0.001m$	0.002 Kg	$7.57 \times 10^{-7} Kgm^2$
2	0.033 m	0.0345 m	$0.0013m$	0.0035 Kg	$4.80 \times 10^{-7} Kgm^2$
3	0.035 m	0.0375 m	$0.0015m$	0.0042 Kg	$1.08 \times 10^{-6} Kgm^2$
4	0.026 m	0.034 m	$0.001m$	0.0037 Kg	$8.37 \times 10^{-5} Kgm^2$

$Kr = 3.29$ N/rd. The analytical model was used to predict the frequency response, the following dimensional transformation is used for the output force,

$$F_{out} = \frac{EI_4}{L_{12}^2}\bar{F}_{out} = \frac{EI_4}{L_{12}^2}\left[\frac{\partial^3 \bar{G}_{42}(\bar{x}_{42}, \beta_{42})}{\partial \bar{x}_{42}^3}\right]_{x_{42}=1} \tag{5.25}$$

The 3D printer material was PLA, and a Young's modulus of $E = 2Gpa$ is assumed based on the experimental results for PLA specimen printed with the same parameters in [109]. The viscoelastic damping coefficient was tuned for a 50 % viscoelastic damping ratio one the first transverse vibration mode, based on PLA plastic damping properties in [110]. The damping coefficients are calculated using the following equation [111],

$$c_{si} = \frac{2\zeta E I_i}{\omega_1} \tag{5.26}$$

where ω_1 is the first mode natural frequency. The damping coefficients were found to be $c_{s1} = 9.64 \times 10^{-6}$Nsec/m^2, $c_{s2} = 2.11 \times 10^{-5}$Nsec/m^2, $c_{s3} = 3.25 \times 10^{-5}$Nsec/m^2, and $c_{s4} = 9.64 \times 10^{-6}$Nsec/m^2. The density of the structure was measured based on weight and volume calculation of the printed stack. The geometry was designed to provide a wide band gap around 32 Hz. We define the bandgap to be the frequency range with force reduction or $|F_{out}|/|F_{in}| < 1$. The theoretically predicted transmissibility frequency response (see Figure 5.6) shows a deep and wide band gap that extends from 57 to 89 Hz, centered on 73 Hz. The overall band gap width is 32 Hz.

The analytical model was verified experimentally using a four-beam stack 3D printed using an 'Ender 3 Pro' FDM type 3D printer at a 45-degree raster angle with 0.2 mm layer thickness, 120 mm/sec print speed, 200° C extrusion temperature. The experiment setup shown in Figure 5.5 includes two 'PCB 208C01' load cells mounted on a support fixed structure. A 'Ling LMT100' shaker stinger was connected to the top beam via a ' PCB 208CO2' load cell. The shaker was excited with a chirp signal at a voltage amplitude of 0.2 volts with a frequency sweep from 40 Hz to 100 Hz over 60 seconds. The load cell voltages were processed through a PCB 482C-series signal conditioner and recorded by an NI Data Acquisition device. A Fast Fourier transform algorithm calculated the frequency response from the time series data.

The experimental frequency response shown in Figure 5.6 has approximately the same band gap center as predicted by theory (1 Hz offset). A wide and deep band gap around 72 Hz was recorded. The experimental band gap (40 Hz) is wider than the theoretically predicted (32 Hz) but shallower (-20.8 dB max) than theory (-43.2 dB max). The comparison between the experimental and analytical results is summarized in

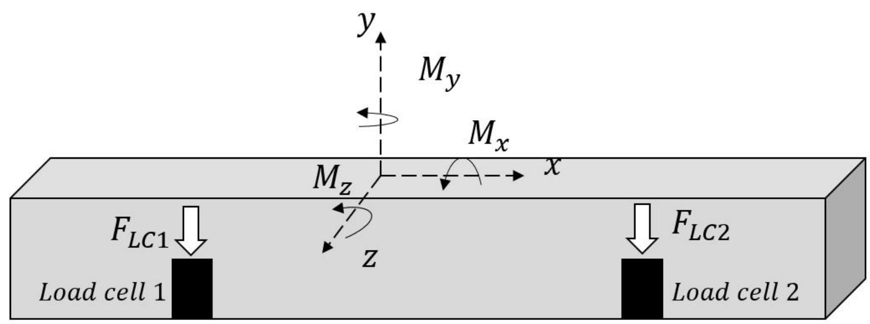

Figure 5.7. Drawing showing the rotational and torsional modes in the load cell plane of measurement. With M_x causing in-plane rotation, M_y causing out-of-plane rotation, and M_z causing torsion (twisting).

Table 5.2. The experimental band gap is shallower and less defined and penetrated by a resonance peak around 65 Hz that is not observed by theory. Additional peaks around 58 Hz and 68 Hz were not predicted by theory. The theoretical model assumed consistent and symmetrical properties of the beams and masses. The 3D printed experimental model contains asymmetry due to variations in beam thickness, especially in the thin sections and flexure notches. Additionally, variation in Young's Modulus, unmodeled flexure elasticity, and noise from the load cells as well as limited load cell resolutions also contribute to the deviations from the clean theoretical prediction. Furthermore, the linear damping model employed in this case is only suitable for small amplitude vibrations, which could explain the discrepancy near the resonant peaks where the vibration amplitude drastically increases [107]. The large theoretical bandgaps could be difficult to realize in experiments, particularly due to the small disturbances that can cause transmissibility peaks in the middle of the bandgap. Additional experimental data is presented in Appendix B to show repeatability of results.

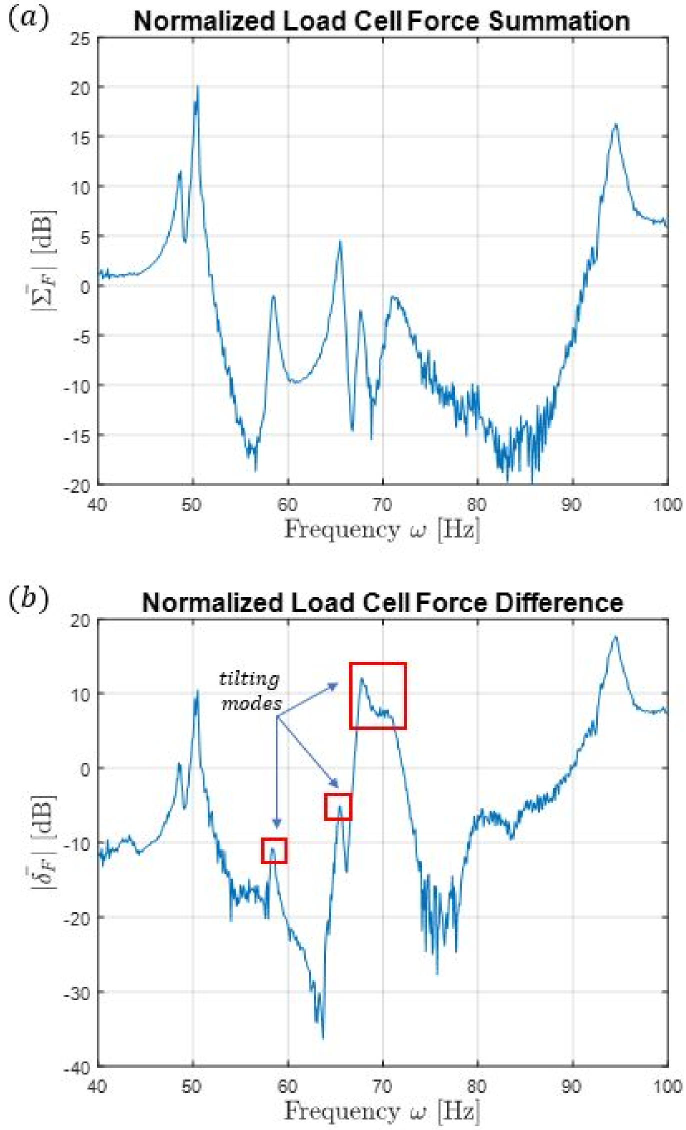

Figure 5.8. Graph showing the summation (a) and difference (b) of the forces measured by load cells 1 and 2, both normalized by the input force measured by load cell 1 shown in Figure 2.9.

5.3.1 Rotational Mode Analysis

The relatively small peaks penetrating the band gap at 58 Hz and 68 Hz are not predicted by theory. The theoretical model only accounts for transverse modes, however the load cells also capture out-of-plane, torsional modes, and in-plane rotational modes that come from shaker misalignment, or from isolator asymmetries. Figure 5.7 shows the rotational

Table 5.2. Comparison between experimental and analytical frequency response

Band Gap	Range	Center	Center Depth	Max Depth
Analytical	57-89 Hz	73 Hz	-17 dB	-43.2 dB
Experimental	52-92 Hz	72 Hz	-4 dB	-20.8 dB

and torsional modes in the load cell plane of measurement. In-plane modes are caused by bending along the x-axis, out-of-plane rotational modes are caused by bending along the y-axis, and torsional modes are caused by twisting along the z-axis (see Figure 5.7).

Figure 5.8 shows the sum of forces measured by load cells 1 and 2, as well as the force difference normalized by the input force over the experimental frequency range. This is calculated by taking the magnitude of the FAST FOURIER TRANSFORM (FFT) of the difference of the measured forces in the load cells 1 and 2, and dividing that by the magnitude FFT of the input force,

$$\bar{\Delta}_F = \frac{|FFT(F_{LC1} - F_{LC2})|}{|FFT(F_{in})|} \tag{5.27}$$

where $\bar{\Delta}_f$ is the normalized force difference, F_{LC1} and F_{LC2} are the forces measured by the load cells 1 and 2, respectively. The normalized force summation is,

$$\bar{\Sigma}_F = \frac{|FFT(F_{LC1} + F_{LC2})|}{|FFT(F_{in})|} \tag{5.28}$$

When the force difference is large, this would indicate either a resonance frequency in the transverse mode, or an out-of-plane rotational mode, or a torsional mode.:

- The transverse mode resonance is characterized by large forces in the transverse direction which could lead to a large force difference between the load cells. Since this is the main mode of excitation, these modes are well pronounced on the experimental transmissibility plot. Therefore, the resonant peaks in Figure 5.8 are at 50.5 Hz and 94.6 Hz, which in-line with the resonant peaks in the summation plot in Figure 5.6.

- The out-of-plane tilting modes as well as the torsional modes will also lead to a large difference of forces between the two load cells, mainly because the load cells will be in opposite phase. Out-of-plane or torsional modes will be represented as small peaks in the transmissibility response (normalized force summation plots), and are not as pronounced as transverse modes. Therefore, the out-of-plane modes are at 66 Hz, 68 Hz and 72 Hz, which is in-line with the small peak penetrations in the band gap in the transmssibility plot in Figure 5.6.

- In-plane modes tilting modes do not lead to a difference in load cell force measurements. However, in-plane tilting modes that are at a slight angle can lead to small force differences. Mainly because the skewed in-plane tilting direction could lead to slightly higher forces in one of the load cells. This would result in small peaks in the force difference plots. Therefore, the small peak at 58 Hz in Figure 5.8 would resemble an in-plane tilting mode that is in-line with the small peak at 58 Hz in the transmissibility plot in Figure 5.6.

Overall, there seems to be a sensitivity to off-axis loading, for typical vibration isolators off-axis vibration resulting from load misalignments are usually handled by high tilting stiffness adapters that ensure a properly aligned load-path passing through the isolator. More information on high tilting stiffness adapters can be found in Appendix C.

5.3.2 Displacement Propagation

Figure 5.9 shows the analytical displacement distributions at the four isolation frequencies. The color describes the transverse displacement along the lengths of

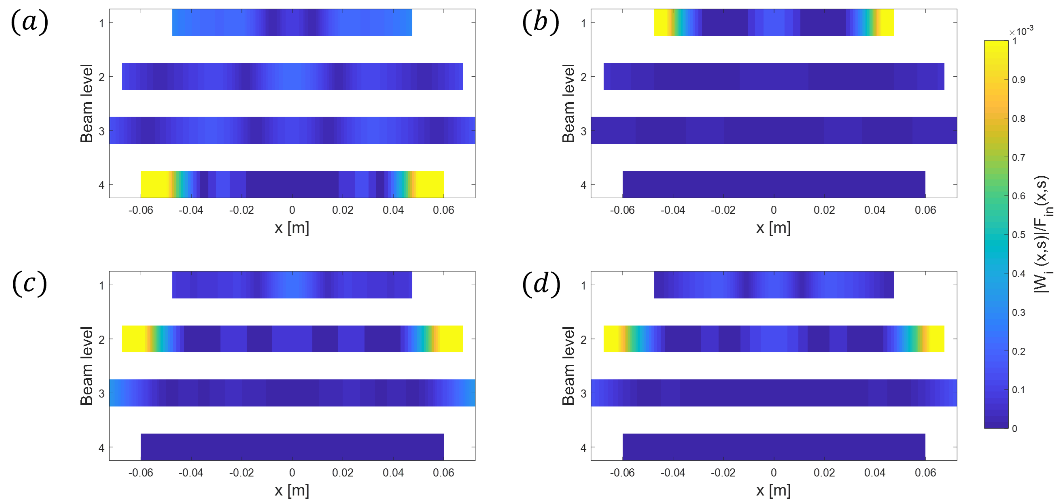

Figure 5.9. Color map plots of four nodal beam displacement magnitude distributions at isolation frequencies (a)-(d) in Figure 5.6

the beams. Figure 5.9-a shows that primarily beam 4 is oscillating at 59.05 Hz, thus the oscillations of beam 4 is causing an isolation frequency. Figure 5.9-(b) shows that there is no vibration propagating to the lower level beams beyond beam 1, indicating that the isolation frequency at 70.66 Hz is primarily due to the oscillations of beam 1. Figure 5.9-(c-d) show isolation due to the 3rd beam is at 82.38 Hz, and 2nd beam at 83.75 Hz. This demonstrates how the system creates a band gap since if any one beam in the stack hits its isolation frequencies, little force is transmitted through the stack.

5.4 Higher Order Isolators

Designing a multiple beam isolator can be tedious due to the multiple parameters. The main design goal is to tune the isolation frequencies to be very close in order to obtain a band gap. One method that works well is to start with identical beams and target a specific isolation and natural frequency by changing the thickness of

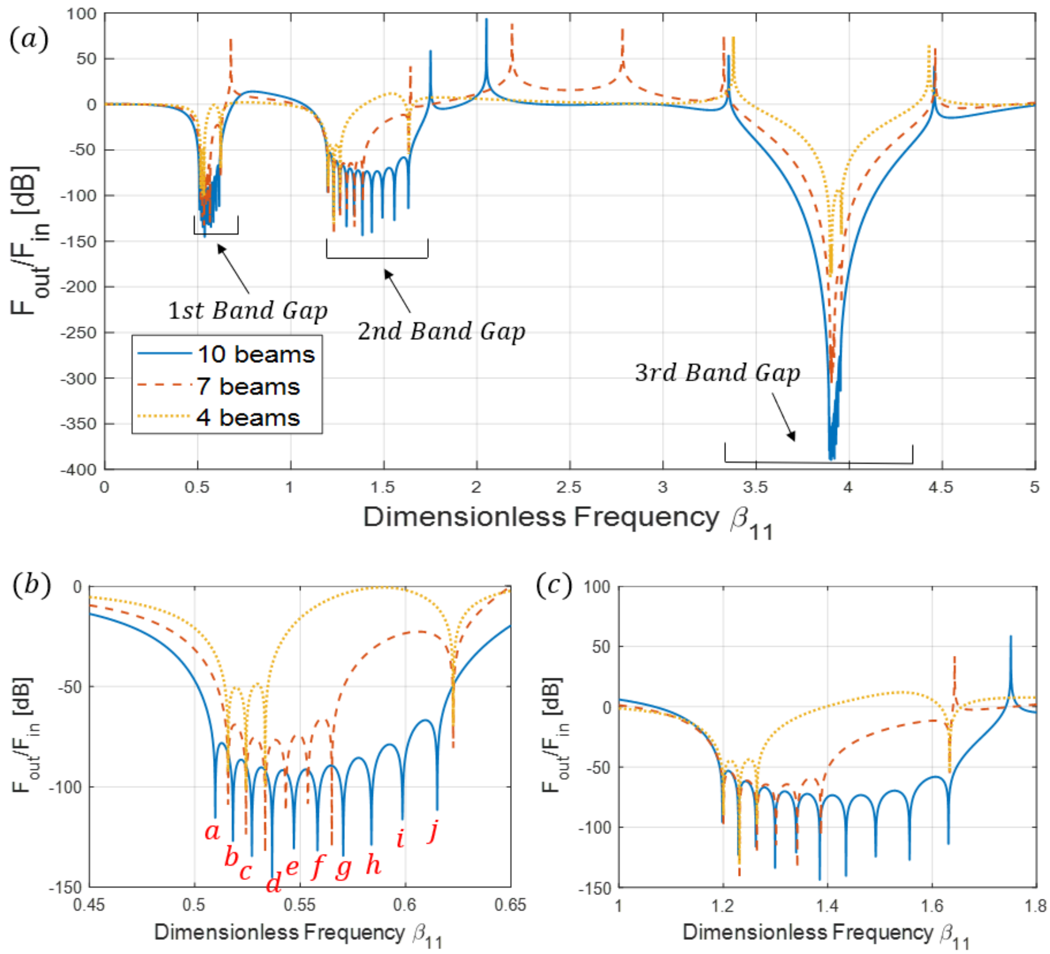

Figure 5.10. Dimensionless force transmissibility frequency response plots of the 10 beam stack (solid), the 7 beam stack (dashed), and the 4 beam stack (dotted): (a) shows the wide frequency range, (b) and (c) zoomed in to the first and second band gap, respectively.

the beam, the rotational stiffness and the distance between input location and the nodal point. It can be seen that the closer the input is to the nodal point, the further is the mass, which leads to higher antiresonant forces. The next step is to change one parameter that will affect the frequencies while keeping all other parameters the same. The simplest parameter to change is the mass, changing the nodal point is also an option. By using small mass changes the isolation frequencies will start shifting.

Using the model, we explore the improved performance provided by 7 and 10 beam

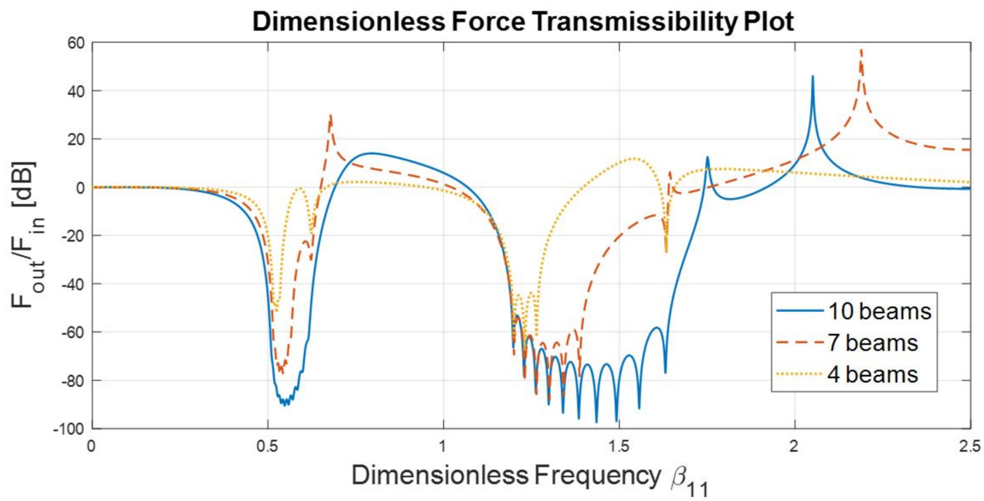

Figure 5.11. Dimensionless force transmissibility frequency response plots of the 10 beam stack (solid), the 7 beam stack (dashed), and the 4 beam stack (dotted) with damping such that the loss tangent $\tan\delta = 0.1$.

stacks. We assume identical beam geometry but different tip masses with $m_1 = 4.27$, $m_n = 3.84$, and $\bar{m}_i = \bar{m}_{i-1} + 0.4274$ for i=2,..,n-1. The mass difference is tuned to achieve a cluster of isolation frequencies. The rotational inertia follows a similar pattern such that $\bar{J}_1 = 0.5073$, $\bar{J}_n = 0.4109$ with $\bar{J}_i = \bar{J}_{i-1} + 0.1065 + 0.01(i-2)$ for i=2,...,n-1. The dimensionless flexure stiffness is $\bar{Kr}_i = 0.37$. For comparison, a 7 beam stack (without the first 3 beams) and a 4 beam stack (without the first 6 beams) are analyzed.

Figure 5.10 shows the force transmissibility frequency response of the 10, 7 and 4, beam stacks. The frequency range is expanded to show 3 band gaps. Each band gap consists of isolation frequencies clustered next to each other. The 10 beam stack has 10 isolation frequencies in each band gap. The 4 and 7 beam stacks have isolation frequencies slightly offset from frequencies in the 10 beam stack. Thus with more beams added more isolation frequencies are possible and wider and deeper band gaps can be achieved. Figure 5.10 also shows the benefits of using continuous vibration structures in vibration isolators instead of discreet springs and

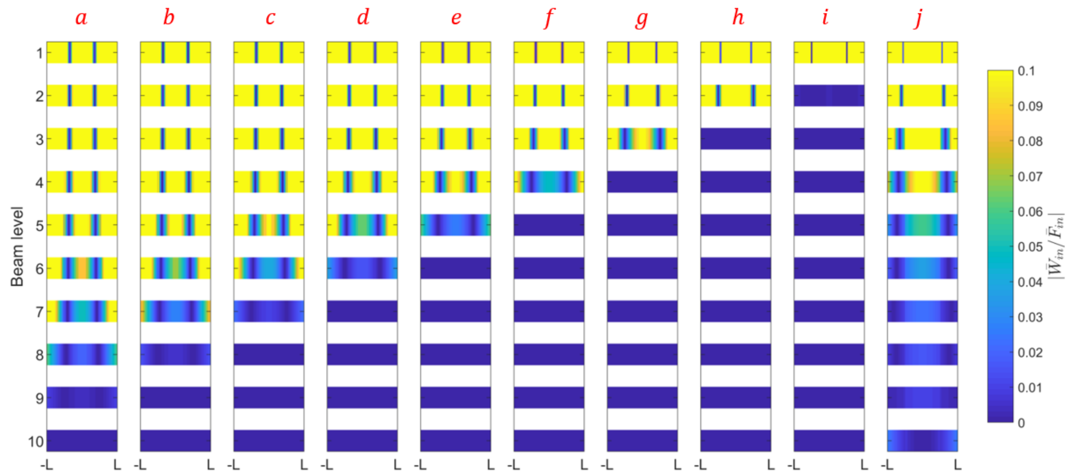

Figure 5.12. Color map showing the beam displacement distribution at the isolation frequencies in the first band gap (a-j in figure 5.10)

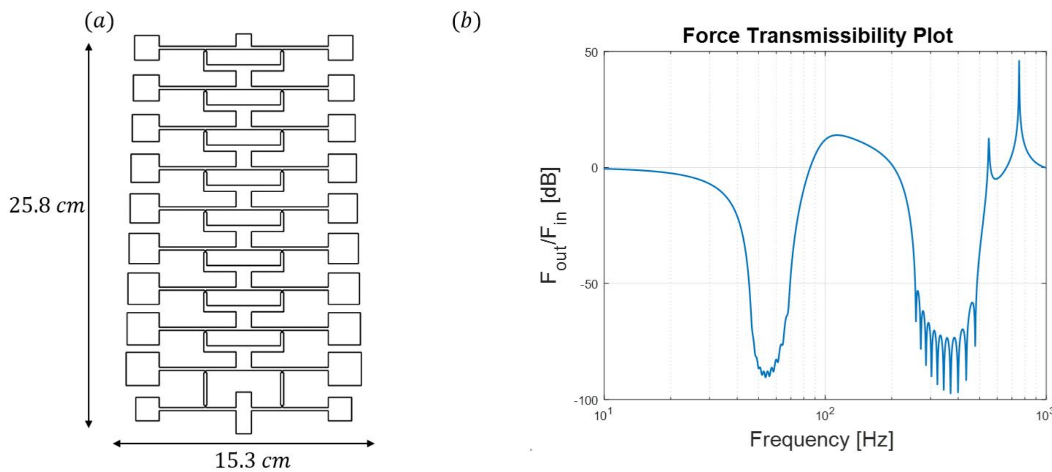

Figure 5.13. (a) Schematic of the dimensional model (b) dimensional frequency response of the 10 beam stack with damping such that the loss tangent $\tan\delta = 0.1$.

masses. Multiple band gaps can be observed in Figure 5.10. For a more realistic theoretical prediction the force transmissibility was also plotted with damping in Figure 5.11.

Figure 5.12 shows the displacement distribution for each beam at the isolation frequencies of the first band gap of the 10 beam stack. Vibration propagates through the stack from top to bottom and stops at the beam tuned to the excitation frequency. As frequency increases from left to right in Figure 5.12, the response is isolated in fewer beams. For case (i) for example, the top beam is tuned to the excitation frequency and the vibration propagates no further in the stack. In case (a) the 9th beam stops the vibration.

Figure 5.13-(a) shows the dimensions of the 10 beam design and Figure 5.13-(b) shows the frequency response for a frequency range of $\omega = 10$ to 1000 Hz. The first band gap is from 10 to 86 Hz. The second band gap is from 202 to 543 Hz, It is remarkable that this isolator provides force reduction over a region covering 42% of the 0-1 kHz domain.

Chapter 6

3D Printed Circular Nodal Plate Stacks for Broadband Vibration

This chapter shows that nodalization can be applied on axisymmetric thin plates, with no force/displacement transmissibility along a nodal radius. A monolithic compliant structure composed of multiple nodal plates connected in series is introduced and shown to be capable of generating multiple bandgaps, potentially at low frequencies. The monolithic isolator is fabricated using additive manufacturing, realizing complex structures with favorable dynamic characteristics. Additive manufactured isolators have three advantages. First, they do not require fluid that can be difficult to seal and sensitive to temperature variations. Second, 3D printed isolators can be tuned for specific bandgaps and frequencies, providing opportunities for customized designs. Finally, structural designs can be realized that would be difficult or impossible to manufacture with traditional methods. An analytical model predicts force transmissibility frequency response and is experimentally validated with several nodal plate designs. The model is used to design monolithic nodal plate isolators that achieve isolation performance equivalent to commercially available isolators with the same weight and volume.

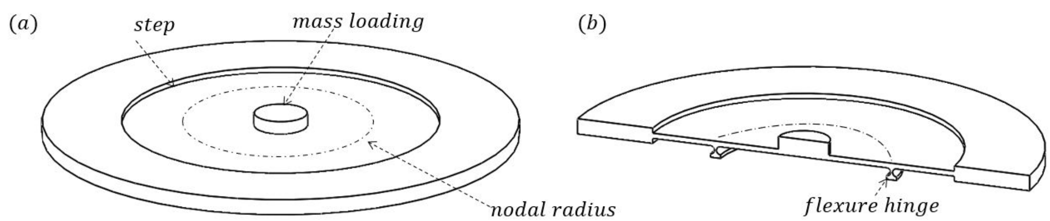

Figure 6.1. Mass loaded stepped plate (a) Isometric view (b) Cross sectional view with flexure hinge

6.1 Nodal Plate Network Design

Figure 6.1 shows an axisymmetric annular thin stepped plate loaded with a mass at its center. A transverse (vertical) force at the mass coupled with the axisymmetric structure and boundary conditions, produces axisymmetric transverse vibrations on the plate. The plate is mounted along a nodal radius through a flexure hinge such that there is zero transmission at the nodal circumference at a specific operational frequency. Figure 6.2 shows a nodal plate 2D schematic, where the flexure hinge is represented as a rotational spring. The plate parameters are the Young's modulus E, and density ρ. The mass M contained within radius r_1 and the nodal radius of the flexure hinge is r_2. The flexure rotational stiffness per circumferential length is K_r. The step radius is r_3, where the plate thickness changes from h_1 to h_2, the outer radius is r_{out}. The mass M is subject to a vertical force F_{in}. The plate can be tuned such that F_{out} is zero at a given operational frequency (or frequencies). The stepped plate design increases the design space with the r_3 and h_2 parameters.

Figure 6.3 shows a network of a nodal plates stacked in series. The stack is subject to an input force at the mass center on the top plate. Each plate connects to the mounting mass of the plate below through a circular flexure. The last plate is grounded at the nodal radius, with the output force transmitted through the flexure hinge. Each plate can be tuned to isolate at specific frequencies, so the stack can

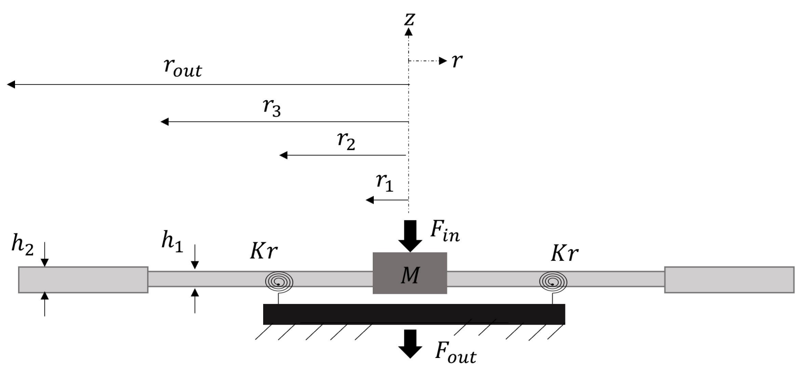

Figure 6.2. Schematic diagram of a single nodal plate with input force F_{in}, output force F_{out} and flexure hinges with torsional stiffness Kr.

isolate at multiple frequencies due to series plate connections. The frequencies can be tuned to be very close to each other to produce a large bandgap, or multiple bandgaps. The stack can provide force reduction over a large frequency range, or over multiple frequency ranges.

6.2 Analytical Model

The plate network shown in Figure 6.3 consists of n-plates, each plate with an outer radius $r_{out,i}$, where i indicates the plate level. The top for example, has input force F_{in}, $i = 1$, and the bottom plate has $i = n$. Each plate is loaded with a mass M_i with radius $r_{1,i}$. The flexure hinge connection at $r_{2,i}$ has a per-unit-length rotational stiffness Kr_i and an assumed rigid vertical connection. The circular flexure parameters are shown in Figure 6.4, and the rotational stiffness,

$$Kr_i = \frac{Ebt^3(2R+t)(4R+t)^3}{24R}\Bigg[t(4R+t)(6R^2+4Rt+t^2) + 6R(2R+t)^2\sqrt{t(4R+t)}\arctan\left(\sqrt{1+\frac{4R}{t}}\right)\Bigg]^{-1} \tag{6.1}$$

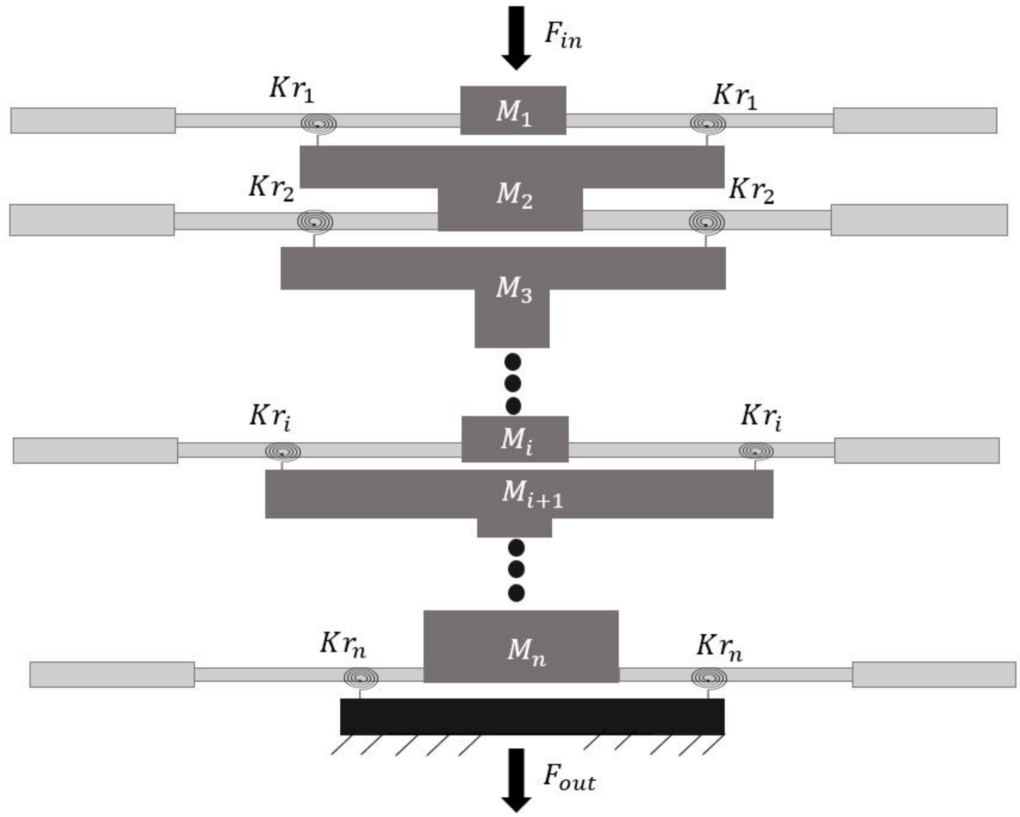

Figure 6.3. Schematic diagram of a stacked nodal plate isolator.

where R, flexure radius, and t, the flexure thickness, are the same for all flexures [99] . Each plate is stepped at a radius $r_{3,i}$.

The free transverse vibrations of a thin plate with viscoelastic damping can be described using the Kirchhoff-Love plate equation,

$$\frac{\partial^4 w_{i,j}}{\partial r_i^4} + \frac{2}{r_i}\frac{\partial^3 w_{i,j}}{\partial r_i^3} - \frac{1}{r_i^2}\frac{\partial^2 w_i}{\partial r_i^2} + \frac{1}{r_i^3}\frac{\partial w_i}{\partial r_i} + \frac{\rho h_{i,j}}{D_{i,j}}\frac{\partial^2 w_i}{\partial^2 t} = 0, \tag{6.2}$$

where $w_{i,j}(r_i, t)$ is the transverse displacement, $j = 1$ is from $r_{1,i}$ to $r_{2,i}$, $j = 2$ is from $r_{2,i}$ to $r_{3,i}$, and $j = 3$ is from $r_{3,i}$ to $r_{out,i}$, $h_{i,j}$ is the thickness of the plate, ρ is the material density, and D is the bending stiffness of the plate such that,

$$D_{i,j} = \frac{2h_{i,j}^3 E^*}{3(1 - v^2)}, \tag{6.3}$$

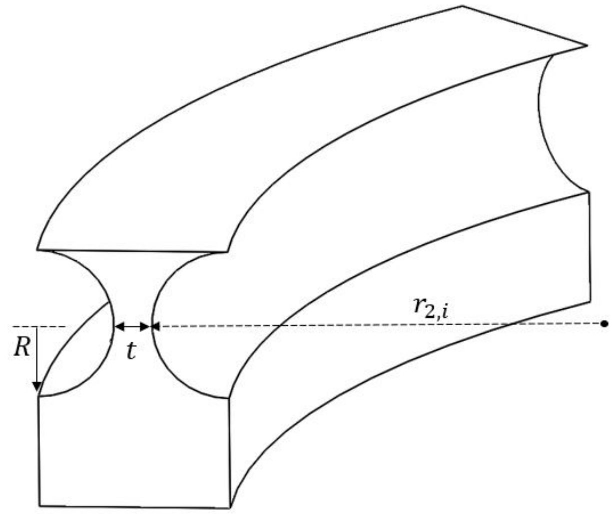

Figure 6.4. Schematic diagram of the i^{th} flexure hinge.

where E^* is the complex modulus, and,

$$E_{i,j}^* = E^{'} + j_{im}E^{''}, \tag{6.4}$$

E' is the storage modulus and E'' is the loss modulus, $j_{im} = \sqrt{-1}$. The complex Poisson's ratio v^* is assumed to be equal to the real Poisson's ratio v, based on [98]. Taking the Laplace transform of equation (6.2) in the time domain yields,

$$\frac{\partial^4 W_{i,j}}{\partial r_i^4} + \frac{2}{r_i}\frac{\partial^3 W_{i,j}}{\partial r_i^3} - \frac{1}{r_i^2}\frac{\partial^2 W_i}{\partial r_i^2} + \frac{1}{r_i^3}\frac{\partial W_i}{\partial r_i} + s^2 W_{i,j}\frac{\rho h_{i,j}}{D_{i,j}} = 0, \tag{6.5}$$

where s is the Laplace variable. The displacement transfer function,

$$G_{i,j}(r_i) = \frac{W_{i,j}(r_i, s)}{F_{in}(s)}, \tag{6.6}$$

Dividing equation (6.5) by F_{in}, and replacing s with $s = j_{im}\omega$, and ω is the excitation frequency, yields,

$$\frac{\partial^4 G_{i,j}}{\partial r_i^4} + \frac{2}{r_i}\frac{\partial^3 G_{i,j}}{\partial r_i^3} - \frac{1}{r_i^2}\frac{\partial^2 G_i}{\partial r_i^2} + \frac{1}{r_i^3}\frac{\partial G_i}{\partial r_i} - \beta_{i,j}^4 G_{i,j} = 0, \tag{6.7}$$

where $\beta_{i,j^4} = \frac{\omega^2 \rho h_{i,j}}{D_{i,j}}$. The solution to equation (6.7) is,

$$G_{i,j}(r_i) = A_{i,j} J_0(\beta_{i,j} r_i) + B_{i,j} Y_0(\beta_{i,j} r_i) + C_{i,j} I_0(\beta_{i,j} r_i) + N_{i,j} K_0(\beta_{i,j} r_i) \tag{6.8}$$

Where $A_{i,j}$, $B_{i,j}$, $C_{i,j}$, $N_{i,j}$ are unknown coefficients, J_0 and Y_0 are zero order Bessel function of the first and second kind, respectively. Y_0 and K_0 are zero order modified Bessel functions of the first and second kind, respectively. The per unit length inner moment transfer function,

$$\bar{T}_{,i,j} = -D_{i,j}\left[\frac{\partial^2 G}{\partial r^2} + \frac{v^*}{r_{i,j}}\frac{\partial G}{\partial r}\right] \tag{6.9}$$

and per unit length shear transfer function,

$$\bar{Q}_{,i,j} = -D_{i,j}\left[\frac{\partial^3 G}{\partial r^3} + \frac{1}{r_{i,j}}\frac{\partial^2 G}{\partial r^2} - \frac{1}{r_{i,j}^2}\frac{\partial G}{\partial r}\right] \tag{6.10}$$

The boundary conditions for equation (6.7) are periodic across the stack except for $i = 1$ where the input force is applied, and at $i = n$ where the output force is transmitted to the ground. At the inner radius $r_{i,1}$ the boundary conditions are as follows,

$$\left[\bar{Q}_{i,1}(\beta_{i,1}, r) - \frac{1}{2\pi r} - \frac{M_i \omega^2}{2\pi r} G_{i,1}(\beta_{i,1}, r)\right]_{r=r_{i,1}} = 0, \text{ for } i = 1, \tag{6.11}$$

$$\left[\bar{Q}_{i,1}(\beta_{i,1},r) - \frac{M_i\omega^2}{2\pi r}G_{i,1}(\beta_{i,1},r)\right]_{r=r_{i,1}} =$$

$$\frac{r_{i-1,2}}{r_{i,1}}\left[\bar{Q}_{i-1,1}(\beta_{i,1},r) - \bar{Q}_{i-1,1}(\beta_{i,2},r)\right]_{r=r_{i-1,2}} \text{ for } i = 2,..,n \quad (6.12)$$

$$\left[\ \frac{\partial G_{i,1}(\beta_{i,1},r)}{\partial r}\right]_{r=r_{i,1}} = 0, \text{ for } i = 1,..,n. \quad (6.13)$$

The continuity conditions at the nodal radius $r_{i,2}$ are,

$$[\ G_{i,1}(\beta_{i,1},r) = G_{i,2}(\beta_{i,2},r)]_{r=r_{i,2}}, \text{ for } i = 1,..,n \quad (6.14)$$

$$[\ G_{i,1}(\beta_{i,1},r)]_{r=r_{i,2}} = [G_{i+1,1}(\beta_{i+1,1},r)]_{r=r_{i+1,1}}, \text{ for } i = 1,..,n-1 \quad (6.15)$$

$$[\ G_{i,1}(\beta_{i,1},r)]_{r=r_{i,2}} = 0, \text{ for } i = n \quad (6.16)$$

$$\left[\ \frac{\partial G_{i,1}(\beta_{i,1},r)}{\partial r} = \frac{\partial G_{i,2}(\beta_{i,2},r)}{\partial r}\right]_{r=r_{i,2}}, \text{ for } i = 1,..,n \quad (6.17)$$

$$\left[\ \bar{T}_{i,2}(\beta_{i,2},r) = \bar{T}_{i,1}(\beta_{i,1},r) - Kr_i\frac{\partial G_{i,1}(\beta_{i,1},r)}{\partial r}\right]_{r=r_{i,2}}, \text{ for } i = 1,..,n. \quad (6.18)$$

Note here that equation (6.16) is the zero-displacement mounting condition at the bottom plate. The continuity conditions at the stepping radius $r_{i,3}$ are as follows,

$$[\ G_{i,2}(\beta_{i,2},r) = G_{i,3}(\beta_{i,3},r)]_{r=r_{i,3}}, \text{ for } i = 1,..,n \quad (6.19)$$

$$\left[\ \frac{\partial G_{i,2}(\beta_{i,2},r)}{\partial r} = \frac{\partial G_{i,3}(\beta_{i,3},r)}{\partial r}\right]_{r=r_{i,3}}, \text{ for } i = 1,..,n \quad (6.20)$$

$$\left[\ \bar{T}_{i,2}(\beta_{i,2},r) = \bar{T}_{i,3}(\beta_{i,3},r)\right]_{r=r_{i,3}}, \text{ for } i = 1,..,n \quad (6.21)$$

$$\left[\ \bar{Q}_{i,2}(\beta_{i,2},r) = \bar{Q}_{i,3}(\beta_{i,3},r)\right]_{r=r_{i,3}}, \text{ for } i = 1,..,n \quad (6.22)$$

The free end boundary conditions at $r_{out,i}$are expressed as,

$$\left[\ \bar{T}_{i,2}(\beta_{i,2}, r)\right]_{r=r_{out,i}} = 0,\ \text{for } i = 1, .., n \tag{6.23}$$

$$\left[\ \bar{Q}_{i,2}(\beta_{i,2}, r)\right]_{r=r_{out,i}} = 0,\ \text{for } i = 1, .., n \tag{6.24}$$

The parameters $A_{i,j}$ $B_{i,j}$ $C_{i,j}$, and $N_{i,j}$ can be determined by substituting equation (6.8) in the boundary conditions (6.11-6.24). A linear $12n \times 12n$ system of equations is obtained, which can be solved numerically by matrix inversion at each ω. The resulting solution is a system of transfer functions that describe the displacements across all the plates, the inner moment and shear can also be calculated by substituting (6.8) in (6.9) and (6.10), respectively. The output force,

$$F_{out} = 2\pi r_{n,2}\left[\ \bar{Q}_{n,2}(\beta_{i,2}, r) - \bar{Q}_{n,1}(\beta_{i,1}, r)\right]_{r=r_{n,2}} i = 1, .., n \tag{6.25}$$

Note that the analytical model presented in this case chapter is suitable for low amplitude vibrations, within the assumptions of Kirchhoff-Love theory for thin plates. High amplitudes vibrations are difficult to model mainly due to nonlinear behavior.

6.3 Experimental Validation

Three plate networks are designed and manufactured to demonstrate isolation performance and validate the analytical model. All the plates are 3D printed with Polylactic Acid (PLA) filament material using an Ender 3 V2 3D printer. All devices are printed at 100% infill density, with a raster angle of 45° C with 0.2 mm layer thickness, 100 mm/sec print speed, 200° C extrusion temperature and 60° C build plate temperature. Figure 6.7 shows the experimental setup for the

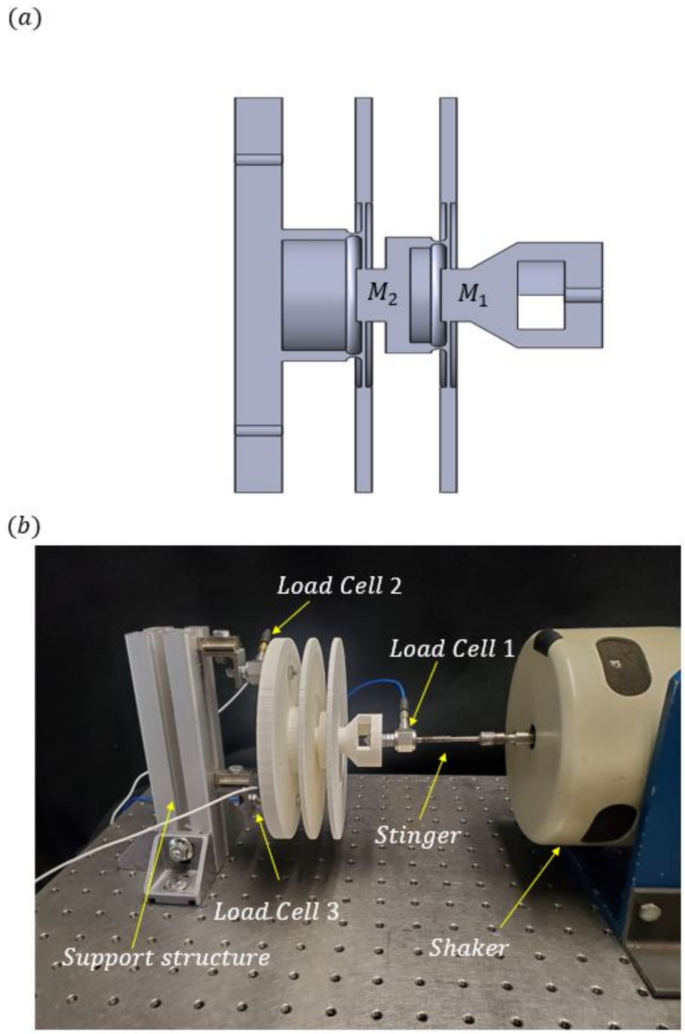

Figure 6.5. Two Plate Isolator 1: (a) Cross sectional view (b) Photograph and experimental setup.

experiments whereby a Ling LMT100 shaker stinger is connected to the first plate via a PCB 201C load cell which measures the input force induced by the shaker. The last plate is bolted to a support structure via two PCB201C load cells that measure the output force. The voltage signals from the load cells are transmitted to a PCB482-C series signal conditioner and recorded by an NI Data Acquisition device. The shaker is excited with a chirp signal input voltage with an amplitude of 0.4 volts. The time series force recordings are then transformed into the frequency

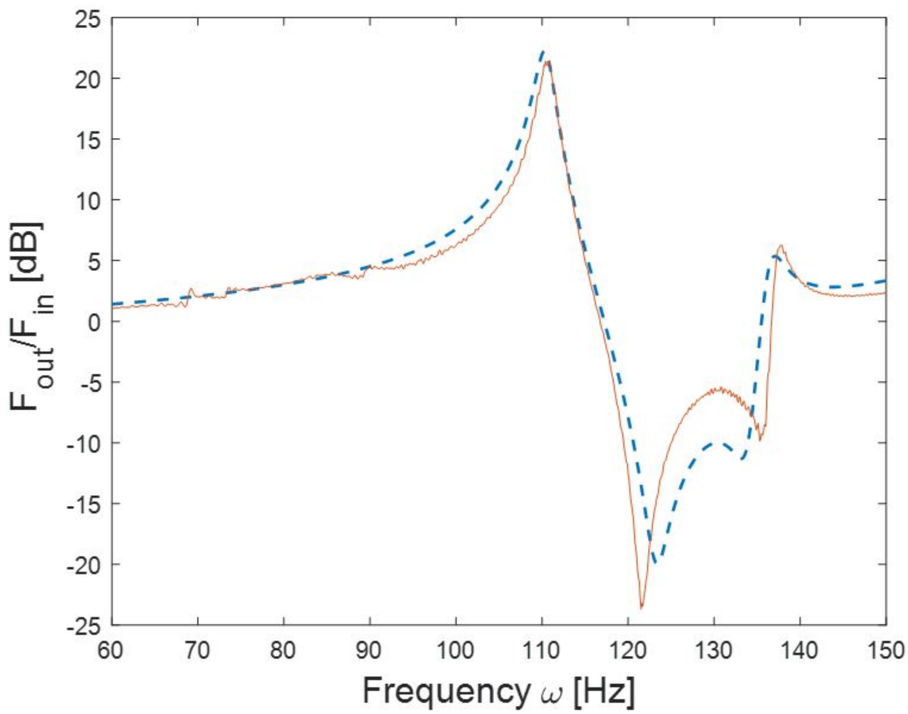

Figure 6.6. Force Transmission response of Isolator 1: analytical (dotted) and experiment (solid)

domain via a Fast Fourier transform algorithm, and the frequency response F_{out}/F_{in} is obtained. Note that there is no static preload condition in all experiments.

6.3.1 Two Plate Network

Figure 6.5 shows the two plate Isolator 1. Using a Young's modulus of $E = 2.7$Gpa , and density of 1190Kg/m^3, the geometric parameters are tuned to produce a wide and mid frequency bandgap around 120Hz, based on PLA specimens printed under similar conditions in [100]. The outer and inner radii and plate masses are shown in Table 6.1. The plate thicknesses are $h_{1i} = 0.001$ m and $h_{2i} = 0.00375$ m for both plates. The circular hinges for both plates are identical with $R = 0.00133$ m, a notch thickness $t = 0.00134$ m, and stiffness of 392 N/rd.

Figure 6.6 shows the analytical response and experimental force transmission

(a)

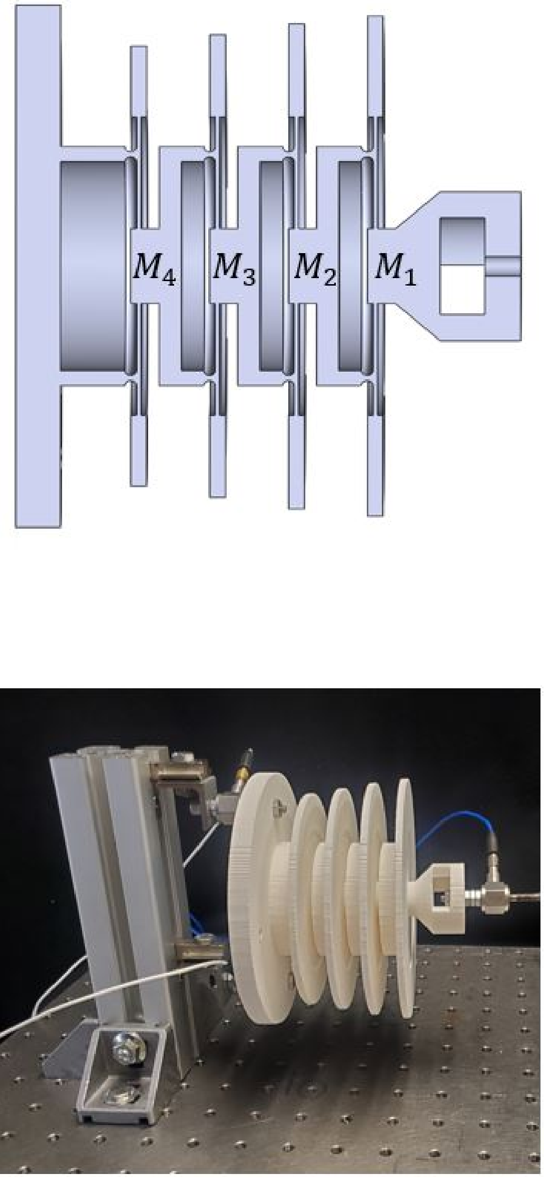

(b)

Figure 6.7. Four Plate Isolator 2: (a) Cross section view (b) Photograph and experimental setup

Table 6.1. Geometric and mass properties of isolator 1

Plate index	$r_{out,i}$	r_{1i}	r_{2i}	r_{3i}	M_i
1	0.075 m	0.01 m	0.0195 m	0.0345 m	0.0575 Kg
2	0.075 m	0.01 m	0.0215 m	0.0345 m	0.028 Kg

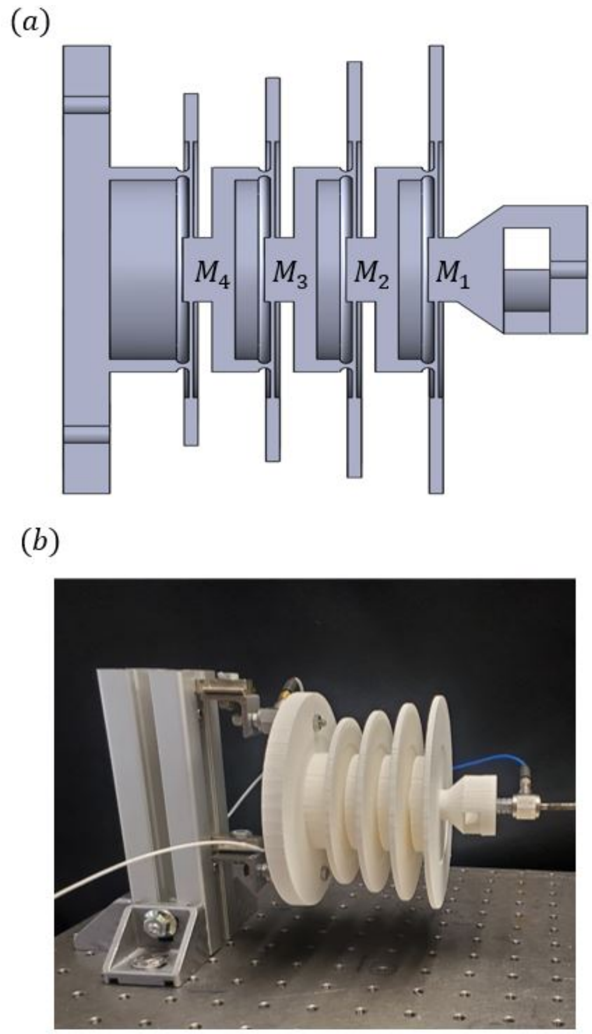

Figure 6.8. Four Plate Isolator 3: (a) Cross section view (b) Photograph and experimental setup

Table 6.2. Geometric and mass properties of isolator 2

Plate index	$r_{out,i}$	M_i
1	0.067 m	0.038 Kg/m
2	0.065 m	0.0412 Kg
3	0.062 m	0.0412 Kg
4	0.059 m	0.0412 Kg

frequency responses for the 2 plate system. The first 110 Hz and second 138 Hz experimentally measured natural frequencies match the model predictions to within 99.26%. The experimental bandgap, defined as the continuous frequency range with a force transmission < 1, stretches from 116.7 Hz to 136.5 Hz, within 93% of theoretical predictions. The first isolation frequency is shifted 2.4 Hz to the left of the theoretical prediction, the second isolation frequency is shifted by 1.5 Hz. The amplitude in the band gap seems to be higher between the two isolation frequencies in the experiment, this is caused by the shifts of the isolation frequencies in opposite directions. The left shift of the first frequency, and the right shift of the second frequency allow the response to increase over a wider frequency range. The small deviation from the theoretical prediction in the band gap is mainly caused by printing errors which would affect the thickness in the flexures, and in turn, the overall rotational stiffnesses. The stiffness changes have a pronounced effect on the band gap width.

6.3.2 Four Plate Networks

Isolators 2 and 3 shown in Figures 6.7 and 6.8 have four plates. The Young's modulus is assumed to be $E = 2.95$ Gpa, and the model parameters are tuned to provide a deep and wide bandgap around 250 Hz. The density is measured to be $\rho = 1050 Kg/m^3$. The damping loss factors are adjusted to fit the experimental results. For Isolator 2, the outer radii and plate masses are shown in Table 6.2, the inner radii and plate thicknesses are equal across all plate levels with $r_{1i} = 0.01$m, $r_{2i} = 0.03$m, $r_{3i} = 0.044$m, $h_{1i} = 0.0011$m, and $h_{2i} = 0.0032$m for $i = 1, .., n$. The flexure hinges are designed with a notch thickness $t = 0.00127m$, and a notch radius $R = 0.004$m such that the per unit length rotational stiffness is $Kr_i = 553$N/rd across all plate levels. The outer radii and masses for Isolator 2 are shown in Table

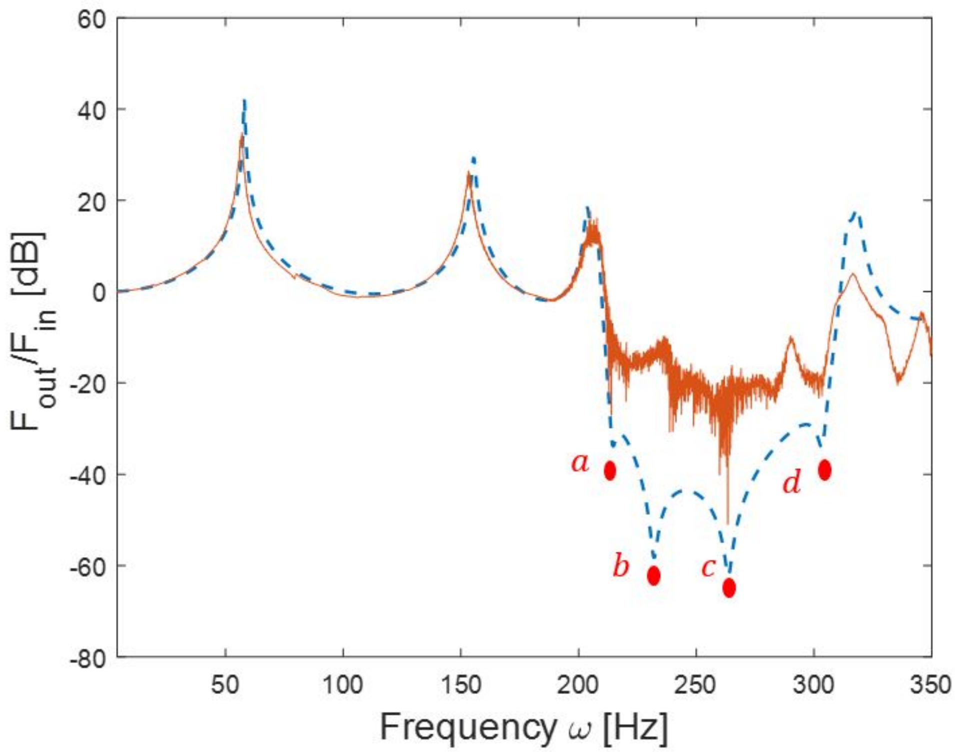

Figure 6.9. Force transmission response of Isolator 2: Analytical (dotted) and experiment (solid). The four points a-b-c-d indicate the isolation frequencies in the first bandgap.

Table 6.3. Geometric and mass properties of isolator 3

Plate index	$r_{out,i}$	M_i
1	0.072 m	0.0403 Kg
2	0.066 m	0.0281 Kg
3	0.06 m	0.0281 Kg
4	0.056 m	0.0281 Kg

6.3. The inner and outer radii and thicknesses for all plates with $r_{1i} = 0.01$m, $r_{2i} = 0.03$m, $r_{3i} = 0.04$m, $h_{1i} = 0.001$m and $h_{2i} = 0.003$m. The rotational hinge is the same as with $Kr_i = 553$N/rd for all plates.

Figures 6.9 and 6.10 shows the experimental and analytical response for Isolators 2 and 3, respectively. Both isolators have 4 natural frequencies that agree to within 98.7% of theory. Note that there are two natural frequencies in the region near 200

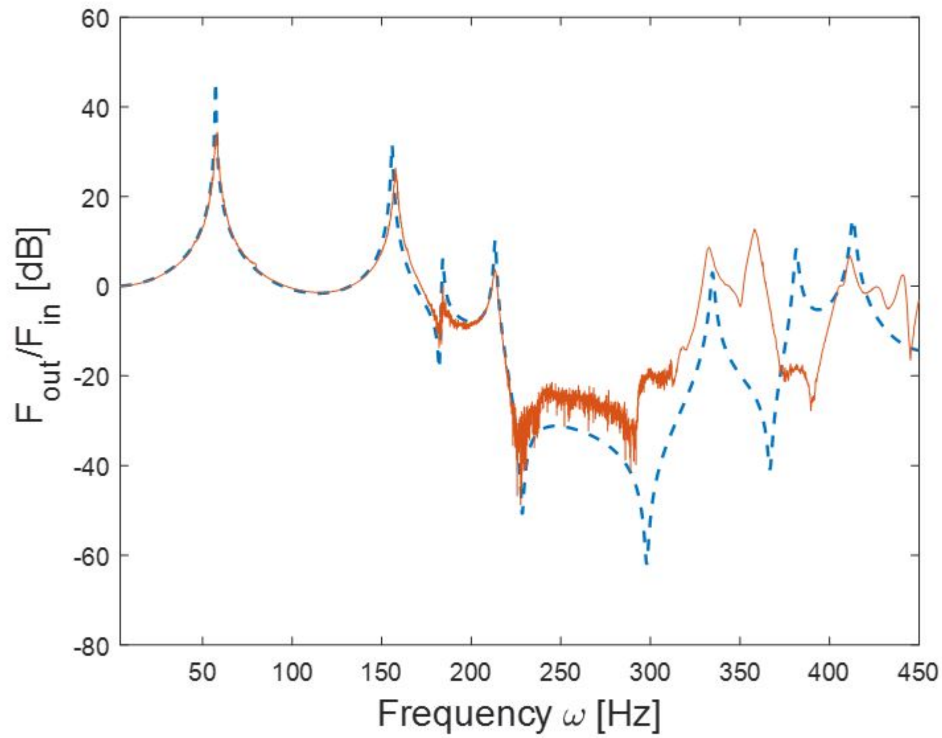

Figure 6.10. Frequency response of the analytical model of Isolator 3 (dotted) and the experiment (solid)

Hz, these two frequencies are very close to each other and the overall resonance peak at 200 Hz seems to be wide in the analytical model and the experiment. This is also the case for the two peaks near the 321 Hz region. For Isolator 2, the bandgap ranges from between 208 Hz and 310 Hz, matching the experimental bandgap. The predicted isolation frequencies highlighted with points a-b-c-d match the experimental isolation frequencies, where the response dips sharply. Torsional or twisting modes due to very small moment perturbations seem to penetrate the bandgap at 237 Hz and at 295 Hz. Figure 6.10 shows the transmission frequency of Isolator 3. Experimentally, the first band gap is between 172 Hz and 184 HZ, the model predicted 169 to 184 Hz. The second band gap range matches the experiment. The third band gap is most prominent, ranging from 215 Hz to 328 HZ, experimentally, the range is from 215 and 328 Hz. The fourth band gap is

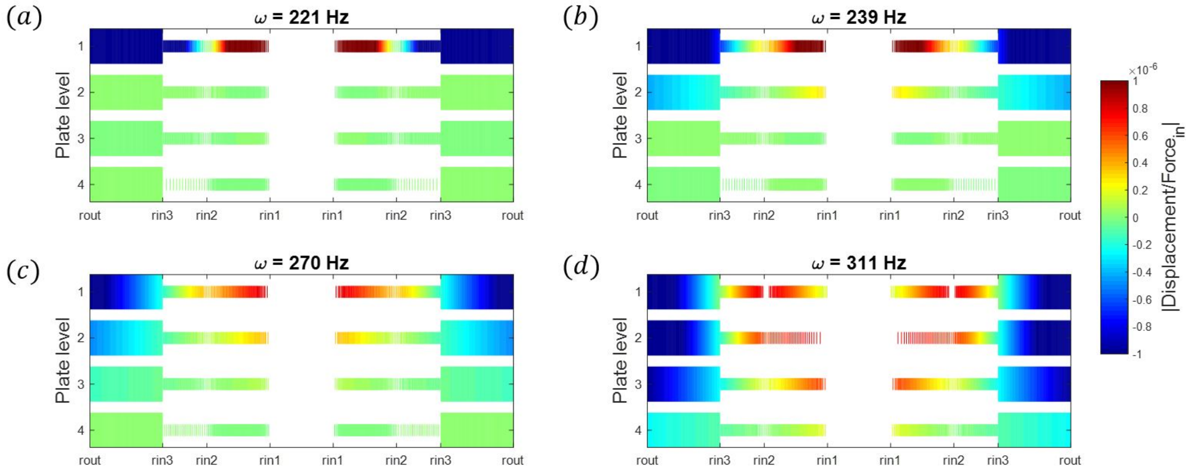

Figure 6.11. Colorplot showing the displacement of each plate in Isolator 2 at the four isolation frequencies labeled a-b-c-d in Figure 6.9

predicted from 333.5 Hz and 379.4 Hz, experimentally it is from 343 Hz and 352 Hz. The discrepancy in the fourth band gap is mainly due to mode coupling with twisting modes at high frequencies. Since the Network was experimentally made from PLA plastic, its overall material stiffness is low compared to conventional metals, and thus twisting modes are more easily excited at higher frequencies. This is also seen in the 292 to 313 Hz region, where the experiment slightly deviates from the predicted model, this is also caused by an unwanted mode coupling at high frequency. Additional experiments that show the repeatability of the force transmissibility experiments for Isolator 2 and 3 are shown in Appendix B.

Figure 6.11 is a color-plot showing the displacement propagation through Isolator 2 at the four bandgap isolation frequencies labeled a-b-c-d in Figure 6.9. The input is applied on the first plate, and the displacement travels down along the network. At ω = 221 Hz (a), there is no displacement on plates 2-3-4, so the first plate experiences zero transmission along its nodal radius, and therefore no vibrations propagate to the lower plates. At $\omega = 239Hz$ and $70Hz$ the vibration stops at the 2nd plate, and the 3rd plate, respectively. At ω = 311 Hz the vibration propagates all throughout the network, however the 4th plate hits its isolation frequency and there is no transmission along its nodal radius down to the ground.

6.3.3 Rotational and Torsional Modes

Discrepancy between the analytical model and the experiment is largely caused by rotational modes due to setup misalignments. Figure 6.12 shows the sum of forces measured by load cells 1 and 2, as well as the force difference normalized by the input force over the experimental frequency range. This is calculated by taking the magnitude of the FAST FOURIER TRANSFORM (FFT) of the difference of the measured forces in the load cells 1 and 2, and dividing that by the magnitude FFT of the input force,

$$\bar{\Delta_F} = \frac{|FFT(F_{LC1} - F_{LC2})|}{|FFT(F_{in})|} \tag{6.26}$$

where $\bar{\Delta_f}$ is the normalized force difference, F_{LC1} and F_{LC2} are the forces measured by the load cells 1 and 2, respectively. The normalized force summation is,

$$\bar{\Sigma_F} = \frac{|FFT(F_{LC1} + F_{LC2})|}{|FFT(F_{in})|} \tag{6.27}$$

The peak in load cell force difference at $\omega = 236$ Hz in Figure 6.12-(b), coupled with a small band-gap peak at the same frequency in the force summation plot in 6.12-(a), indicates an out-of-plane rotation mode or a torsional mode. There is a small peak in the force difference plot at 263 Hz that does not appear on the force summation plot. This indicates that there is an out of plane mode that is being excited at this frequency. There is a small band gap peak at $\omega = 290$ Hz that appears on the force summation plot but not on the force difference plot. This indicates this peak is caused by an in-plane rotational mode that leads to symmetric forces applied on the load cells.

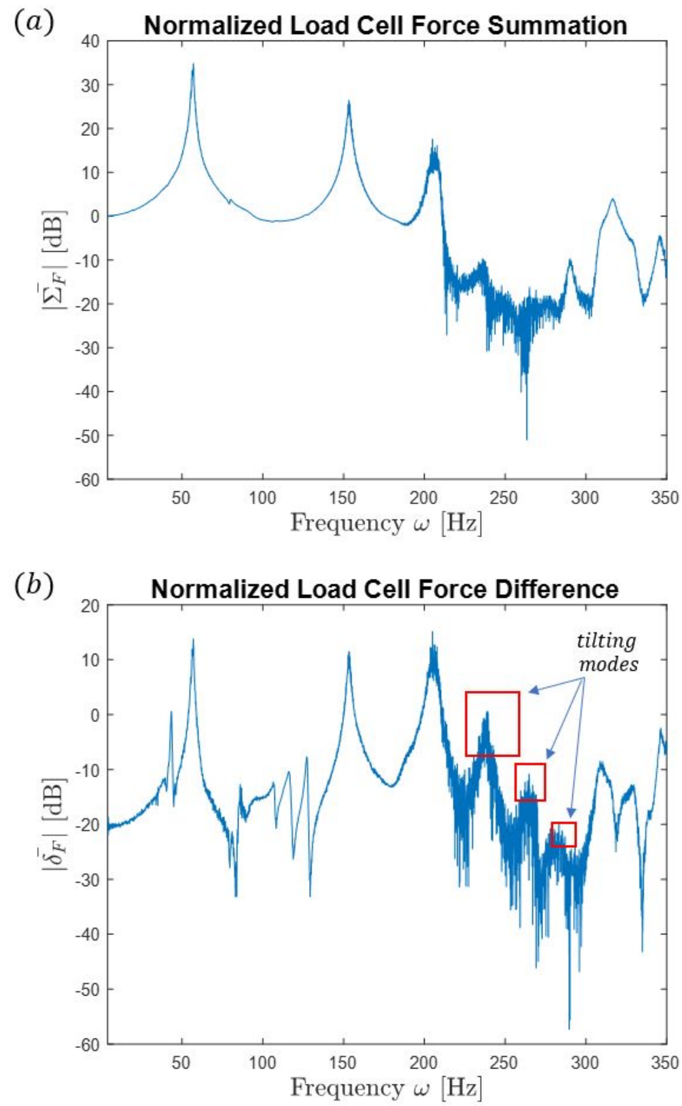

Figure 6.12. Graph showing the summation (a) and difference (b) of the forces measured by load cells 1 and 2, both normalized by the input force measured by load cell 1 shown in Figure 6.7.

6.3.4 Isolator Design

There are many parameters that affect the overall isolator behavior which make the design process tedious. The main challenge is to align the isolation and natural frequencies in the range of interest. Similar to the design process for beams, it is recommended to start with identical plates, with identical masses and rotational stiffnesses along the nodal radius. The target frequency range can be achieved by changing the parameters for a single plate. Plate thickness for example seemed to have a large effect on isolation/natural frequency. Thereafter, a single parameter for each plate can be changed to move their respective isolation frequencies and obtain a band gap. Changing the mass seemed to very effective, also changing the outer radius seemed to be effective as well, especially if the outer plate is thicker than the inner plate. Changing the rotational stiffness is also effective for band gap tunability.

6.4 Response Sensitivity to Manufacturing Errors

The proposed plate stack isolators are monolithic and manufacturable using additive manufacturing technology. Using flexures instead of hinges reduces friction and wearing losses that increase the maintenance cost and reduce the overall lifetime of the isolator. These devices are susceptible to printing errors where the thickness distribution can vary during the 3D printing process up to +/- 0.2mm, depending on the accuracy of the printer [100, 112]. Nonuniform cooling speeds for layers with different sizes cause warping and thickness variations. A sensitivity study is conducted to assess the effects of print errors on the frequency response. The critical thicknesses in the isolator are the plate thickness and the flexure notch thicknesses. Figure 6.13 shows the response variation of the two plate Isolator 1 as each of these thicknesses vary from -0.2 mm to +0.2 mm. The right shifts in the graphs (a)-(d) shows that the addition of thickness adds more stiffness. As shown in Figure 6.13-(a) the response is very sensitive to the inner plate thickness h_1. The sensitivity to the outer plate thickness h_2 shown in Figure 6.13-(b) is not as pronounced as h_1, but has the same trend and causes the rightward bandgap shift in Figure 6.13-(b). The increase in rotational stiffness on the first plate Kr_1 mainly

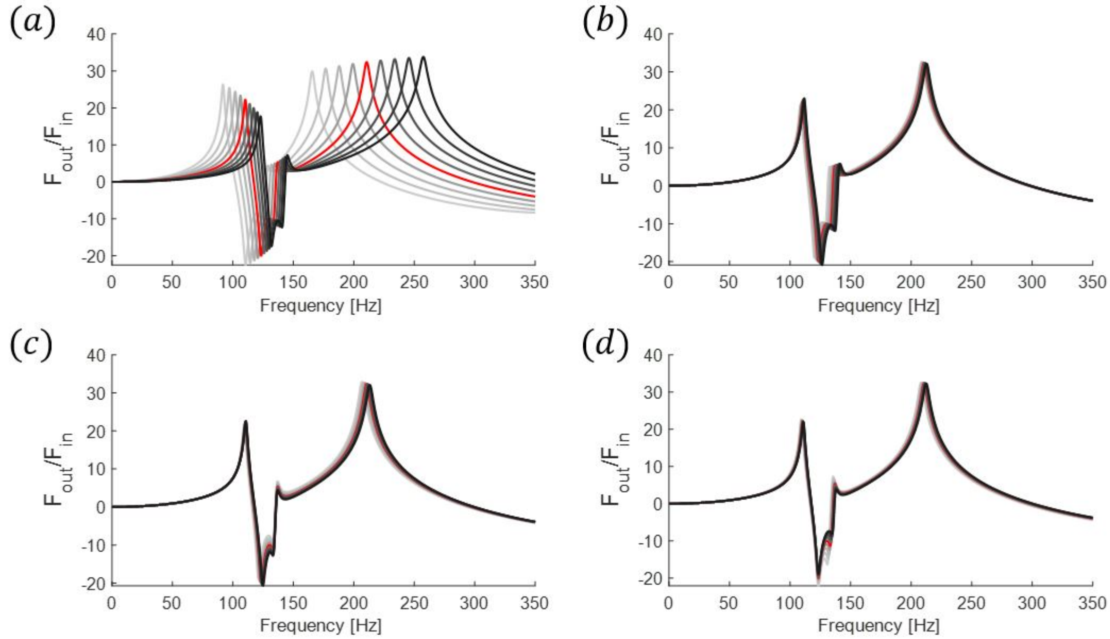

Figure 6.13. Transmission frequency response sensitivity to printing errors for (a) plate thickness h_1, (b) plate thickness h_2 and the flexure notch thicknesses presented as variations in the flexure notch stiffnesses (c) Kr_1 and (b) Kr_2 with thicknesses ranging from -15% (light gray) to +15% (black) and the color red resembling a 0% error.

shifts the first isolation frequency and the third natural frequency to the right, as seen in 6.13-(c). The same shift is observed for the second isolation frequency and the second natural frequency with the increase in the rotational stiffness of the second plate Kr_2 in Figure 6.13-(d). The shifting of isolation frequencies in the bandgap leads to an increase of transmission amplitude between the two frequencies, making the bandgap shallower. This shows that the main cause for the discrepancy between the experiment and the model for Isolator 1 in Figure 6.6 is a printing error in the rotational hinges that leads to frequency shifting. Therefore, when designing plate network isolators, it is important to account for geometric tolerances in the thin features to minimize the response sensitivity. This problem can be overcome by using more accurate printers, or more accurate printing methods such as Stereolithography (SLA) or Polyjet.

6.4.1 Printing Orientation

All plate isolators used in the experiments above were printed by having them laid flat along their side. This orientation ensures that there will be no support structures in the inner plate masses. Supports on the inner structure cannot be removed because the masses are fully encircled by the rotational hinge, and these supports will attach to the preceding plate thus hindering any inner plate displacement. By printing the plate with their side, the overhang angle will always be small except in the early stages in the print, which will lead to a structure with minimal supports. The main draw back with side printing orientation is that the fiber orientation in the thing flexures might not be uniform, which could lead to a variable stiffness along the radius. By printing with 100% infill density, this effect could minimize.

6.5 Low Frequency Isolation with Metal Based Plate Networks

Plate networks made from metal could be very suitable for real life applications. The high fatigue capability of metals combined with their high stiffness makes metals a good design choice for plate networks. Their high stiffness will make them less sensitive to twisting or off-axis loading. Furthermore, metal-based plate networks can be realized by metal additive technology, specifically, Laser Powder Bed Fusion (LPBF). To assess their dynamic performance, a large pool of randomly generated parameter sets is fed into the analytical model. Each set is a plate network design made up of 4 plates. Titanium is chosen as the material for all design sets since it is commonly used in applications, and because it has good fatigue

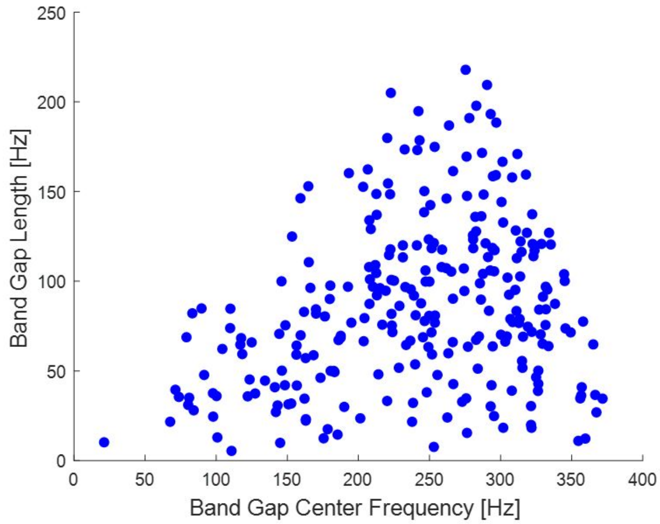

Figure 6.14. Monte Carlo plot showing the bandgap characteristics width vs. center for 4 plate isolators within a design space associated with commercially available isolators.

and stiffness characteristics. The model is constrained such that the maximum outer diameters is 30 cm, making dimensions comparable to commercially available isolators [113, 114], and printable with commercially available LPBF printers. The Young's modulus for titanium is $E = 140$ Gpa and the density is chosen to $\rho = 4400$ Kg/m^3. The minimum thickness constraint is chosen to be 0.6 mm to meet the design guidelines for minimum wall thickness for LPBF printing [115]. Therefore, the minimum values for h_{1i}, h_{2i}, and the flexure notch thickness are 0.6mm. The rotational hinge is chosen to have a width of 4 mm, associated with $Kr_i = 1814$ N/rd. The maximum stiffness is $Kr_i = 20,000$ N/rd, and the inner masses M_i are chosen to range from 0.08 Kg to 0.28 Kg. Figure 6.14 is a Monte Carlo plot showing the first bandgap width and center of the metal plate networks within this design space. The bandgap width reduces for lower bandgap centers. Isolation at lower frequencies is much more difficult that at high frequencies. The model predicts that metal plate networks are capable of achieving low frequency broadband isolation (<80 Hz).

Chapter 7

Conclusions and Future Work

7.1 Conclusions

In this dissertation elastic network vibration isolators are presented. Elastic networks with beam and plate elements are investigated with different stacking conditions.

Theoretical models verified with experiments show that parallel-stacked beam network isolators are a good fit for HSLDS applications, even for those with relatively high deflection characteristics. Furthermore, parallel stacking introduces new features such as multi-frequency isolation, high stiffness, and isolation frequency clustering. The versatility of the beam network isolator is due to the ability to tune beam components in the design level to match a certain isolation criterion. Using the concept of parallel stacking, a modified DAVI with a flexible lever is introduced. The flexibility of the lever with elastic boundary conditions allows for a more accurate dynamic model as compared to the rigid lever assumption and the friction-less connection assumption in the classic DAVI. Moreover, the lever elasticity with a distributed inertial profile has an additional inertial amplification effect, leading to an improved isolation performance as the inertial forces are much higher as compared to a rigid lever. It is shown that a flexible DAVI is capable of isolation at lower frequencies as compared to a rigid DAVI with the same auxiliary mass. The flexible DAVI is also suitable for HSLDS, low frequency isolation applications. These isolators can achieve low frequency isolation; without trading off stiffness and at a reduced mass-penalty, compared to classic DAVI. It is also worth noting that these isolators do not exhibit any nonlinear isolation behavior, such as jump phenomenon or displacement dependencies. This work shows that the ability to manufacture complex structures due to the advance of additive manufacturing can lead to the development of vibration control devices with favorable dynamic characteristics and a potential for relatively long fatigue lives. The fact that these isolators are monolithic means that the main failure modes are stress related, in the absence of friction. With a proper design scheme, these isolators can be designed to have an overall low stress limit, given a certain geometry and a set of specifications.

Using parallel stacking, a compact fluid free beam network isolator is designed. The isolator has a diameter of 23 cm, a height of 21 cm and a total mass of 8 Kg. The isolator exhibits HSLDS behavior and is capable of providing a large degree of isolation at low frequency (25 Hz). Decoupling the static and dynamic displacements allows for a large static displacement without affecting the overall dynamic performance. This design shows the versatility of beam network isolators whereby the stiffness as well as the isolating force can be scaled. The added compliance of the beams and the hinges allow for less isolator volume and mass compared to typical DAVI designs. Finally, a rubber-beam network isolator is built as a proof of concept and used to experimentally verify the analytical model for rubber-beam network isolators.

The concept of series stacking beam networks is explored, and it is shown that nodal beam stack isolators consisting of multiple nodal beams connected in series, generate multiple, wide, and deep band gaps. An isolator with four beams is designed to provide a band gap of 32 Hz with a center frequency at 72 Hz. A polymer prototype is 3D printed and the frequency response of input force to transmitted force is experimentally measured showing a large 41 Hz band gap with a center frequency also around 72 Hz. The experimentally validated model is used to design a 10 beam isolator with a low frequency band gap from 10 to 86 Hz and a high frequency band gap from 202 to 543 Hz, resulting in a force reduction encompassing 42% of the 0-1KHz domain. The monolithic nature of these isolators means they can be additively manufactured and the flexure hinge design reduces friction and wear with the absence of sliding surfaces.

Novel plate vibration isolators are presented and shown to generate multiple bandgaps over several frequency ranges. The analytical model is verified with 3 experiments to a high degree of accuracy. The model shows that small thickness variations can alter the bandgap width, center, and range. However, with more accurate printers, as well as a detailed tolerance analysis, this could be overcome, and the isolators will not deviate from their target design performance. The experimentally validated model predicts that metal-based plate stack isolators manufactured with Laser Powder Bed Fusion can achieve broadband isolation at low frequency (< 80 Hz). Monolithic plate stack isolators, now possible with the advance of additive manufacturing, are advantageous over commercially available isolators due to their customizable, single-part nature that eliminates friction and increases cycle life.

In summary, this dissertation showed that the elastic networks can be used to design isolators with one or more of the following features:

- Low frequency isolation

- Compact and fluid-free designs
- HSLDS behavior
- No nonlinear isolator behavior
- Large broad band gap isolation
- Friction-less design
- Manufacturable with additive manufacturing

7.2 Future Work

There are many possible future directions for this research. There are two main recommendations for future work that can be done to build on the research provided in this dissertation, namely, stress analysis, a design optimizer tool, elastomeric isolator manufacturing, metal-based isolators, and multidirectional vibration isolators.

7.2.1 Stress Analysis and Design Optimizer

Vibration or cyclic loading of isolators is the main factor that will determine their respective lifetimes. Isolators are subject to a static loading as well, which increase the overall stresses in the isolator components. Therefore, it is very important to conduct a comprehensive stress analysis for the monolithic isolators presented in this thesis:

- The flexible lever DAVI
- The nodal beam isolator
- The nodal plate isolator

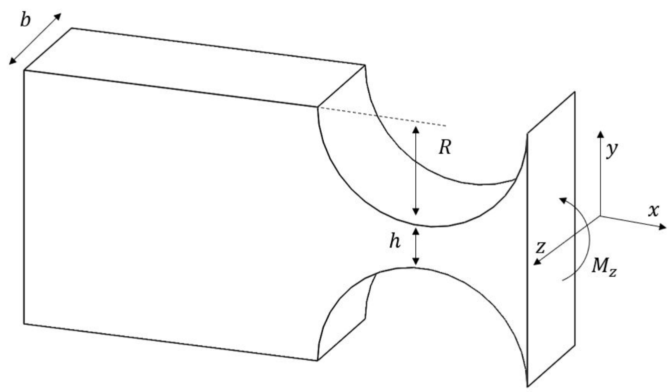

Figure 7.1. Schematic showing a flexure hinge subject to a bending moment M_z

The rotational flexure hinges will be a major weak point for these isolators, especially due to stress concentrations on the flexure notch thin parts. Some stress concentration equations can be found in [16]. The maximum bending stress in a circular flexure hinge is calculated as [116],

$$\sigma^b_{max} = k_b \sigma_{nom} \tag{7.1}$$

where nominal maximum stress due to bending σ_{nom} can be calculated as,

$$\sigma_{nom} = \frac{6M_z}{bh^2} \tag{7.2}$$

Where M_z is the bending moment, w is the flexure hinge, and h is the flexure minimum thickness, as shown in Figure 7.1. The stress concentration factor k_b is approximated as [117, 118],

$$k_b = (1 + \frac{h}{2R})^{9/20} \text{ for } 0 < \frac{h}{2R} < 2.3 \tag{7.3}$$

For more accurate stress predictions, the axial stress should also be considered.

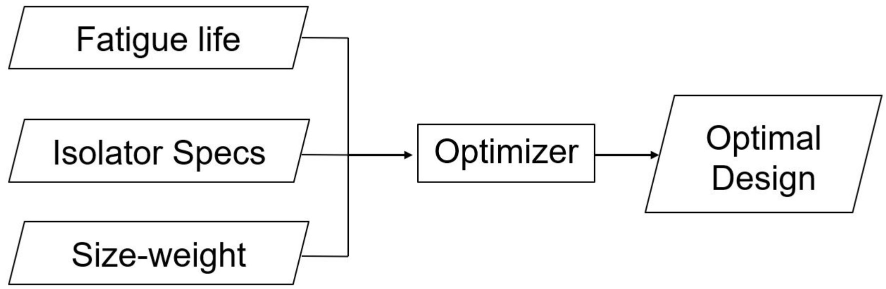

Figure 7.2. Isolator design optimizer flowchart that meets a given set of isolator specifications within limitations on stress, fatigue, size, and weight

The maximum axial stress can be calculated as [116],

$$\sigma^b_{max} = k_a \sigma_{nom} \tag{7.4}$$

where k_a is the axial stress concentration, and the nominal axial stress is calculated as,

$$\sigma^a_{nom} = \frac{F_x}{bh} \tag{7.5}$$

In the case of loading in both the axial and bending directions the following stress concentration factors can be used [119],

$$k_a = -0.1729\left(\frac{R}{h}\right)^3 + 0.8539\left(\frac{R}{h}\right)^2 - 1.4265\left(\frac{R}{h}\right) + 1.9613 \tag{7.6}$$

$$k_b = 0.1721\left(\frac{R}{h}\right)^4 - 0.9288\left(\frac{R}{h}\right)^3 + 1.8387\left(\frac{R}{h}\right)^2 + 1.9613 - 1.6593\left(\frac{R}{h}\right) + 1.669 \tag{7.7}$$

Given the nominal stresses due to bending and axial loading, the overall equivalent stress can be calculated using superposition. More accurate ways to calculate the equivalent stress, as well as suitable fatigue strength limits can be found in [120,121].

The stress and fatigue tool can be used to find the maximum weight limit for each design. This is important for practical design applications. Therefore, given certain isolator specs a design optimizer can be built to find an optimal design within constraints on stress, fatigue, size, and weight. Figure 7.3 shows am optimizer flow chart, the isolator specifications can be calculated using the analytical models presented in this dissertation. The stress and fatigue limits can be calculated using the methodology outlined above. After building the stress tools, the optimizer can be built. Given the large number of parameters and constraints, a genetic optimization scheme is recommended. For example, a Nondominated sorting generic algorithm (also known as NSGA) can be used.

7.2.2 Preload conditions and Linear Load Limits

Most isolators are subject static loads, mainly because they are part of a load path where a vibratory/isolated mass is mounted on them. This thesis assumes that the preloading conditions do not affect the vibration response since linearity is assumed. However, for continuous systems, large displacements might lead to nonlinear effects. It is recommended that preloading conditions should be thoroughly explored to find a maximum static load/ preload before the system becomes nonlinear.

The models presented in this thesis are well equipped for low amplitude vibrations which is often the case for many isolator applications. However, it is recommended to explore the linear limits of the model, or the load at which the isolator behavior becomes nonlinear. This could be very helpful to assign a maximum loading specification that is coupled with stress limits.

7.2.3 Metal Elastic Networks

Fatigue is one the main failure modes for vibration isolators, mainly due to the cyclic loading under various environmental conditions. Metals isolators are of particular interest due to their capability to endure high fatigue loads. The monolithic nature of additively manufactured networks already eliminates friction and wearing losses. Therefore, the first step is experimenting with metal additively manufactured networks to demonstrate their favorable dynamic performance, and to validate the model that includes isotropic and homogeneous assumptions.

Laser powder bed fusion is a suitable metal additive manufacturing method that might work well for the isolators presented in this dissertation. Some major considerations would be to ensure proper print orientations not to prevent powder entrapment in the hollow chambers in nodal plate networks. Care should also be taken to ensure proper minimum thickness in the flexure hinges, as well as the thin plate/beam members.

7.2.4 Off-axis loading

The elastic networks presented are suitable for unidirectional vibration applications, especially beam networks. Beam networks are not designed to withstand titling loads and will thus be very sensitive to off-balance disturbances. Plates on the other hand are less sensitive to off-balance loads, that is due to the high plate torsional/tilting stiffness. Nonetheless rotational modes do appear on the experimental frequency response plots. Therefore, it is recommended to explore experimental methods that reduce rotational and torsional mode excitations. Furthermore, it is recommended to explore designs or isolator systems that are generally less sensitive to off-axis loading.

7.2.4.1 Experimental Methods for Reduced Rotational Mode Excitation

Shaker stinger alignment with the isolator load path is often difficult to achieve without a small degree of error. Even small misalignments can lead to rotational

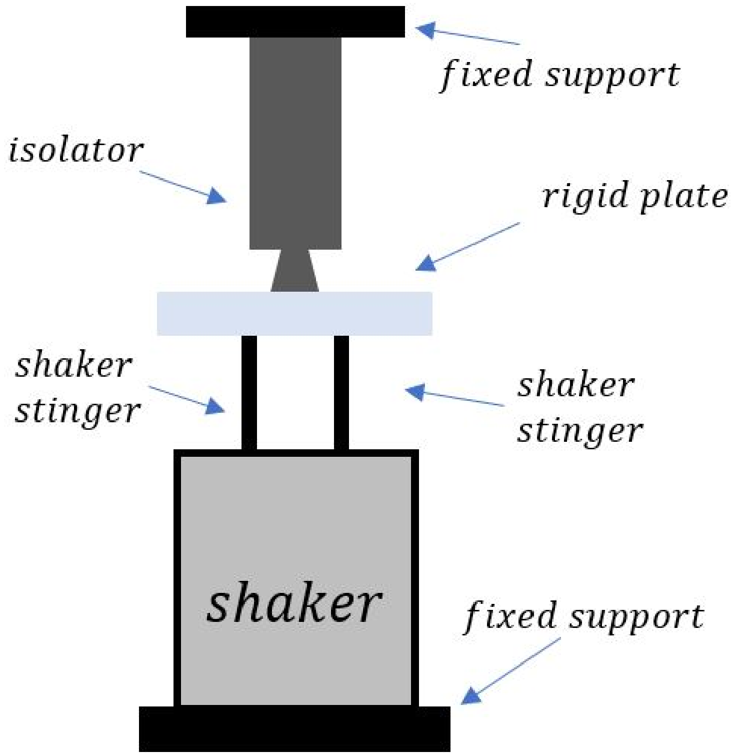

Figure 7.3. Schematic of a vertical experimental setup with a rigid plate

modes that might penetrate a target bandgap. Therefore, it is recommended to setup an experiment with a rigid plate connection between the stinger and the isolator as shown in Figure 7.4. Verticals experimental setups are recommended to ensure that the weight of the isolator does not lead to misalignment. The rigid plate can easily be leveled statically, and is held by multiple shaker stingers, which will prevent tilting motion.

7.2.4.2 System of Unidirectional Isolators

Figure 7.4 shows a strut system for gearbox vibration attenuation. A similar concept can be explored whereby these struts could be unidirectional isolator units hinged and free to rotate at both ends (or on the support structure end only).

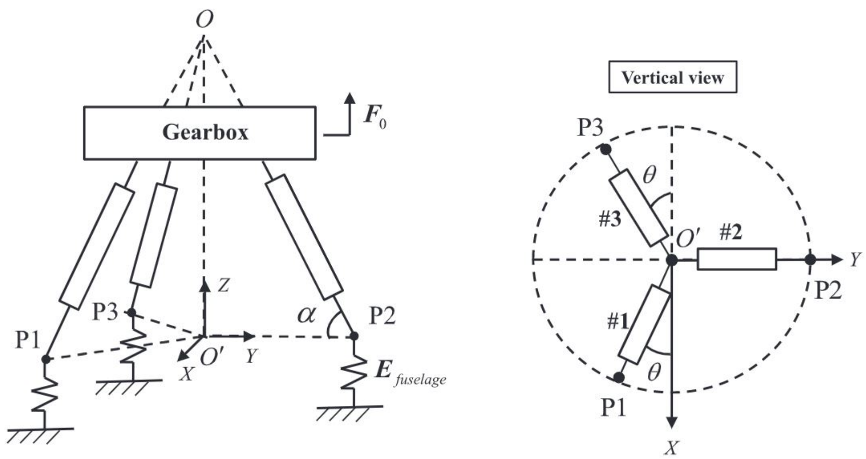

Figure 7.4. Gearbox Strut System [16]

This way each isolator will behave as a two-force member, and the overall system behavior will not be sensitive to any off-axis loading.

7.2.4.3 Design Solutions for Increasing Rotational and Torsional Stiffness

Force adaptors can be used to make sure that the load path does not deviate from the load path direction (more information about tilting adaptors and overall practical isolator design features are found in Appendix C). This can be done by designing adaptors with for a very high tilting stiffness. This way the rotational modes will only appear at very high frequency.

Appendix A

Force Transmissibility Derivation for a Flexible Lever DAVI

Figure A.1 shows the left half free body diagram of a flexible lever DAVI. The flexible DAVI is subject to an input force F_{in} at the mounted mass. The displacement of the mounted mass M_t is denoted by Y. The spring force is F_s, the force transferred to the beam is F_b. Therefore, the equation for $F_{in}/2$ is

$$F_{in}(t)/2 = F_b(t) + F_s(t) + M_t\ddot{Y}_t(t). \tag{A.1}$$

The force transferred from the beam to the ground is denoted by F_g. Therefore, the output force equation is,

$$F_{out}(t)/2 = F_g(t) + F_s(t). \tag{A.2}$$

The force transmissibility ratio in the frequency domain is then,

$$T_{flex} = \frac{F_g(\omega) + F_s(\omega)}{F_b(\omega) + F_s(t) - \omega^2 M_t Y_t(\omega)} \tag{A.3}$$

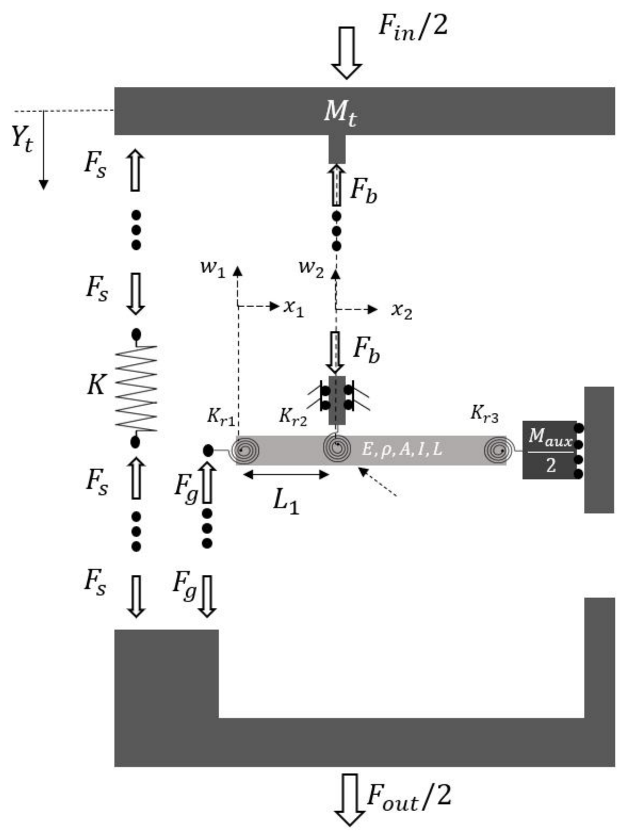

Figure A.1. Free body diagram of a flexible DAVI.

Dividing the numerator and the denominator by F_b, and replacing $F_s = KY_t$ equation (A.3) becomes,

$$T_{flex} = \frac{F_g/F_b + KY_t/F_b}{1 + KY_t/F_b - \omega^2 M_t Y_t/F_b} \tag{A.4}$$

The transfer functions $G_2(0, \omega) = -Y_t/F_b$ and $G_1'''(0, \omega) = -F_g/F_b$ can be calculated using the beam transfer function method presented in this dissertation. Therefore, the force transmissibility ratio becomes,

$$T_{flex}(\omega) = \frac{-KG_2(0, \omega) + EIG_1'''(0, \omega)}{-KG_2(0, \omega) + 1 + \omega^2 M_t G_2(0, \omega)}, \tag{A.5}$$

Appendix B

Additional Experiments

B.1 Repeatability

This appendix includes additional experiments that are a repetition of experiments previously presented in different parts of this dissertation. The experiments are presented for the purpose of showing repeatability of results. The figures below are additional experiments for the four beam isolator in Chapter 5, the plate isolators referred to as isolators 1 and 2 in Chapter 6.

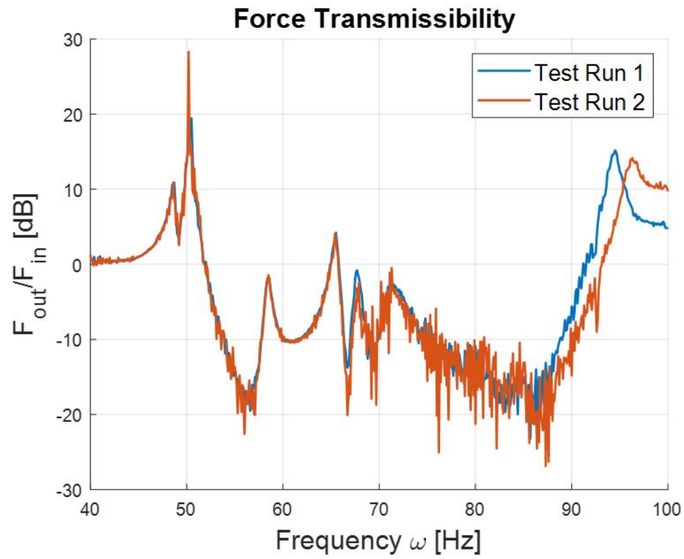

Figure B.1. Force transmissibility plots for the four-beam isolator presented in Chapter 5 whereby this experiment is comparable to that shown in Figure 5.6.

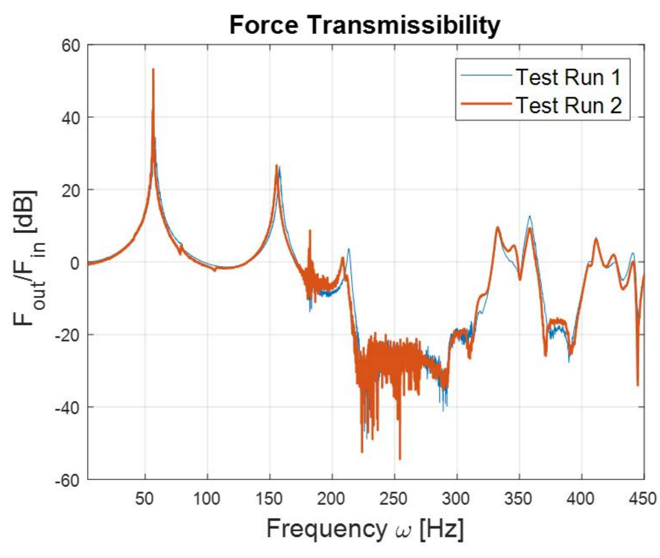

Figure B.2. Force transmissibility plots for the four-plate isolator presented in Chapter 6 bas Isolator 2 whereby this experiment is comparable to the one shown in Figure 6.9.

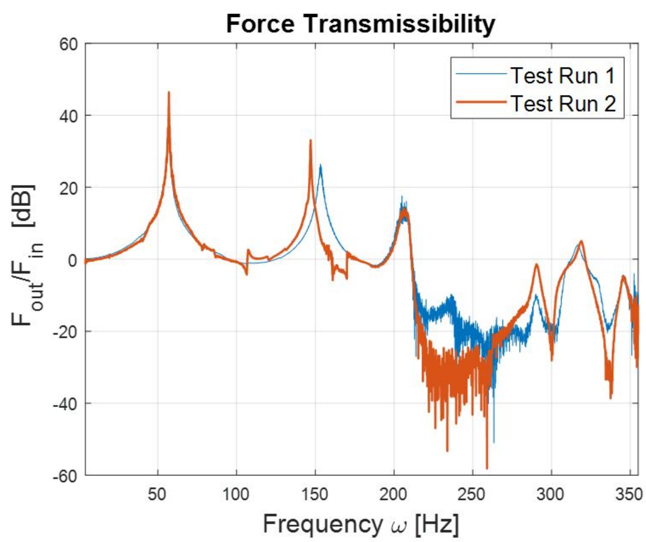

Figure B.3. Force transmissibility plots for the four-plate isolator presented in Chapter 6 as Isolator 3 whereby this experiment is comparable to the one shown in Figure 6.10.

Appendix C

Practical Isolator Design

C.1 Tilting Stiffness Adaptor

Chapters 5 and 6 in this dissertation included an analysis into rotational modes that appear in the experimental responses of nodal beam and plate isolators. These rotational modes are often caused by off-axis loading coming from shaker misalignment in the experimental setup. Misalignments and off-axis loads are very difficult to avoid in real life applications, therefore typical isolator designs include methods to maintain alignment in the isolator load path by adding high tilting stiffness features. For example, Figure C.1 shows a cross section of a Fluidlastic isolator (with no fluid) with a rubber adapter at its top end. The rubber adapter is very stiff in the tilting direction, which ensures alignment in the load path.

C.2 Casing

Isolators are sensitive to mass changes and damages, even on the small scale. For the isolators presented above it is recommended to have a casing design to protect the inner isolator mechanism from buildup of gunk, and possible solid particle

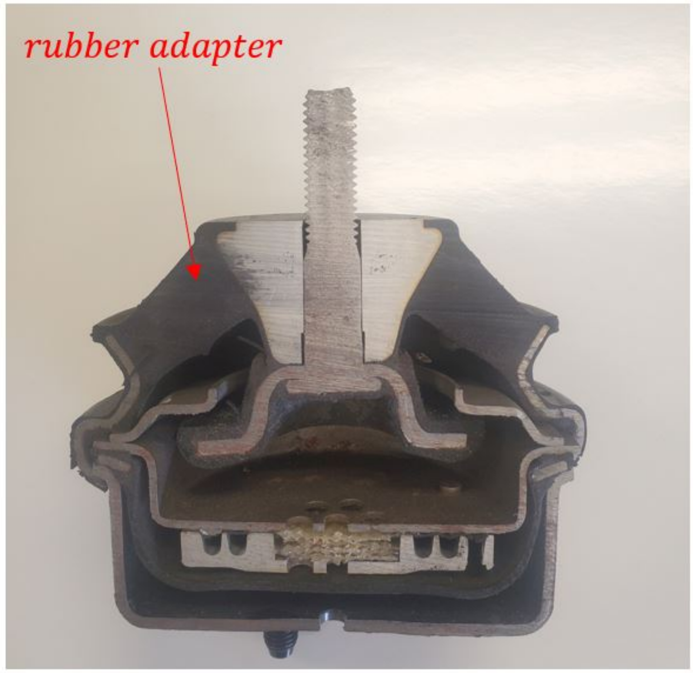

Figure C.1. Force transmissibility plot for the four-plate isolator presented in Chapter 6 bas Isolator 2 whereby this experiment is comparable to the one shown in Figure 6.9.

strikes that might damage the mechanism. The casing feature is common for most isolators, especially for fluidic isolators (see Figuere C.1) that are very sensitive to leaking, or to solid particles.

Bibliography

[1] Crede, C. E. and J. E. Ruzicka (1996) "Theory of vibration isolation," *Shock and vibration handbook*, **2**, pp. 30–35.

[2] Özyar, O. and Ç. Yilmaz (2021) "A self-tuning adaptive-passive lever-type vibration isolation system," *Journal of Sound and Vibration*, **505**, p. 116159.

[3] Kuhnert, W. M., P. J. P. Gonçalves, D. F. Ledezma-Ramirez, and M. J. Brennan (2021) "Inerter-like devices used for vibration isolation: a historical perspective," *Journal of the Franklin Institute*, **358**(1), pp. 1070–1086.

[4] Halwes, D. (1980) "LIVE–liquid inertia vibration eliminator," in *American Helicopter Society 36th Annual Forum, Washington, DC*.

[5] Domke, B. (2000).
URL `https://b-domke.de/AviationImages/Rotorhead/1264.html`

[6] McGuire, D. P. (1994) "Fluidlastic dampers and isolators for vibration control in helicopters," in *ANNUAL FORUM PROCEEDINGS-AMERICAN HELICOPTER SOCIETY*, vol. 5, AMERICAN HELICOPTER SOCIETY, pp. 295–295.

[7] Tamer, A., V. Muscarello, G. Quaranta, and P. Masarati (2020) "Cabin layout optimization for vibration hazard reduction in helicopter emergency medical service," *Aerospace*, **7**(5), p. 59.

[8] Huang, X., X. Liu, and H. Hua (2014) "On the characteristics of an ultra-low frequency nonlinear isolator using sliding beam as negative stiffness," *Journal of Mechanical Science and Technology*, **28**(3), pp. 813–822.

[9] Ibrahim, R. (2008) "Recent advances in nonlinear passive vibration isolators," *Journal of sound and vibration*, **314**(3-5), pp. 371–452.

[10] Alabuzhev, P. (1989) *Vibration protection and measuring systems with quasi-zero stiffness*, CRC Press.

[11] Yu, L., L. Tang, L. Xiong, and T. Yang (2020) "Capture of high energy orbit of Duffing oscillator with time-varying parameters," *Chaos: An Interdisciplinary Journal of Nonlinear Science*, **30**(2), p. 023106.

[12] Matlack, K. H., A. Bauhofer, S. Krödel, A. Palermo, and C. Daraio (2016) "Composite 3D-printed metastructures for low-frequency and broadband vibration absorption," *Proceedings of the National Academy of Sciences*, **113**(30), pp. 8386–8390.

[13] Hu, G., A. C. Austin, V. Sorokin, and L. Tang (2021) "Metamaterial beam with graded local resonators for broadband vibration suppression," *Mechanical Systems and Signal Processing*, **146**, p. 106982.

[14] Yilmaz, C., G. M. Hulbert, and N. Kikuchi (2007) "Phononic band gaps induced by inertial amplification in periodic media," *Physical Review B*, **76**(5), p. 054309.

[15] Reichert, G. (1980) "Helicopter vibration control-a survey," in *Sixth European Rotorcraft and Powered Lift Aircraft Forum*.

[16] Wang, J. and X. Liu (2014) "Generalized equations for estimating stress concentration factors of various notch flexure hinges," *Journal of Mechanical Design*, **136**(3).

[17] Snowdon, J. C. (1968) *Vibration and shock in damped mechanical systems*, J. Wiley.

[18] Crede, C. E. (1951) *Vibration and shock isolation*, Wiley.

[19] Snowdon, J. C. (1979) "Vibration isolation: use and characterization," *The Journal of the Acoustical Society of America*, **66**(5), pp. 1245–1274.

[20] Flannelly, W. G. (1967), "Dynamic antiresonant vibration isolator," US Patent 3,322,379.

[21] Rita, A., J. McGarvey, and R. Jones (1978) "Helicopter rotor isolation evaluation utilizing the dynamic antiresonant vibration isolator," *Journal of the American Helicopter Society*, **23**(1), pp. 22–29.

[22] Braun, D. (1982) "Development of antiresonance force isolators for helicopter vibration reduction," *Journal of the American Helicopter Society*, **27**(4), pp. 37–44.

[23] Desjardins, R. A. and W. Hooper (1980) "Antiresonant rotor isolation for vibration reduction," *Journal of the American Helicopter Society*, **25**(3), pp. 46–55.

[24] Braun, D. (1988), "Vibration isolator particularly of the antiresonance force type," US Patent 4,781,363.

[25] Desjardins, R. A. and V. Sankewitsch (1982) "Vibration isolation system," *The Journal of the Acoustical Society of America*, **72**(6), pp. 2053–2053.

[26] Desjardins, R. A., C. W. Ellis, and V. Sankewitsch (1983) "Vibration isolation system," *The Journal of the Acoustical Society of America*, **73**(1), pp. 395–395.

[27] Liu, N., C. Li, C. Yin, X. Dong, and H. Hua (2018) "Application of a dynamic antiresonant vibration isolator to minimize the vibration transmission in underwater vehicles," *Journal of Vibration and Control*, **24**(17), pp. 3819–3829.

[28] Ivovich, V. and M. Savovich (2001) "Isolation of floor machines by lever-type inertial vibration corrector," *Proceedings of the Institution of Civil Engineers-Structures and Buildings*, **146**(4), pp. 391–402.

[29] Liu, C., X. Jing, and F. Li (2015) "Vibration isolation using a hybrid lever-type isolation system with an X-shape supporting structure," *International Journal of Mechanical Sciences*, **98**, pp. 169–177.

[30] Yilmaz, C. and N. Kikuchi (2006) "Analysis and design of passive band-stop filter-type vibration isolators for low-frequency applications," *Journal of Sound and Vibration*, **291**(3-5), pp. 1004–1028.

[31] Kim, G. W. and J. Kang (2019) "The V-shaped band-stop vibration isolator inspired by middle ear," *Applied Acoustics*, **150**, pp. 162–168.

[32] Yan, B., Z. Wang, H. Ma, H. Bao, K. Wang, and C. Wu (2021) "A novel lever-type vibration isolator with eddy current damping," *Journal of Sound and Vibration*, **494**, p. 115862.

[33] Yan, B., N. Yu, Z. Wang, C. Wu, S. Wang, and W. Zhang (2022) "Lever-type quasi-zero stiffness vibration isolator with magnetic spring," *Journal of Sound and Vibration*, **527**, p. 116865.

[34] Rivin, E. I. (2003) *Passive vibration isolation*, Amer Society of Mechanical.

[35] Goodwin, A. J. (1965), "Vibration isolators," US Patent 3,202,388.

[36] Rasmussen, R. E. (1964), "Engine mount," US Patent 3,137,466.

[37] Halwes, D. R. and W. A. Simmons (1980), "Vibration suppression system," US Patent 4,236,607.

[38] Flower, W. C. (1985) "Understanding hydraulic mounts for improved vehicle noise, vibration and ride qualities," *SAE transactions*, pp. 832–841.

[39] Corcoran, P. E. and G.-H. Ticks (1984) "Hydraulic engine mount characteristics," *SAE transactions*, pp. 25–30.

[40] Scarborough, L. H., C. D. Rahn, and E. C. Smith (2012) "Fluidic composite tunable vibration isolators," *Journal of vibration and acoustics*, **134**(1).

[41] Miura, K., M. Krott, E. Smith, C. D. Rahn, and P. Romano (2015) "Experimental validation of Tailboom vibration control using fluidic flexible matrix composite tubes," in *Annual Forum Proceedings-AHS International*, vol. 2, American Helicopter Society, pp. 1252–1260.

[42] Krott, M. J. (2018) *Fluidic Flexible Matrix Composite Vibration Treatments for Helicopter Airframes and Rotor Blades*, The Pennsylvania State University.

[43] Smith, M. R. and W. S. Redinger (1999) "The model 427 pylon isolation system," in *AHS International Annual Forum, 55 th, Montreal, Canada*, pp. 195–201.

[44] McGuire, D. P. (2003) "High stiffness (" rigid") helicopter pylon vibration isolation systems," in *ANNUAL FORUM PROCEEDINGS-AMERICAN HELICOPTER SOCIETY*, vol. 59, AMERICAN HELICOPTER SOCIETY, INC, pp. 649–658.

[45] Han, D., C. D. Rahn, and E. C. Smith (2014) "Higher harmonic pitch link loads reduction using fluidlastic isolators," *Proceedings of the Institution of Mechanical Engineers, Part G: Journal of Aerospace Engineering*, **228**(3), pp. 455–469.

[46] Ibrahim, R. and R. Somnay (2007) "Nonlinear dynamic analysis of an elastic beam isolator sliding on frictional supports," *Journal of Sound and Vibration*, **308**(3-5), pp. 735–757.

[47] Liu, C. and K. Yu (2018) "A high-static–low-dynamic-stiffness vibration isolator with the auxiliary system," *Nonlinear Dynamics*, **94**(3), pp. 1549–1567.

[48] Liu, X., X. Huang, and H. Hua (2013) "On the characteristics of a quasi-zero stiffness isolator using Euler buckled beam as negative stiffness corrector," *Journal of Sound and Vibration*, **332**(14), pp. 3359–3376.

[49] Oyelade, A. O. (2019) "Vibration isolation using a bar and an Euler beam as negative stiffness for vehicle seat comfort," *Advances in Mechanical Engineering*, **11**(7), p. 1687814019860983.

[50] Lu, Z.-Q., D.-H. Gu, H. Ding, W. Lacarbonara, and L.-Q. Chen (2020) "Nonlinear vibration isolation via a circular ring," *Mechanical Systems and Signal Processing*, **136**, p. 106490.

[51] Somnay, R. J., R. Ibrahim, and R. Banasik (2006) "Nonlinear dynamics of a sliding beam on two supports and its efficacy as a non-traditional isolator," *Journal of Vibration and Control*, **12**(7), pp. 685–712.

[52] Sun, X. and X. Jing (2016) "A nonlinear vibration isolator achieving high-static-low-dynamic stiffness and tunable anti-resonance frequency band," *Mechanical systems and signal processing*, **80**, pp. 166–188.

[53] Jiang, G., X. Jing, and Y. Guo (2020) "A novel bio-inspired multi-joint anti-vibration structure and its nonlinear HSLDS properties," *Mechanical Systems and Signal Processing*, **138**, p. 106552.

[54] Carrella, A., M. Brennan, and T. Waters (2007) "Static analysis of a passive vibration isolator with quasi-zero-stiffness characteristic," *Journal of sound and vibration*, **301**(3-5), pp. 678–689.

[55] Carrella, A., M. Brennan, I. Kovacic, and T. Waters (2009) "On the force transmissibility of a vibration isolator with quasi-zero-stiffness," *Journal of Sound and Vibration*, **322**(4-5), pp. 707–717.

[56] Carrella, A., M. Friswell, A. Zotov, D. Ewins, and A. Tichonov (2009) "Using nonlinear springs to reduce the whirling of a rotating shaft," *Mechanical Systems and Signal Processing*, **23**(7), pp. 2228–2235.

[57] Carrella, A., M. Brennan, T. Waters, and V. Lopes Jr (2012) "Force and displacement transmissibility of a nonlinear isolator with high-static-low-dynamic-stiffness," *International Journal of Mechanical Sciences*, **55**(1), pp. 22–29.

[58] Balaji, P. and K. Karthik SelvaKumar (2021) "Applications of nonlinearity in passive vibration control: a review," *Journal of Vibration Engineering & Technologies*, **9**(2), pp. 183–213.

[59] Richards, D. and D. J. Pines (2003) "Passive reduction of gear mesh vibration using a periodic drive shaft," *Journal of Sound and Vibration*, **264**(2), pp. 317–342.

[60] Elmadih, W., D. Chronopoulos, W. Syam, I. Maskery, H. Meng, and R. Leach (2019) "Three-dimensional resonating metamaterials for low-frequency vibration attenuation," *Scientific reports*, **9**(1), pp. 1–8.

[61] Jiang, S., H. Chen, L. Dai, H. Hu, and V. Laude (2017) "Multiple low-frequency broad band gaps generated by a phononic crystal of periodic circular cavity sandwich plates," *Composite Structures*, **176**, pp. 294–303.

[62] Sorokin, V. (2013) "A new approach to the analysis of oscillations of one-dimensional spatially periodic structures," *Journal of Sound and Vibration*, **332**(14), pp. 3552–3563.

[63] Liu, Z., X. Zhang, Y. Mao, Y. Zhu, Z. Yang, C. T. Chan, and P. Sheng (2000) "Locally resonant sonic materials," *science*, **289**(5485), pp. 1734–1736.

[64] Jin, Y., X.-Y. Jia, Q.-Q. Wu, X. He, G.-C. Yu, L.-Z. Wu, and B. Luo (2022) "Design of vibration isolators by using the Bragg scattering and local resonance band gaps in a layered honeycomb meta-structure," *Journal of Sound and Vibration*, **521**, p. 116721.

[65] Krushynska, A. O., M. Miniaci, F. Bosia, and N. M. Pugno (2017) "Coupling local resonance with Bragg band gaps in single-phase mechanical metamaterials," *Extreme Mechanics Letters*, **12**, pp. 30–36.

[66] Xiao, Y., J. Wen, G. Wang, and X. Wen (2013) "Theoretical and experimental study of locally resonant and Bragg band gaps in flexural beams carrying periodic arrays of beam-like resonators," *Journal of Vibration and Acoustics*, **135**(4).

[67] Nobrega, E., F. Gautier, A. Pelat, and J. Dos Santos (2016) "Vibration band gaps for elastic metamaterial rods using wave finite element method," *Mechanical Systems and Signal Processing*, **79**, pp. 192–202.

[68] Wang, K., J. Zhou, Q. Wang, H. Ouyang, and D. Xu (2019) "Low-frequency band gaps in a metamaterial rod by negative-stiffness mechanisms: Design and experimental validation," *Applied Physics Letters*, **114**(25), p. 251902.

[69] Wu, Z., W. Liu, F. Li, and C. Zhang (2019) "Band-gap property of a novel elastic metamaterial beam with X-shaped local resonators," *Mechanical Systems and Signal Processing*, **134**, p. 106357.

[70] Sun, H., X. Du, and P. F. Pai (2010) "Theory of metamaterial beams for broadband vibration absorption," *Journal of Intelligent Material Systems and Structures*, **21**(11), pp. 1085–1101.

[71] Lu, Z.-Q., L. Zhao, H. Ding, and L.-Q. Chen (2021) "A dual-functional metamaterial for integrated vibration isolation and energy harvesting," *Journal of Sound and Vibration*, p. 116251.

[72] El-Borgi, S., R. Fernandes, P. Rajendran, R. Yazbeck, J. Boyd, and D. Lagoudas (2020) "Multiple bandgap formation in a locally resonant linear

metamaterial beam: Theory and experiments," *Journal of Sound and Vibration*, **488**, p. 115647.

[73] Salleh, H. and M. Brennan (2007) "Control of flexural waves on a beam using a vibration neutraliser: Effects of different attachment configurations," *Journal of sound and vibration*, **303**(3-5), pp. 501–514.

[74] Gao, Y., M. J. Brennan, and F. Sui (2011) "Control of flexural waves on a beam using distributed vibration neutralisers," *Journal of Sound and Vibration*, **330**(12), pp. 2758–2771.

[75] du Toit, D., B. Mace, V. Sorokin, and L. Rughunanan (2021) "Control of bending wave transmission through an uncoupled force and moment neutraliser," *Journal of Sound and Vibration*, **508**, p. 116219.

[76] Liu, C., X. Jing, and Z. Chen (2016) "Band stop vibration suppression using a passive X-shape structured lever-type isolation system," *Mechanical systems and signal processing*, **68**, pp. 342–353.

[77] Goffaux, C. and J. Sánchez-Dehesa (2003) "Two-dimensional phononic crystals studied using a variational method: Application to lattices of locally resonant materials," *Physical review B*, **67**(14), p. 144301.

[78] Szefi, J., E. Smith, and G. Lesieutre (2003) "Design and analysis of high-frequency periodically layered isolators for helicopter gearbox isolation," in *44th AIAA/ASME/ASCE/AHS/ASC Structures, Structural Dynamics, and Materials Conference*, p. 1784.

[79] Frandsen, N. M., O. R. Bilal, J. S. Jensen, and M. I. Hussein (2016) "Inertial amplification of continuous structures: Large band gaps from small masses," *Journal of Applied Physics*, **119**(12), p. 124902.

[80] Li, Y. and W. Zhou (2021) "Bandgap and vibration transfer characteristics of scissor-like periodic metamaterials," *Journal of Applied Physics*, **130**(2), p. 025103.

[81] Miranda Jr, E., E. Nobrega, A. Ferreira, and J. Dos Santos (2019) "Flexural wave band gaps in a multi-resonator elastic metamaterial plate using Kirchhoff-Love theory," *Mechanical Systems and Signal Processing*, **116**, pp. 480–504.

[82] Zouari, S., J. Brocail, and J.-M. Génevaux (2018) "Flexural wave band gaps in metamaterial plates: A numerical and experimental study from infinite to finite models," *Journal of Sound and Vibration*, **435**, pp. 246–263.

[83] Xiao, Y., J. Wen, and X. Wen (2012) "Flexural wave band gaps in locally resonant thin plates with periodically attached spring–mass resonators," *Journal of Physics D: Applied Physics*, **45**(19), p. 195401.

[84] Zang, J., T.-C. Yuan, Z.-Q. Lu, Y.-W. Zhang, H. Ding, and L.-Q. Chen (2018) "A lever-type nonlinear energy sink," *Journal of Sound and Vibration*, **437**, pp. 119–134.

[85] Liu, C., D. Xu, and J. Ji (2012) "Theoretical design and experimental verification of a tunable floating vibration isolation system," *Journal of sound and vibration*, **331**(21), pp. 4691–4703.

[86] Kim, S. and R. Singh (2001) "Vibration transmission through an isolator modelled by continuous system theory," *Journal of Sound and Vibration*, **248**(5), pp. 925–953.

[87] Ding, H., M.-H. Zhu, and L.-Q. Chen (2018) "Nonlinear vibration isolation of a viscoelastic beam," *Nonlinear Dynamics*, **92**(2), pp. 325–349.

[88] Ding, H., Z.-Q. Lu, and L.-Q. Chen (2019) "Nonlinear isolation of transverse vibration of pre-pressure beams," *Journal of Sound and Vibration*, **442**, pp. 738–751.

[89] Snowdon, J. C. (1973) "Isolation and absorption of machinery vibration," *Acta Acustica United with Acustica*, **28**(6), pp. 307–317.

[90] Lim, S., K. Kim, U. Cho, N.-C. Park, Y.-P. Park, K.-S. Park, and W.-Y. Soh (2009) "Cantilever dynamic vibration absorber for reducing optical disk drive vibration," *IEEE transactions on magnetics*, **45**(5), pp. 2198–2201.

[91] Rai, G., C. D. Rahn, E. Smith, and C. Marr (2021) "Vibration Isolation in Continuous Beam Networks," in *ASME International Mechanical Engineering Congress and Exposition*, vol. 85628, American Society of Mechanical Engineers, p. V07BT07A062.

[92] Halwes, D. R. (1975), "Nodal beam inertial flexure," US Patent 3,858,831.

[93] Gaffey, T. M. and R. W. Balke (1976) *Isolation of rotor induced vibration with the bell focal pylon-nodal beam system*, *Tech. rep.*, SAE Technical Paper.

[94] Kelley, B. (1972) "Contributions of the Bell Helicopter Company to helicopter development," *The Aeronautical Journal*, **76**(735), pp. 157–165.

[95] Shipman, D. (1973) "Nodalization applied to helicopters," *SAE Transactions*, pp. 2961–2971.

[96] Rai, G., C. Rahn, E. Smith, and C. Marr (2022) "Nodal beam stack vibration isolators," *Mechanical Systems and Signal Processing*, **179**, p. 109324.

[97] Michalczyk, K. and W. Sikora (2021) "Analysis of the nodal beam isolation system based on application of helical spring," *Acta Mechanica*, **232**(10), pp. 3997–4007.

[98] Snowdon, J. (1974) "Forced vibration of internally damped rectangular and square plates with simply supported boundaries," *The Journal of the Acoustical Society of America*, **56**(4), pp. 1177–1184.

[99] Lobontiu, N. (2002) *Compliant mechanisms: design of flexure hinges*, CRC press.

[100] Letcher, T. and M. Waytashek (2014) "Material property testing of 3D-printed specimen in PLA on an entry-level 3D printer," in *ASME International Mechanical Engineering Congress and Exposition*, vol. 46438, American Society of Mechanical Engineers, p. V02AT02A014.

[101] Gent, A. N. (2012) *Engineering with rubber: how to design rubber components*, Carl Hanser Verlag GmbH Co KG.

[102] García Tárrago, M.-J., L. Kari, J. Viñolas, and N. Gil-Negrete (2007) "Torsion stiffness of a rubber bushing: a simple engineering design formula including the amplitude dependence," *The Journal of Strain Analysis for Engineering Design*, **42**(1), pp. 13–21.

[103] Horton, J. and G. Tupholme (2006) "Approximate radial stiffness of rubber bush mountings," *Materials & design*, **27**(3), pp. 226–229.

[104] Adkins, J. and A. Gent (1954) "Load-deflexion relations of rubber bush mountings," *British Journal of Applied Physics*, **5**(10), p. 354.

[105] Parker LORD, *AEROSPACE DEFENSE ISOLATOR CATALOG*, [Online]. URL `https://lordfulfillment.com/pdf/44/PC6116_AerospaceandDefenseIsolator.pdf`

[106] Sayag, M. R. and E. H. Dowell (2016) "Linear versus nonlinear response of a cantilevered beam under harmonic base excitation: theory and experiment," *Journal of Applied Mechanics*, **83**(10).

[107] Amabili, M. (2018) "Nonlinear damping in large-amplitude vibrations: modelling and experiments," *Nonlinear Dynamics*, **93**(1), pp. 5–18.

[108] Balasubramanian, P., G. Ferrari, and M. Amabili (2018) "Identification of the viscoelastic response and nonlinear damping of a rubber plate in nonlinear vibration regime," *Mechanical Systems and Signal Processing*, **111**, pp. 376–398.

[109] Zhao, Y., Y. Chen, and Y. Zhou (2019) "Novel mechanical models of tensile strength and elastic property of FDM AM PLA materials: Experimental and theoretical analyses," *Materials & Design*, **181**, p. 108089.

[110] He, X., M. Qu, X. Shi, et al. (2016) "Damping properties of ethylene-vinyl acetate rubber/polylactic acid blends," *Journal of Materials Science and Chemical Engineering*, **4**(03), p. 15.

[111] Mahapatra, K. and S. Panigrahi (2019) "Dynamic Response of a Damped Euler–Bernoulli Beam Having Elastically Restrained Boundary Supports," *Journal of The Institution of Engineers (India): Series C*, **100**(6), pp. 891–905.

[112] Beniak, J., P. Križan, L. Šooš, and M. Matúš (2019) "Research on shape and dimensional accuracy of FDM produced parts," in *IOP conference series: materials science and engineering*, vol. 501, IOP Publishing, p. 012030.

[113] Eaton Corporation, *Vibration Isolation Section Type Hangers Catalog*, [Online]. URL `https://www.eaton.com/content/dam/eaton/products/support-systems/pipe-hangers/ph-20-catalog-sections/vibration-isolation-section-pipe-hanger-catalog.pdf`

[114] Parker Lord Corporation, *LORD Vibration, Shock and Motion Control Products Catalog*, [Online].

URL https://www.lord.com/sites/default/files/Documents/ProductCatalogs/PC7000_IndustrialParts.pdf

[115] Herzog, D., K. Asami, C. Scholl, C. Ohle, C. Emmelmann, A. Sharma, N. Markovic, and A. Harris (2022) "Design guidelines for laser powder bed fusion in Inconel 718," *Journal of Laser Applications*, **34**(1), p. 012015.

[116] Young, W. C., R. G. Budynas, and R. J. Roark (2002) *[Formulas for stress and strain]; Roark's formulas for stress and strain*, McGraw-Hill.

[117] Ling, C.-B. (1968) "On stress-concentration factor in a notched strip," .

[118] Smith, S. T., V. G. Badami, J. S. Dale, and Y. Xu (1997) "Elliptical flexure hinges," *Review of Scientific Instruments*, **68**(3), pp. 1474–1483.

[119] Hale, L. C. (1999) *Principles and techniques for designing precision machines*, *Tech. rep.*, Lawrence Livermore National Lab.(LLNL), Livermore, CA (United States).

[120] Dirksen, F., M. Anselmann, T. I. Zohdi, and R. Lammering (2013) "Incorporation of flexural hinge fatigue-life cycle criteria into the topological design of compliant small-scale devices," *Precision Engineering*, **37**(3), pp. 531–541.

[121] Issler, L., H. Ruoss, and P. Häfele (2013) *Festigkeitslehre-Grundlagen*, Springer-Verlag.

Vita

George Rai

Education

- **The Pennsylvania State University** (August 2018 - July 2022)
  Doctor of Philosophy in Mechanical Engineering
- **University of Balamand** (August 2015 - May 2018)
  Bachelor of Science in Mechanical Engineering

Publications

- **Rai, G.**, Rahn, C., Smith, E., Marr, C.. 3D Printed Circular Nodal Plate Stacks for Broadband Vibration Isolation. (under preparation).
- **Rai, G.**, Rahn, C., Smith, E., Marr, C.. Dynamic Antiresonant Vibration Isolators with Flexible Levers. (under preparation).
- **Rai, G.**, Rahn, C., Smith, E., Marr, C. (2022). Nodal beam stack vibration isolators. *Mechanical Systems and Signal Processing*, 179, 109324.
- **Rai, G.**, Rahn, C. D., Smith, E., Marr, C. (2021, November). Vibration Isolation in Continuous Beam Networks. In *ASME International Mechanical Engineering Congress and Exposition* (Vol. 85628, p. V07BT07A062). American Society of Mechanical Engineers.
- Saxena, A., **Rai, G.**, Lanari, V., Rahn, C. D., Manogharan, G. (2021, November). Strain-Coupled Fluidlastic Circuits Inside Metal Additive Manufactured Structures. In *ASME International Mechanical Engineering Congress and Exposition* (Vol. 85611, p. V07AT07A041). American Society of Mechanical Engineers.
- **Rai, G.**, Rahn, C. D., Smith, E., Marr, C. (2020, November). Vibration isolation using continuous beams. In *ASME International Mechanical Engineering Congress and Exposition* (Vol. 84553, p. V07BT07A046). American Society of Mechanical Engineers.